NTNU
Norwegian University of
Science and Technology

Device-level control of microgrids with Master-Slave structure

Rakel Alice Utne Holt

Master of Energy and Environmental Engineering
Submission date: February 2018
Supervisor: Kjell Sand, IEL

Norwegian University of Science and Technology
Department of Electric Power Engineering

Abstract

Microgrids are low voltage distribution networks comprising various distributed generators, storage devices and controllable loads that can operate as a controlled entity, either interconnected or isolated from the main distribution grid. Successful operation of microgrids can increase the reliability and efficiency of the energy system, lower operational costs and facilitate the implementation of renewable energy sources. However, long-established regulation strategies used in conventional power systems might not be feasible in microgrids, due to the new system configuration, the variety of resources utilized, and the considerable presence of power electronics.

A control system for a microgrid model has been developed. The model consists of a generating unit (PV-array), a storage unit (battery), a distribution system and loads, as well as the power electronic interfaces between the AC- and the DC-components. The control is performed through inverter control of the microgrid units in a master-slave structure. The control functions implemented are current control, power control, voltage control, and maximum power point tracing of the PV-array. The control system was developed using the rotating dq-frame coordinate system, and implemented in the MATLAB/Simulink simulation tool. Most simulations concerned events that spanned less than 3 seconds, and it took approximately 5-10 seconds to perform the simulations.

The control system was shown to enable optimized efficiency of the PV-array, while at the same time regulate the amplitude and frequency of the load voltage in the presence of a variable load condition and a variable supply. The control system was feasible during both grid-connected and islanded operation, and was able to adapt to islanding events with the microgrid stability preserved.

An advantage of the master-slave structure utilized is that it enabled reference tracking with zero steady-state error. A disadvantage with the strategy is the need for two distinct controllers on the master unit (the battery), with following dependence on proper coordination of battery controller modes. The application potential of the developed simulation model was demonstrated. Simulations concerned transient dynamics during important events, such as the islanding of the microgrid during power exchange with the utility, and islanding that did not coordinate with the microgrid master controller. It was also demonstrated how the current controller time constant affected the battery's voltage reference tracking ability. As the time constant increased, the reference tracking ability became more sensitive to the load conditions.

Sammendrag

Mikronett er segmenter av lavspentnettet, og omfatter distribuerte kilder, lagringsenheter og fleksible laster. Mikronettet kan driftes som en kontrollert enhet, enten sammenkoblet med eller isolert fra resterende nett. Det er forventet at mikronett vil øke energisystemets pålitelighet og effektivitet, samt legge til rette for å ta i bruk fornybare energikilder. Konvensjonelle reguleringsstrategier er imidlertid ikke direkte overførbare til mikronett. Dette skyldes ny systemkonfigurasjon, et spekter av tilkoblede enheter, samt stor bruk av kraftelektronikk.

Det er utviklet et kontrollsystem for en modell av et mikronett. Modellen består av en fornybar kilde (solcelle), en lagringsenhet (batteri), et distribusjonsnett og laster, samt omformere mellom AC- og DC-komponentene. Kontrollen utføres ved styringssignaler til systemets invertere. Enhetene i mikronettet er organisert i en "Master-Slave" struktur. Reguleringsfunksjonene er strøm-, effekt-, spenning- og frekvensregulering, samt sporing av maksimalt effektuttak fra solcellepanelet. Kontrollsystemet ble utviklet ved bruk av det roterende dq-koordinatsystemet, og implementert i simuleringsverktøyet MATLAB / Simulink. De fleste simuleringene viser hendelser som strekker over mindre enn 3 sekunder, og det tok omtrent 5-10 sekunder å kjøre simuleringene.

Det er vist at kontrollsystemet kan optimalisere effektuttaket fra solcellepanelet, og samtidig regulere frekvensen og amplituden på lastspenningen, også under variabelt lastnivå og variabel forsyning. Kontrollsystemet fungerer både nett-tilkoblet og i isolert drift, og bevarer stabiliteten under frakobling fra distribusjonsnettet.

"Master-Slave" strukturens styrke er at mikronettet stabiliserer seg i en drifttilstand lik referenasentilstanden (null avvik). En svakhet med strategien er behovet for to ulike kontrolsystem på hovedenheten (batteriet). Batteriet må da driftes forskjellig i nettilkoblett drift og i isolert drift, og en samkjøringsmekanisme må være til stede. Simuleringsmodellens brukspotensial er demonstrert. Simuleringene omhandlet transiente forløp under kritiske hendelser. Dette var frakobling av mikronettet under energiutveksling med dristibusjonsnettet, samt frakobling som ikke var koordinert med batteriets kontrollsystem. Det ble også vist hvordan tidskonstanten til strømregulatoren påvirket batteriets evne til spenningsregulering. Økt tidskonstant førte til at spenningsregulatoren ble mer påvirket av lasttilstanden.

Preface

This thesis concludes my studies at the Norwegian University of Science and Technology. It is submitted to the Department of Electric Power Engineering in partial fulfillment of the requirements for the degree of Master of Science.

Gratitude goes to my family, for the encouragement, favours and willingness to proofread this work. Warm thoughts go to my friends, for the hard work we did the past years, and the detours we took.

I want to thank researcher Kjersti Berg, postdoc Santiago Sanchez Acevedo and prof. Kjetil Uhlen for keeping your doors open for me during this work, enabling valuable discussions and practical advice.

My sincerest thanks go to my supervisor, prof. Kjell Sand. Thank you for guiding me into the field of Smartgrid. A field that without your guidance (as with most mega-trends) I would have been sure to avoid. Both motivation and insights were found when needed. Thank you.

Trondheim, 2018

Rakel Alice Utne Holt

Contents

List of Figures

List of Tables

List of Abbreviations

AC	Alternate current
CCS	Carbon capture and storage
CHP	Combined heat-and-power
DC	Direct current
DER	Distributed energy resources
DG	Distributed generation
DSO	Distribution system operator
DSR	Demand-side response
IEA	International Energy Agency
MPP	Maximum power point
MPPT	Maximum power point tracing
P/Q	Real- and reactive power control
PCC	Point of common coupling
PLL	Phase-locked loop
PV	Photo voltaic
V/f	Voltage and frequency control
VSC	Voltage-source converters

Chapter 1

Microgrid's role in future power systems

1.1 Energy challenge

There are several drivers towards the implementation of microgrids; satisfying the increasing need for power quality and reliability, providing universal access to low cost energy, as well as the pursue towards a low-carbon society. In the World Energy Outlook 2017, IEA introduces for the first time the Sustainable Energy Scenario. The scenario differ from previous scenarios solely driven by climate considerations (*i.e.* the 450 scenario), by also aiming at improved air quality and universal access to modern energy services. The scenario illustrate a path to affordable, secure and sustainable energy that is available to all, and microgrids are included in the realization of this goal.

The Sustainable Development Scenario is designed to limit the average global temperature increase to $2°C$ above pre-industrial levels. This require substantial CO_2 emissions reductions compared with the baseline, the New Policies Scenario. As Figure 1.1 illustrates, energy efficiency and integration of renewable energy sources are expected to account for 80 % of the CO_2 emission reductions by year 2040. Microgrid technology is expected to contribute to both, by aiding the realization of intelligent and flexible electricity network infrastructures, and by facilitate the integration of distributed and renewable energy resources [1]. Regarding energy availability, more than 1.2 billion people were without access to electricity in 2016. In IEA's Universal Access Scenario, 60 % of the capacity additions to deliver electricity access are mini- and off-grid systems, such as microgrids [2].

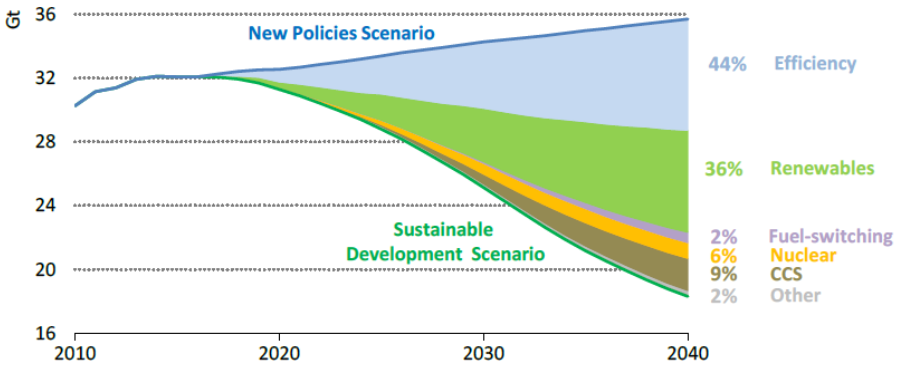

Figure 1.1: *Global CO_2 emissions reductions in the New Policies and the Sustainable Development Scenarios* [3].

Microgrid (and Smartgrid) technology is experiencing great attention in present time. Mission Innovation recognizes microgrid technology to be the most important innovation focus area today [4]. As a member of Mission Innovation, Norway has committed to double its clean energy research and development investments by year 2020. Although this thesis do not touch upon the economic feasibility of microgrids, one point in this regard will be noted: Pursuing net-zero emissions, fossil-fuel power plants in the future must be equipped with carbon capture and storage (CCS) systems. The costs of this is likely to lead to a doubling in fossil-based energy prices [5]. Thus, this should be the financial reference frame when considering the implementation of renewables and efficiency improving measures.

1.2 Conventional power systems

Conventionally, electric power production takes place in large plants. The conversion of mechanical to electrical energy is almost exclusively achieved by means of synchronous generators. The power is transmitted to the loads through a high-voltage network. The voltage level is high during transmission in order to minimize losses, and is step-wise transformed down before reaching the end-user in the distribution part of the network. Typically 8-10 % of the electrical energy is lost during the transmission and distribution stage [6]. Since the electrical energy cannot easily be stored in large quantities, the energy demand must at all times be met by a corresponding generation [6]. Fortunately, the combined load pattern of a large power system normally changes in a relatively predictable manner, and the daily production schedule can be set in advance based on historical data. The actual power demand will fluctuate somewhat around the predicted value, but mismatches are accounted for when they arise by making small adjustments in generation continuously [7].

1.3 Distributed generation

The advantage of the central productions economy of scale is decreasing [8]. Instead, there is a growing potential for small-scale production integrated into the distribution network, referred to as distributed generation (DG). These units are typically photo voltaics (PV), combined heat-and-power (CHP) micro-turbines, wind turbines and possibly fuel cells [9]. Distributed generation alters the traditional operating principle of the grid. First of all, the synchronous generators now operates in parallel with a variety of energy sources, some of which are coupled through power electronic interfaces. A new group of customers, so-called *prosumers* (customers who both produce and consume energy), introduce reverse energy flows by at times generating a surplus which is distributed back to the grid. These time dependent bidirectional power flows disrupt the feasibility of conventional protection coordination and selectivity schemes [10]. Further more, both wind and solar are periodic, non-controllable, and volatile sources. This implies that not only the demand, but also production will be subject to uncertainties, making power balance challenging to maintain. In parallel, an increasing amount of high-power loads are made available, like high-efficient water heaters and fast charging stations for electrical vehicles. This leads to an increase in electrical hours, in peak demand, and in demand variations. In sum, this calls for exploring better ways of operating the power grid.

1.4 Future power systems

In the context of distributed generation, microgrids emerge as a promising control concept [11]. The concept is based on gathering groups of distributed resources, and operate them as individual cells (microgrids) within the larger utility. The microgrids include a portfolio of products and grid improvements intended to enable efficient, responsive, clean and resilient systems [12].

The most salient of the microgrid features is the islanding capability. Islanding refers to the capability to segregate from the rest of the utility, and serve local loads in an autonomous state when desired, see Figure 1.2. This protects the microgrid from utility grid disturbances, and vice versa, protects the utility in the case of upstream disturbances originating in the microgrid. A control system must be applied to each microgrid. The system has the task of coordinating

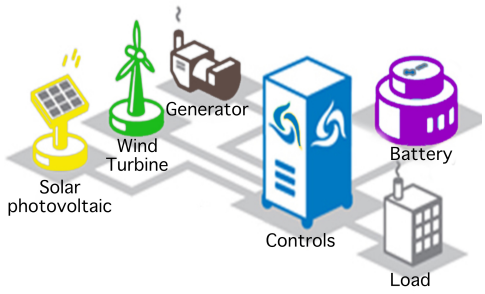

Figure 1.2: *Autonomous operation of distributed resources.* [13].

the units, and regulating the flow
of electricity within the boundaries of the microgrid. However, due to the new system configuration, variety of resources utilized, and the considerable presence of power electronics, long-established regulation strategies used in conventional power systems might not be feasible. New strategies must be investigated in order to harvest the potential benefits of microgrids. The system must be applicable during both grid-connected and islanded operation, and must facilitate the switch between the different modes of operation. The control system must handle periods of transients during disconnection and re-connection with the utility. In the islanded state, the control system should optimize the efficiency of the distributed resources, and satisfy the local demand-supply balance.

1.5 Problem definition and scope of work

The work of this thesis concerns the device level control of microgrids. The microgrid control system includes a range of functions, who operate at different control levels and in different time frames. As seen from Figure 1.3, the device level constitutes the lowermost layer in the control, and operate on the time scale of milliseconds. A goal of this work was to design a device level control layer who optimizes the efficiency of a renewable generating source, a PV-array, while providing the loads with requested amount of power. The control system should be feasible during both grid-connected and isolated operation, and should autonomously adapt to the current mode of operation. A goal was also to study the microgrid behaviour during both common and important scenarios, and this was done through simulations. Through simulations, the reference tracking ability of the controllers where tested in the presence of disturbances. Disturbances consisted of rapid changes in load and supply conditions, disconnection from the utility, and delays or failure in key control signals.

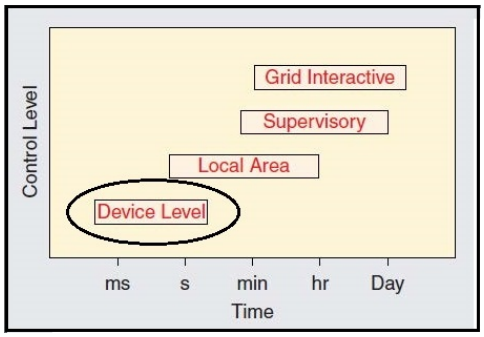

Figure 1.3: *Microgrid control function timescales* [14].

The first part of this work has been a study of what sort of a system a microgrid is, and to what are its most prominent elements and features. In the second part, a

microgrid including loads, a storage battery and a PV-array has been modelled and implemented in the MATLAB/Simulink simulation tool. The control system was developed utilizing known strategies from the control of voltage-source converters (VSC), adopted in a master-slave structure with the storage battery as the master and the PV-array as the slave. The control functions included were current control, real/reactive power control, voltage control and frequency control. The functions were embedded in local controllers on, respectively, the storage battery and the PV-array. In combination, the functions enable flexible energy storage control, as well as maximum power point tracing of the PV-array. The proposed microgrid model has been designed to be compatible with a possible testing in the Smart Grid laboratory at NTNU. The microgrid elements were chosen as to make the model relevant to several on-going projects, *e.g.* Power House Brattøra, Trondheim, and IntegER (SINTEF Energy Research), Trondheim.

1.6 Objectives

The objectives of this thesis are to:

1. Develop an initial framework for the study of microgrid control, particularly applicable to microgrid who incorporate solar power generation, storage battery capacity, and island capability.
2. Explore the feasibility of inverter control in a master-slave structure.
3. Demonstrate the application potential of a simulation model through illustrative case studies - both normal operating cases and cases of failure in key control signals.
4. Provide a treatment of the underlying control concepts.
5. Provide a review of microgrid as a energy system.
6. Provide a microgrid model compatible with a possible testing in the Smart Grid laboratory at NTNU, and relevant to several on-going projects.

Chapter 2

Review of microgrid as a power system

Remark: This work builds on the literature review carried out as part of specialization project TET4520, and as such there is extensive reproduction/usage of the content therefrom.

This chapter is a documentation of a literature review concerning what sort of a system microgrid is, and to what are its most prominent features. Main elements, benefits and challenges are addressed. The two main strategies used for microgrid control are described, whereas one of them is the master-slave structure utilized to control the microgrid model of this thesis. The chapter concludes with a status on microgrid research in Norway.

2.1 Definition of microgrid

The first question that needs to be addressed is simply, what is a microgrid? The answer to this question is not straight forward. In fact, no unified global definition of microgrid exist today. One might wonder why there are regional variances, when the benefits from having a clear definition seems obvious. One reason may be that the microgrid is not an object (although the name suggest that it is), but a concept. It is the concept of operating the electrical network in distributed cells that receive periodic management signals from a central operator. This is beneficial, and even necessary, due to the growing complexity of the electrical grid. As stated in the introduction, an increasing amount of different resources can be connected to the grid. Production is increasingly stochastic, and there is an increasing amount of possible combinations of ways to allocate the resources of the grid. With this, the problem of finding the optimal allocation of resources becomes larger, and perhaps unmanageable. An analogy to this might be the problem of a highly complicated

calculation. What does one do when encountering a calculation that is too large to solve in one piece? If possible, one divide the problem into parts, solve each part separately, and combine the solution. Microgrid can be seen as the manifestation of the same strategy applied to the problem of optimizing the electrical system. By splitting the system into smaller cells (microgrids), one can find the optimal allocation of resources within each cell, and hope that the aggregated set of local solutions will provide a solution fairly close to the global optimum. Now, this might not be a fully adequate description of the microgrid, however, at the very least, it may be a helpful illustration to keep in mind when moving forward.

The United States Department of Energy (DOE) operate with a microgrid definition suitable for the purpose of this work. According to their definition, a microgrid is:

> *a group of interconnected loads and distributed energy resources within clearly defined electrical boundaries that acts as a single controllable entity with respect to the grid. A microgrid can connect and disconnect from the grid to enable it to operate in both grid-connected or island-mode* [15].

Other definitions differ from this, *e.g.* by not requiring the microgrid to be able to operate in an islanded mode. However, the island capability is at the core of this work. To be considered a relevant microgrid within the scope of this thesis, the system should have the following three features:

1. It should be connected to the utility in a single point.
2. It should have the ability to operate in both grid-connected and island-mode.
3. It should include a high share of variable energy resources, and seek to optimize the generation from these sources by combining the generation with a storage device.

A microgrid can be designed to support AC or DC power, or it can be a hybrid solution of the two. Reference [16] highlights the advantages and drawbacks of each technology. The most salient feature of the microgrid is the island capability. This refers to the capability of the microgrid to, segregate from the rest of the utility and serve local loads in an autonomous state. Islanding happens by opening a main switch at the single point that connects the microgrid with the utility. This point is refereed to as the point of common coupling (PCC). The location of the PCC can be seen in Figure 2.1, where a typical microgrid structure is depicted. During islanded operation, the microgrid must independently provide energy to its local loads. Thus, the installed capacity of the microgrid must exceed the peak critical load. The islanded microgrid can be re-synchronized with the utility once the disturbance is removed. When the microgrid is in grid-connected operation, it can exchange energy with the utility. From the utility's point of view (as the microgrid is connected in a single point), the microgrid is seen as a single load or as a single source supporting the grid.

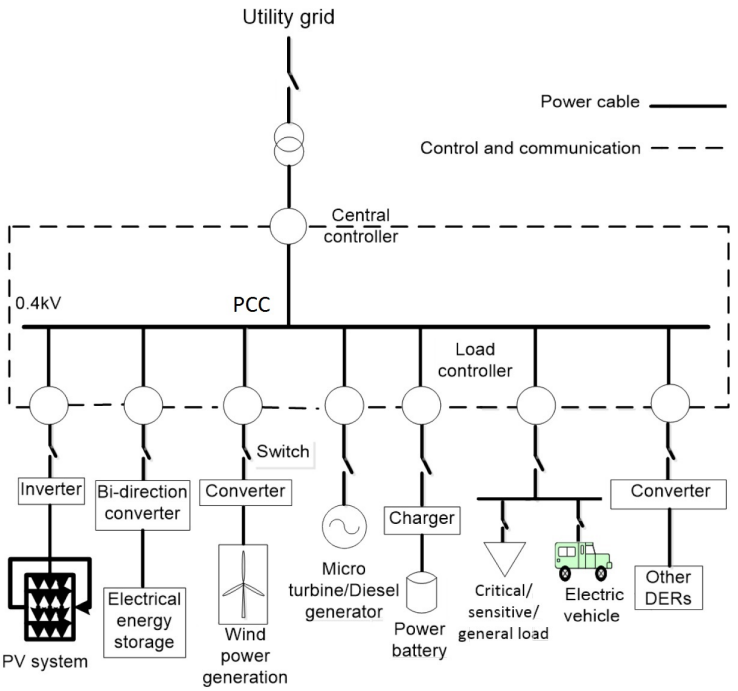

Figure 2.1: *Typical microgrid structure* [15].

2.2 Microgrid elements

This section will describe the elements that usually exist in a microgrid. The main elements can be seen in Figure 2.1. Main elements that will be addressed are distributed generation, energy storage, loads, and power electronics. As solar power and VSCs are of particular relevance to the scope of this thesis, they are granted some additional focus.

2.2.1 Distributed generation

The energy sources within a microgrid are distributed, meaning they are essentially small units integrated in the distribution network. Main generating units are wind turbines, PVs, CHP-microturbines and possibly fuel cells [9]. It is important to separate between controllable and non-controllable resources, also referred to as dispatchable and variable. Variable resources are of a fluctuating nature, and cannot always be called upon when desired. For example, the production from PV units are limited by the amount of solar irradiation, and power from wind turbines are limited by the wind condition. The production from these sources can to some degree be predicted, but is by no means certain. As the variable resources

cannot be controlled to a specific output, these units are typically operated at their maximum power point (MPP). This is the point that optimizes the efficiency of the unit. Dispatchable resources are those that can be controlled to a specific output, as *e.g.* microturbines and fuel cells. The dispatchable resources can be called upon to help meet either fluctuating demand or to complement variable forms of supply. Their power output is therefore set and updated according to the given load condition. In general, renewable energy sources are usually of a variable nature (with hydro power as an exception), and fossil-based energy sources are usually dispatchable.

Solar PV features

A benefit of solar power is that it is a global resource, which can be harvested anywhere. However, the solar power is variable in its nature. The PV-arrays do not include any rotating components, thus, they do not contribute to system inertia and associates with fast dynamics. Fast dynamics in combination with a fluctuating irradiance may be challenging from a control perspective, and are to be considered downsides of these units. Figure 2.2 depicts solar irradiance on a horizontal surface for a mostly clear day and a mostly cloudy day in Greenbelt, Maryland. As seen from the figure, solar power production may vary rapidly due to the sudden shading from clouds.

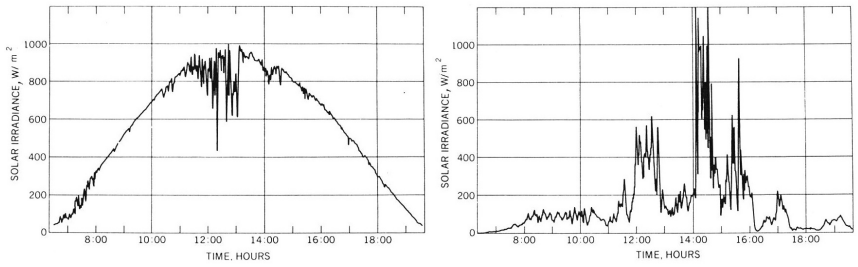

Figure 2.2: *Solar irradiance on a horizontal surface for a mostly clear (left) day and a mostly cloudy (right) day in Greenbelt, Maryland [17].*

Global solar PV capacity

In spite of the associated control challenges, there has been a massive increase in PV capacity additions in resent years. In 2015, capacity additions made in solar PV was record high, with 49 GW installed additions, accounting for approximately one sixth of the world's total additions [18]. The major expansion of the market are underpinned by rapid cost reductions, both in the utility- and decentralised-scale markets. As can be seen in Figure 2.3, PV installations are seeing cost declines of 40-75 % in leading markets since 2010. Solar PV are also expected

to be distributed to a significant degree. In both the 450 Scenario and the New Policies Scenario, more than 40 % of the installed PV capacity will be distributed within 2040. In the Universal Access Scenario, solar PV in year 2040 is the largest source of mini- and off-grid electricity generation, accounting for more than a third of total generation.

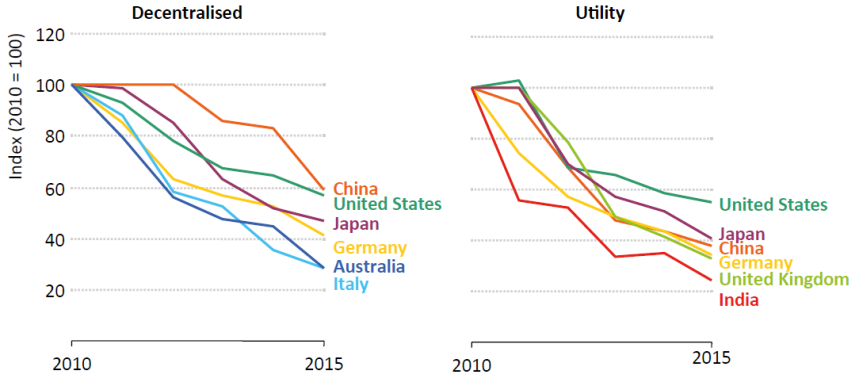

Figure 2.3: *Index of solar PV unit investment cost in selected markets. Investment cost can be seen to have fallen rapidly around the world* [18].

2.2.2 Loads

Microgrid loads are commonly categorized as fixed or flexible (also known as adjustable or responsive) [12]. Fixed loads cannot be altered and must be satisfied under normal operating conditions. In contrast, flexible loads are responsive to control signals, and can be shifted. Historically, systematic control of electricity demand at short notice has not been viable. Therefore, electricity supply has so far needed to be instantaneously adjusted to match demand. The rise of modern information and communication technologies is making it possible to monitor and control demand rapidly and at large scale. Thus, the demand can to some extent be shaped to match supply, making the demand so-called flexible. The re-shaping of the load curve is referred to as demand-side response (DSR), and is primarily performed by either load shifting (transfer demand in time without affecting the total electricity demand) or load shedding (lowering the total energy demand by interrupting loads). DSR may be performed by top-down or bottom-up management [19]. Top-down management is performed by the system operator, while bottom-up refers to consumer driven action, stimulated by the appropriate information, *e.g.* price signals. With DSR, the customer is considered a potential resource, who provide flexibility to the grid operator in return of an economic value. Their services can be regarded as similar to that of a storage unit. Thus, successful DSR schemes may relieve the need for investing in high-cost storage capacity. It is also common to distinguish between high- and low-priority loads. During abnormal situations, it

might be necessary to shed non-flexible loads. In this case, loads are shed according to their priorities in order to secure and improve reliability of the most critical loads. High-priority loads are *e.g.* hospitals or certain kinds of industry.

2.2.3 Energy storage systems

Although storage systems are no source of energy, they are included in the term distributed energy resources (DER). A storage unit can be used to absorb temporarily mismatches between power generation and demand. These devices are vital to stabilize the energy production from the variable renewable energy sources. Energy storage systems can be in the form of traditional batteries, super capacitors and flywheels, but also in the form of coordinated charging and discharging of electrical vehicles, and thermal storage in building stock. In low inertia systems, the energy buffer stored in rotating masses is low, putting higher requirements to the storage system short response time. Batteries are examples of storage systems with a rapid response, and the growth of the global grid-scale battery fleet is largely driven by lithium-ion batteries. Lithium-ion batteries are also the most popular type of rechargeable batteries for portable electronics and electric vehicles [1]. Storage systems serve two major functions in a microgrid.

1. They provide loads with energy when there is a deficit in production from the variable resources.
2. They prevent energy curtailment when there is a surplus in production from the variable resources.

Energy curtailment is energy that is not utilized. In systems with high penetration of variable generation, curtailment may represent a substantial energy loss, see Figure 2.4. Usually, peak production from variable sources do not coincide with peak demand. Grid regularities dictate how much energy is allowed to be delivered from prosumers (end user with both consumption and production behind their own connection point). In Norway, grid regulations prohibit prosumers from power delivery exceeding 100 kW [20]. An ongoing project in Trondheim involves installing rooftop PV on two commercial buildings at Brattørekaia. Combined, they have a peak production of 600 kW. At the same time, the power

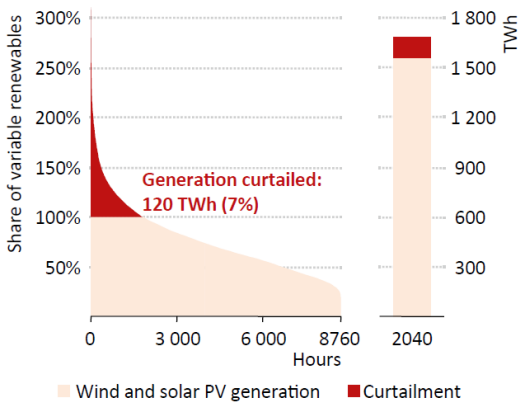

Figure 2.4: *Curtailment without storage and DSR measures in the European Union in the 450 Scenario, 2040 [1].*

demand in weekends is expected to be zero. Without some form of energy storage system, the energy loss is projected to be 350.000 kWh yearly, equivalent to 55% of production. On a European scale, by 2040, more than 570 GW of wind and solar PV installations is projected to come online in the European Union (the 450 scenario) [21]. In the absence of storage and DSR, total curtailment is expected to exceed 85 TWh, equivalent to 6.9 % of generation [18]. Storage system limitations are often cost-related, but lack of appropriate management and control strategies might also be an issue [22]. This is a field under constant investigation and development.

2.2.4 Power electronics

Microgrids have a considerable presence of power electronics. The diverse use of energy sources makes power electronic converters a necessity, the function of which is to facilitate the exchange of energy between subsystems that cannot be directly interfaced with each other. Solar power and storage batteries, for example, are DC units, and cannot be connected with an AC microgrid busbar except through an converter. Also, the connection of wind turbines must be interfaced by means of a back-to-back AC/DC and DC/AC converter, if one wishes to operate the turbine at variable speed. Other important power electronic components are smart switches. Smart switches are circuit breakers which can sense and determine abnormal operation situations, and take actions to prevent faults. They can send signals about their status to the central controller, and can also receive remote commands and open or close the circuit based on the received command.

The voltage-source converter

One of the most commonly used power-electronic converters for high-power applications is the voltage source converter (VSC). Figure 3.2 illustrate the VSCs role as the interface between a DC and an AC system. The DC system that maintains the net voltage of the capacitor can be *e.g.* a battery unit, or it can be a DC power source such as a PV-array. The fundamental component of the AC-side voltage is usually controlled based on a pulse-width modulation technique [23].

The energy exchange between the DC- and the AC-system is facilitated by means of coordinated on/off-states of six semiconductor switches. In contrast to mechanical switches, on/off transition in electronic switches are achieved without any moving parts (*e.g.* the movement of a mechanical arm), making them suitable for fast repetitive switching. However, they introduce switching and conduction power losses not found in their mechanical counterpart, and effort to minimize these losses is the subject of major research and development programs of the power semiconductor switch industry [23].

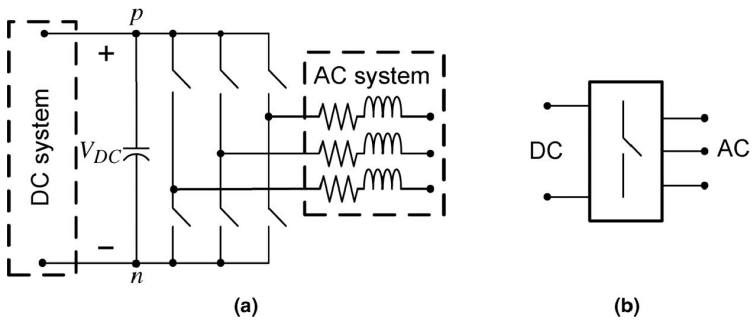

Figure 2.5: *(a) Schematic diagram of a three-wire, three phase, two-level VSC. (b) The symbolic representation of the three-phase VSC.*

2.2.5 Key features

The microgrid separates itself from the conventional power system by a portfolio of products and grid improvements intended to enable a more efficient, responsive, clean and resilient system. Key differences between the conventional power grid and a microgrid is summarized in Table 2.1 [24]. The microgrid is said to manage "in-

Table 2.1: *Comparison between the conventional grid and a microgrid.*

Conventional grid	Smartgrid/Microgrid
One-way communication	Two-way communication
Few sensors	Sensors throughout
Electromechanical	Digital (and electromechanical)
Manual monitoring	Self-monitoring
Manual restoration	Self-healing
Failures and blackouts	Adaptive and islanding
Limited control	Extensive control
Few customer choices	Many customer choices

telligently" its own consumption and production. Here, intelligent is a simple word referring to the combined effects from table 2.1, *e.g.* self-monitoring, self-healing, adaptive learning and control. To realize this, the microgrid depend on advanced information and communication infrastructure, far more so than the traditional power system [24]. An example of a product enabling a two-way communication between a utility company and its customers in a microgrid is the smart meter. The smart meter register electricity consumption every hour, and automatically send information to the distribution system operator (DSO). The DSO get a more correct basis for billing customers, and the customer receive time-of-use information about consumption and prices [25]. This give consumers better opportunities

to engage in demand response, *e.g.* by voluntarily reducing their electricity demand during peak hours. This puts less pressure on the grid, relieving the utility of having to invest in additional power substations or line reinforcements.

2.3 Benefits with microgrid

Microgrids was introduced in the technical literature as a solution to many of the concerns around successful integration of distributed energy resources, listed in reference [22]. Main advantages are summarized below, where several are those associated with distributed resources in general. Microgrids [11][26][27][28]:

1. Facilitate high penetration of renewable energy sources, being in compliance with the future low-carbon society.
2. Alleviate the pressure from the main transmission system, as well as reducing transmission losses by exploiting local sources of energy.
3. Lower generation, transmission and distribution costs.
4. Continue to serve critical loads even if the main utility grid is down due to fault, increasing the overall reliability of the system.
5. Optimize flexible loads to fit production, increasing the system efficiency and postponing the need for grid reinforcements.
6. Bring electricity to remote sites and rural areas without extensive expansion of the utility grid.
7. Can easily increase or decrease its capacity by adding or removing modules.

Cost savings by eliminating expensive transmission lines or sea-cables are especially important drivers for isolated microgrids, who may be situated a long distance from the main utility.

2.4 Challenges with microgrid

Some issues are still to be addressed in order to harness the potential benefits of microgrids without jeopardizing the present level of reliability. Main technical challenges found in [22][26][29] are those of:

1. Voltage and frequency output control. The output of inverter-based energy units are internally set, and does not inherently vary with reactive and active power.
2. Low inertia. Can lead to critical frequency deviations if proper control mechanisms are not implemented.

3. Stability issues, particularly during transition from connected to stand-alone mode.

4. Protection issues, mainly concerning bi-directional power flows and low contributions to fault currents.

5. Power quality, affected by harmonics produced by power electronics, volatile power production and asymmetry of nonlinear loads.

6. Dividing the production among generating units in an optimal way under supply and demand uncertainty. Determination of appropriate levels of reserves.

In addition to the technical barriers, microgrid encounter non-technical barriers as regulatory policies and ownership models, elaborated in Reference [30].

2.5 Two important control strategies

As illustrated in Figure 2.6, the control system has the task of coordinating all units within the microgrid. There are two main control strategies commonly used for microgrids. These are the master-slave strategy and the peer-to-peer strategy. A combination of the two can also be adopted. Peer-to-peer is most commonly used in large microgrids, while master-slave is the most commonly used strategy for small microgrids [31]. Table 2.2 present a comparison of the two, highlighting advantages and disadvantages with both strategies.

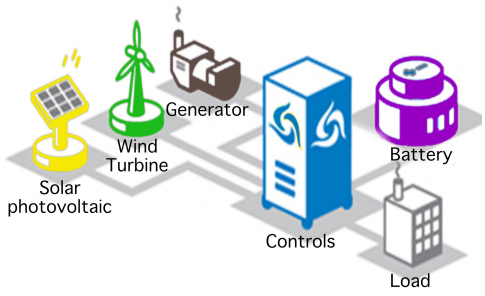

Figure 2.6: *Central control system to coordinate units within the microgrid* [13].

During grid-connected operation, none of the microgrid units participate in the regulation of voltage or frequency. This is because the voltage and frequency during this time is supported and regulated by the utility grid. Instead, the microgrid units simply inject or (in case of a storage unit) absorb power. This is referred to as the units being under power control (P/Q control). In island operation, however, the microgrid must by itself ensure that the voltage at the PCC is of nominal magnitude and frequency. Thus, the microgrid units must also engage in voltage-frequency control (V/f control). The peer-to-peer strategy and the master-slave strategy solves this in two distinct ways.

Table 2.2: *Comparison between master-slave and peer-to-peer strategies.*

	Master-slave	Peer-to-peer
Local control	P/Q and V/f	Droop control
Steady state error in voltage and frequency	Zero	Constant
Advantages	Zero steady state error	Equal in both grid-connected and island mode Simple control design Less communication
Challenges	Single point of failure	Sacrifice stability May need adjustments to take into account highly resistive lines
Typical application	Small microgrids	Larger microgrids

2.5.1 Master-Slave strategy

With the master-slave strategy, one or more microgrid resources acts as the 'master', while the other resources act as 'slaves'. As the name might suggest, the master and the slave units are assigned with different responsibilities in the microgrid. The master alone has the responsibility to ensure that the PCC voltage has nominal magnitude and frequency in the islanded state. Thus, immediately after the microgrid is separated from the utility, the master must be switched from P/Q control to V/f control. The slave units, on their part, remain under P/Q control also after islanding. The voltage at the PCC will be of nominal magnitude if the power demand from loads are met by a corresponding supply. Thus, as the master is in charge of the voltage regulation means that the master must adapt to changes in loads (or variable production from the slave units). The master should therefore have an output that is controllable. A benefit with the master-slave structure is that it has zero steady state error in voltage and frequency. A downside is that the master unit must be controlled with different strategies in the grid-connected and island modes. This complicates the control design, and further require the implementation of fast island detection schemes. These schemes are incorporated to detect possible unintentional islanding of the microgrid, and make the proper switch from P/Q to V/f control. These schemes work on the time frame of milliseconds [32].

2.5.2 Peer-to-Peer strategy

With this control strategy, all microgrid units are equal, and there is no master or slave. Instead, droop control is adopted. The method of droop control is a familiar one, being the conventional way to control synchronous generators in the main interconnected grid. The droop principle implies that all units participate in the regulation of nominal voltage magnitude and frequency. When the load changes,

the changes will be automatically distributed among the generating units according to the droop factor. Thus, all units will adjust the frequency and amplitude of their output voltage to establish a new steady-state with reasonable distribution of output power. An important benefit of the droop control is that it remain unchanged for grid-connected and island operation, facilitating smooth transfer between the two modes. The control design is simple, and little communication is needed. However, with the droop technique, the system is designed to allow the steady-state frequency and voltage to drop as the load increases. Thus, the simple, easy-to-deploy structure comes at the sacrifice of voltage and frequency stability [31].

2.6 Status on microgrid research in Norway

Norway is well positioned for a future smarter energy system. Broadband communication to homes is well-developed, and large portions of electricity in the domestic sector is used for space and water heating. This offers much flexibility for DSM. Two important drivers for smart grid priorities are large scale adoption of electrical vehicles, and an aging infrastructure. The EV fleet in Norway is rapidly growing, now containing around 150 000 vehicles and 1 500 fast charging stations. At the same time, approximately 40 % of supply terminals in Norway are weaker than the standardized electromagnetic compatibility reference impedance. Weak parts of the grid might experience voltage quality problems, and the issue may be worsened by the deployment of EVs and other high-power applications [4].

Figure 2.7: *Electric power system in Norway* [4].

Adapting to a flexible and intelligent distribution system might solve increased energy- and power related issues at a more acceptable cost than pure reinforcement of the grid. As a step towards the more intelligent electrical distribution system, regulators in Norway required the implementation of smart meters in every household by January 2019. In 2010, a national Smart Grid demonstration and laboratory platform, *Demo Norway*, was established. The main purpose of Demo Norway is to support development, testing and verification Smart Grid technologies, services and use cases, both in real life and laboratory environment. Currently, Demo Norway comprises eight power system demo sites, of which one is exploring island operation of microgrid. Distributed energy storage and solar PV are in focus at several of the other sites [4].

In 2016, the Norwegian National Smart Grid Laboratory at NTNU and SINTEF Energy research was formally opened. A specific feature of the laboratory is the opportunity to combine real-time simulations with physical power system assets (power hardware in-the-loop), through a 200 kVA power supply interface. The set-up can be both 400 V AC or 700 V DC. The set-up is flexible, allowing a range of use cases to be tested, ranging from smart homes and microgrids to multiterminal AC- or DC transmission systems. Also in 2016, a research centre for intelligent electricity distribution, FME CINELDI, was appointed (SINTEF). The purpose of CINELDI is to enable a cost-efficient realization of a flexible and robust future Norwegian electricity distribution grid. Microgrid is is here included as one out of 5 main topics of research. FME CINELDI has a budget of about NOK 360 million and will last for 8 years [4].

Chapter 3

Simulation model and method

This chapter provides a description of the microgrid developed. This involves separate treatment of components, with the mathematical equations and the description of key properties. It also involves the combination of components, *e.g.* the combination of the PV-array, the VSC and an impedance into the complete PV-array feeder line. The chapter also describe the method for implementation of the control system, highlighting the merits and drawbacks with the method of choice.

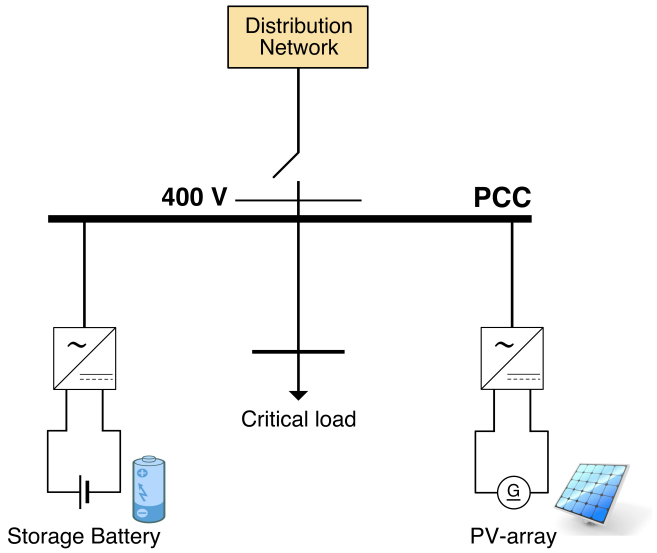

Figure 3.1: *The structure of the microgrid developed and analyzed.*

3.1 Models for the power system components

The microgrid schematics is shown in Figure 3.1. The main components are two VSC, a PV-array, a storage battery and a critical load. The components are connected to a a 400 V AC distribution network through a switch. The microgrid control system is addressed in Chapter 4 and 5. The control system coordinate the production from the PV-array and the charging/discharging of the battery. This is done through processing control and measurement signals which culminate in proper gating/switching signals sent to the VSC.

3.1.1 Voltage-source converter model

The function of the VSC is to facilitate the exchange of energy between subsystems that cannot be directly interfaced with each other. The VSC is modelled as an ideal converter in series with a small resistor r_{on}, representing the on-state resistance of the converter switches. Figure 3.2 depicts a schematic diagram of this VSC model.

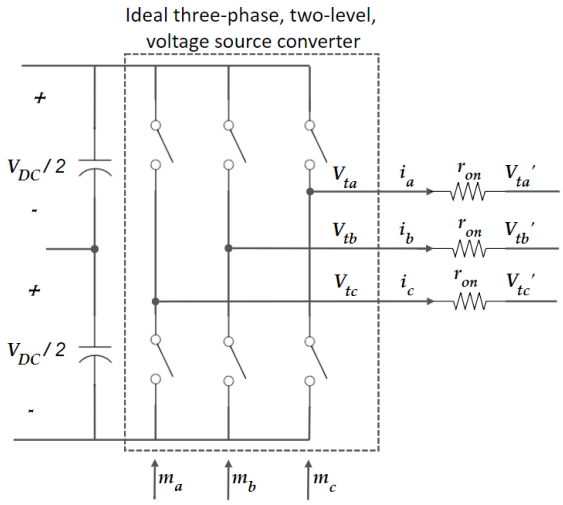

Figure 3.2: *Schematic diagram of a three-phase, two-level voltage sourced converter.*

In the figure, V_{DC} is the net voltage over the DC-side capacitors (maintained by the storage battery or the PV-array). $V_{t,abc}$ is the AC-side voltage of the idealized converter, and $V'_{t,abc}$ is the AC-side voltage after the switches. i_{abc} is the three-phase line current, and m_{abc} is the gating/switching signal to the converter. The voltage profile of $V'_{t,abc}$ is averaged over one switching cycle. Thus, $V'_{t,abc}$ is given

by

$$V'_{ta} = V_{ta} - r_{on}i_a = m_a(t)\frac{V_{DC}}{2} - r_{on}i_a, \tag{3.1a}$$

$$V'_{tb} = V_{tb} - r_{on}i_b = m_b(t)\frac{V_{DC}}{2} - r_{on}i_b, \tag{3.1b}$$

$$V'_{tc} = V_{tc} - r_{on}i_c = m_c(t)\frac{V_{DC}}{2} - r_{on}i_c. \tag{3.1c}$$

It can be seen that m_{abc} is the scaling factor which decide the ratio of V_{DC} and the ideal voltage $V_{t,abc}$. This averaged model looses information about switching harmonics, but benefit from fast simulation. This model will be utilized due to the high value of a fast running simulation in this initial work on microgrid control.

3.1.2 PV-array model

The PV-array is modeled as multiple modules connected in series and parallel branches. Each module is modelled by an equivalent circuit referred to as the single diode model, illustrated in Figure 3.3. This is a five parameter model, using a current source, I_L, a diode, a series resistance, R_s, and a shunt resistance, R_{sh}, to represent the irradiance- and temperature dependent I-V characteristic of the modules. The diode I-V characteristics for a single module is defined by Equation 3.2

$$I_D = I_0\big[exp\big(V_D/V_T\big) - 1\big], \tag{3.2a}$$

$$V_T = \frac{kT}{q} * nl * Ncell, \tag{3.2b}$$

where the equation parameters are given by Table 3.1. The power generation of the PV-array originates from I_L, which is a light-generated current. I_{DC} is the share of this current that passes through the external circuit, and I_D, and I_{sh} are shares that do not pass through the external circuit. V_{DC} is the imposed voltage at the array terminals. This voltage depend on the magnitude of I_{DC}, and

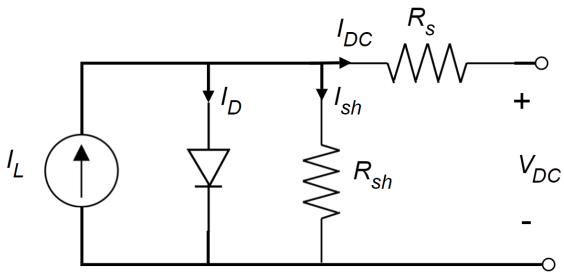

Figure 3.3: *The single diode model [33].*

notably, on the magnitude of the external circuit impedance. If the impedance of the external circuit rises, V_{DC} rises, and *so do the power delivered to the external circuit*. This is due to the PV-array behaving like a current source (not a voltage source). Figure 3.4 show the power-voltage characteristic of the utilized PV-array (parameters listed in Appendix C). It can be seen that the power delivery from the array increases as V_{DC} increases. However, due to the diode, there will be an upper limit to V_{DC} (when the diode is fully conducting). The power delivery from the array drops drastically when V_{DC} approaches its upper limit, as more and more current is flowing through the diode. The black line in the figure is a trajectory of the terminal voltage, V_{mp}, that optimizes the efficiency of the PV-array. The operating condition that leads to the highest possible power extraction is therefore when $V_{DC} = V_{mp}$. It can be seen that V_{mp} is a function of the solar irradiance. Thus, to operate the array optimally, one must make V_{DC} track V_{mp} (which vary as the solar irradiation varies). This is referred to as *maximum power-point tracing* (MPPT). MPPT is an extension to power control. Thus, MPPT can only be achieved if the array is under P/Q control (not V/f control). MPPT will be described and implemented in Chapter 4.

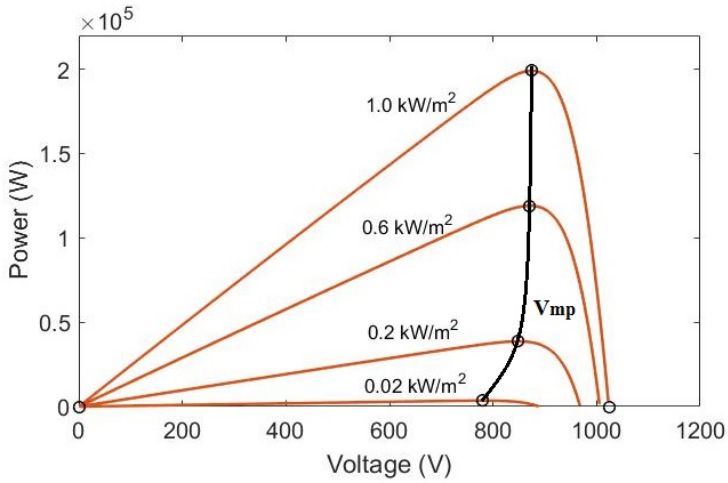

Figure 3.4: *Power-voltage characteristic of the utilized PV-array model.*

Connecting the PV-array to the PCC

The PV-array is connected to the PCC by a three-phase feeder line, and interfaced by a VSC and a large capacitor, C. The schematic diagram is shown in Figure 3.5. The large capacitor is added to stabilize V_{DC}, so it can be more easily regulated. The averaged, ideal VSC is connected to the right hand-side of the capacitor. The

Table 3.1: *Parameters of Equation 3.2.*

I_D	diode current [A]
V_D	diode voltage [V]
I_0	diode saturation current [A]
nl	diode ideality factor ≈ 1.0
k	Boltzmann constant = 1.3806 e^{-23} [J/K]
q	electron charge = 1.6022 e^{-19} [C]
T	cell temperature [K]
Ncell	number of cells connected in series in a module

on-state resistance of the converter switches, r_{on}, is added together with the line resistance, R. The other parameters in the figure are the ideal voltage at the AC-side of the converter $V_{t,abc}$, the converter gating/switching signals, m_{abc}, the line inductance, L, the line current, i_{abc}, and the voltage at the PCC, $V_{s,abc}$. The figure also depict the power extraction from the PV-array, P_{ext}, and the power delivered to the AC-system, P_t. Changes in V_{DC} originates from a difference in P_{ext} and P_t, as the energy difference accumulates in the capacitor in the form of an electric field.

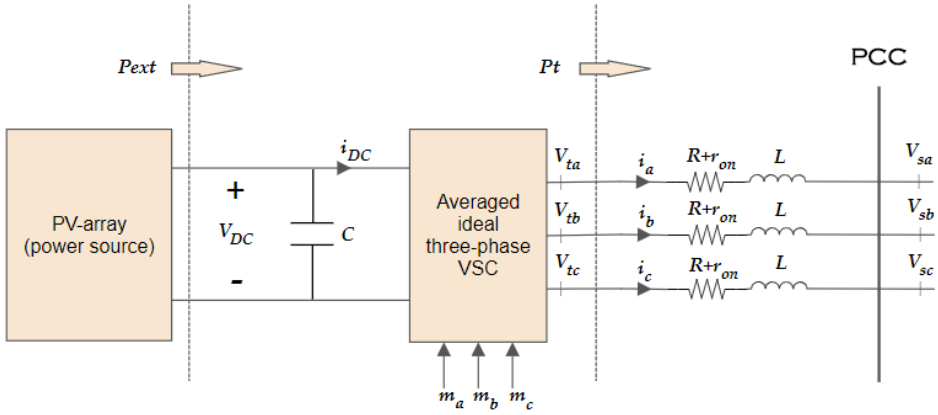

Figure 3.5: *PV-array feeder, consisting of a PV-array, a DC-link capacitor, a VSC, and a low-voltage distribution line.*

3.1.3 Storage battery model

The microgrid storage battery is modelled as a lithium-ion battery. The Simulink Simscape library includes a generic dynamic model of lithium-ion batteries, and Figure 3.6 shows its equivalent circuit model. A controlled voltage source represents

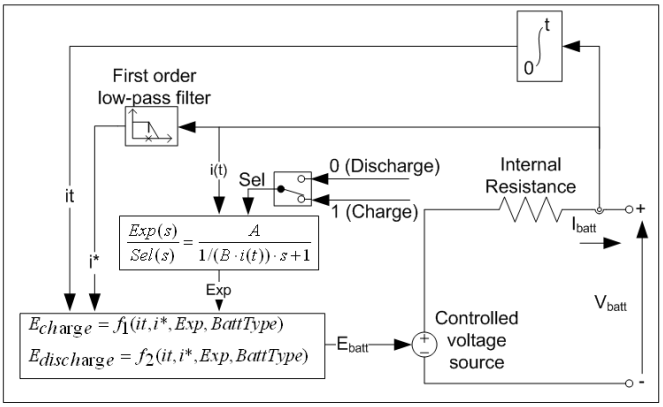

Figure 3.6: *Equivalent circuit model of the lithium-ion battery. The model is based on a controlled voltage source in series with a resistor. The value of the internal voltage source varies, representing the internal voltage dependency on the battery state of charge.*

the internal voltage of the battery, E_{batt}, and the series resistor represent the internal resistance of the battery. As the internal voltage of a battery depends on its state of charge, E_{batt} is continuously updated by the functions f_1 and f_2, for charging and discharging of the battery, respectively. f_1 and f_2 are given by

$$f_1 = E_0 - K\frac{Q}{Q-it}i^* - K\frac{Q}{Q-it}i + A^{-Bit}, \tag{3.3a}$$

and

$$f_2 = E_0 - K\frac{Q}{it+0.1Q}i^* - K\frac{Q}{Q-it}i + A^{-Bit}, \tag{3.3b}$$

where E_0 is a constant voltage, K is a polarization constant in ohms, i^* is the low frequency current dynamics in ampere, i is the battery current in ampere, it is extracted capacity in ampere-hours, Q is the maximum battery capacity in ampere-hours, A is an exponential voltage term in volts, and B is an exponential capacity term in $[Ah]{-}1$. Parameters and characteristic discharge curve of the installed lithium ion battery are listed in Appendix C.

Connecting the storage battery to the PCC

The storage battery is also connected to the PCC by a three-phase feeder line, and interfaced by a VSC, its schematics illustrated in Figure 3.7. The voltage on the DC-side terminals of the converter, V_{DC}, is stabilized by the storage battery, and a large DC-side capacitor is therefore not necessary. A three-phase shunt capacitor, C_f, is connected on the AC-side of the system. The storage battery performs voltage control during isolated operation of the microgrid, and the shunt capacitors ensure that the *RL*-branch is terminated to a node with some degree of voltage support. The shunt capacitors also provide a low-impedance path for switching current harmonics generated by the VSC, and thus, prevents them from penetrating into the load. Without the shunt capacitors, harmonic distortion of load voltage (PCC voltage), $V_{s,abc}$, will significantly depend on the load impedance at the switching frequency and its harmonics [23].

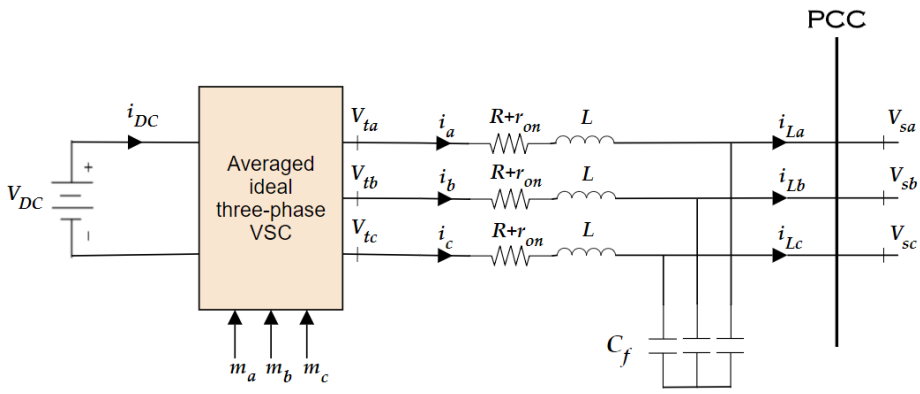

Figure 3.7: *Storage battery feeder model.*

3.1.4 Load model

Two different loads are utilized in the simulations. As seen in Figure 3.8, load 1 is a series ohmic (R)-load, while load 2 is a series ohmic and inductive (RL)-load. They are assumed to be balanced three phase loads, described by Equations 3.4 and 3.5, respectively. The loads are connected to the PCC through separate switches. Under the no-load condition, both switches are in open position. During the partially loaded condition, switch 1 is closed, while switch 2 remains open. During the fully loaded condition, both switches are closed. The loads are not modelled to be responsive to control signals. This is due to DSR and fast load shedding being part of a higher level control (local area control), associated with a time scale ranging from seconds to minutes, while this work focus on device level control, on the time scale of milliseconds.

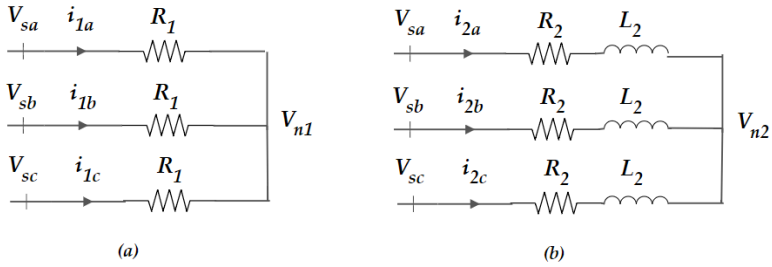

Figure 3.8: *(a) Load 1, a series R-load. (b) Load 2, a series RL-load.*

Load 1 can be described by the three-phase set of equations

$$R_1 i_{1a} = V_{sa} - V_{n1}, \tag{3.4a}$$

$$R_1 i_{1b} = V_{sb} - V_{n1}, \tag{3.4b}$$

$$R_1 i_{1c} = V_{sc} - V_{n1}, \tag{3.4c}$$

where R_1 is the load resistance, $i_{1,abc}$ is the load current, $V_{s,abc}$ is the voltage at the PCC, and V_{n1} is the voltage at the neutral. Load 2 is described by

$$L_2 \frac{di_{2a}}{dt} = -R_2 i_{2a} + V_{sa} - V_{n2}, \tag{3.5a}$$

$$L_2 \frac{di_{2b}}{dt} = -R_2 i_{2b} + V_{sb} - V_{n2}, \tag{3.5b}$$

$$L_2 \frac{di_{2c}}{dt} = -R_2 i_{2c} + V_{sc} - V_{n2}, \tag{3.5c}$$

where R_2 is the load resistance, L_2 is the load inductance, $i_{2,abc}$ is the load current, $V_{s,abc}$ is the voltage at the PCC, and V_{n2} is the voltage at the neutral.

3.1.5 Distribution grid model

The entire microgrid is connected to the main utility through a switch at the PCC. The utility is modelled as a constant voltage source, $V_{g,abc}$, behind a Thevenin impedance. This means that the distribution grid is assumed to constitute a balanced three-phase AC system with constant nominal frequency. When the switch is in closed position, the dynamics of the utility is described by

$$L_{th}\frac{di_a}{dt} = -R_{th}i_a + V_{sa} - V_{ga} - V_{null}, \tag{3.6a}$$

$$L_{th}\frac{di_b}{dt} = -R_{th}i_b + V_{sb} - V_{gb} - V_{null}, \tag{3.6b}$$

$$L_{th}\frac{di_c}{dt} = -R_{th}i_c + V_{sc} - V_{gc} - V_{null}, \tag{3.6c}$$

where L_{th} is the Thevenin inductance, R_{th} is the Thevenin resistance, i_{abc} is the line current in the distribution feeder line, $V_{s,abc}$ is the voltage at the PCC of the microgrid, $V_{g,abc}$ is the voltage source of the distribution grid (the closest distribution transformer), and V_{null} is the voltage at the neutral. The position of the switch is controlled by a mode signal. When islanding is desirable, the mode signal gives the command of opening the switch. At the same time, the mode signal commands the control system to make the proper changes from P/Q control to V/f control of the master unit, *i.e.* the storage battery.

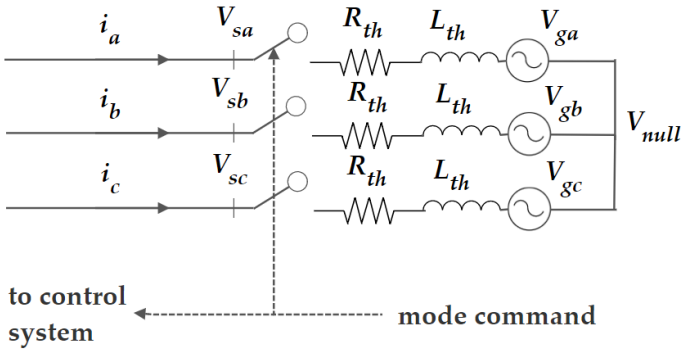

Figure 3.9: *Schematic diagram of the distribution grid model.*

3.2 Choice of control method

3.2.1 Control strategy

The strategy of choice has been the master-slave, as this is the most commonly used strategy for controlling small microgrids (<2 MW). Further, the storage battery was chosen to be the master, and the PV-array was chosen to be the slave. This choice is supported by the notions that i) the storage battery output is significantly more controllable, and ii) one would want the PV-array to pursue maximum power point tracing, (which can only be achieved under P/Q control, and not under V/f control).

A current controller is present in all controlled elements. Upon the current controller, either power control or voltage control are build. This has been realized utilizing known strategies from the control of VSC. Reference [23] is a textbook dedicated to the use of voltage-source converters in power systems. All equations put forth in Chapter 4 and Chapter 5 can be found in their non-per-unitized form in this textbook.

Maximum power point tracing of the PV-array was achieved by making additions to the power controller of the array. The additions involved a perturb-and-observe (P&O) algorithm to identify the terminal voltage that optimizes the efficiency of the array, V_{mp}. Benefits with the P&O are ease of implementation, and that the only measurements needed are the voltage and current outputs of the array. Measurements of irradiance and temperature are not needed. This is beneficial, as such measurements usually are too expensive for the application. Further, such calculation of V_{mp} also require accurate parameters for the PV array, which may not be adequately known [34]. A downside with P&O is that it oscillates around the optimal voltage in steady-state operation. It can also track in the wrong direction, away from the optimal power point, under rapidly increasing or decreasing irradiance levels [34]. The algorithm used was adapted from the Mathworks example of a 250 kW grid-connected PV-array system.

3.2.2 Per-Unit system

The control system is developed in a per-unitized form. Thus, all equations from the above mentioned textbook are converted to the per-unit system, and the derivation can be found in Appendices. Further, all measurements are converted to the per-unit system before being processed. Utilizing this system is convenient, as normalizing units to a common base yields important information about relative magnitudes. Moreover, it makes the model easily scalable. This is beneficial if one, subsequent to this work, want to adopt the model to represent a larger or smaller microgrid. The utilized base values are listed in Appendix A.

3.2.3 The dq-reference frame

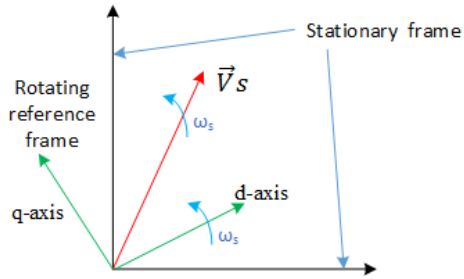

Figure 3.10: *Stationary and rotating coordinate frames.*

The control is performed in the *dq*-frame. The *dq*-frame is a rotating reference frame, with a rotational speed that matches the electrical frequency of the AC-system. This frame is commonly used in the analysis of three-phase circuits, enabling AC waveforms to be represented in the form of DC signals. As known, one can represent a three-phase AC circuit with a set of three rotating vectors. The three vectors can be summed (each vector weighted with its position in space) to a single space-phasor. The space-phasor rotate in the counter-clockwise direction with the angular velocity of the AC system angular electrical velocity, ω_s. An illustration of the space-phasor $\overrightarrow{V}_s$ in the stationary and the rotating frame is depicted in Figure 3.10. As seen from the figure, the *d*- and *q*-axis components of $\overrightarrow{V}_s$ will be stationary with perfect synchronization between the rotating frame and the space-phasor velocities. The relation between the amplitude of the PCC voltage, $\hat{V}_s$, in the abc-frame and the *dq*-frame are given by

$$\hat{V}_s = \sqrt{V_{sd}^2 + V_{sq}^2}, \tag{3.7}$$

where $\hat{V}_s$ is the length of $\overrightarrow{V}_s$, and V_{sd} and V_{sq} are the *d*- and *q*-axis components of $\overrightarrow{V}_s$. Compared with control in the stationary frame, *dq*-frame control reduces the number of dynamic systems to be controlled from three (the three phases of the AC system) to two (the *d*- and *q*-axis components). Moreover, instantaneous decoupled control of the real- and reactive power exchanged between the DC and the AC systems are enabled. Its most significant merit may be that all control variables, (feedback measurement signals, feed-forward signals, and control signals) are DC quantities when the system is in steady-state. This significantly reduces the complexity of the control design.

When the microgrid operates in isolated mode, the VSC dictates the frequency of the microgrid, and is set constant to 50 Hz. Thus, the angular velocity of the *dq*-frame is also set to 50 Hz. In grid connected operation, however, the frequency of the microgrid voltage is dictated by the distribution grid, and may deviate slightly from nominal ($\pm$ 0.1 Hz in the legal region [35]). Obtaining a *dq*-frame that matches the angular speed of the AC system therefore requires a synchronization mechanism. This is not needed in *abc*-frame control, and can be considered a demerit of the *dq*-frame control [23]. Synchronization of the *dq*-frame is achieved by *phase locking*. With phase locking, $\overrightarrow{V}_s$ is synchronized with the *d*-axis of the

rotating frame. Thus, in steady state,

$$(V_{sd}, V_{sq}) = (\hat{V}_s, 0). \tag{3.8}$$

Further details of how the angle for the dq-frame is obtained, both during grid-connected and island operation, is described in Appendix D.

3.2.4 Tuning of regulator gains

The control system involves the use of several proportional-integral (PI) regulators. Two gains must be tuned in each regulator, respectively, the proportional and the integral gain. Initially, the gains were set by utilizing the known tuning methods of *modulus optimum* and the *symmetrical optimum*. Some of the regulator gains was somewhat adjusted thereafter, based on system tests.

Chapter 4

PV-array control

This chapter outlines the development of MPPT of the PV-array. The objective of the control system is to trace the maximum power output of the given operating condition (irradiance), optimizing the efficiency of the PV-array. With reference to Figure 3.4, the maximum power point is when $V_{DC} = V_{mp}$. The control system is a cascaded system of multiple controllers. Each part will be described individually, and the performance of the complete system is reviewed in the end. Simulations of PV-array operation without the storage battery have been conducted. This involves both grid-connected operation and stand-alone operation.

4.1 Outline of control steps

The main objective is to perform MPPT of the PV-array unit, which is an extension to P/Q control. The P/Q control is based on an inner current control loop (No. 4 in the list below) and an outer power control loop (No. 3). MPPT is achieved by implementing an additional DC-side voltage controller (No. 2), and a system that calculates the optimal DC-side voltage, V_{mp} (No. 1). The steps of the control are as following, see also Figure 4.1:

1. V_{mp} is calculated. This is done without measuring the solar irradiation, based on a perturb-and-observe technique.
2. V_{mp} is sent as input to the DC-side voltage controller, who adjust the reference power, $P_{s,ref}$, based on this. $P_{s,ref}$ is adjusted so that, if $V_{DC} < V_{mp}$ the reference power is decreased. If $V_{DC} > V_{mp}$, the reference power is increased.
3. $P_{s,ref}$ is sent to the power controller together with the reference for reactive power, $Q_{s,ref}$. The PV-array is operated at unity power factor, thus $Q_{s,ref} = 0$. The power controller adjust the reference currents, $i_{d,ref}$ and $i_{q,ref}$ based on the input.

4. $i_{d,ref}$ and $i_{q,ref}$ are sent to the current controller, who adjust the converter gating/switching signals, m_{dq}, based on this. It should be remembered that the gating/switching signals are scaling factors who decide the voltage at the AC-side of the converter, $V_{t,abc}$. Varying the magnitude of $V_{t,abc}$ results in more or less power, P_t, being released from the DC-side capacitor, C. This, in turn, affect V_{DC}, and the control loop is complete.

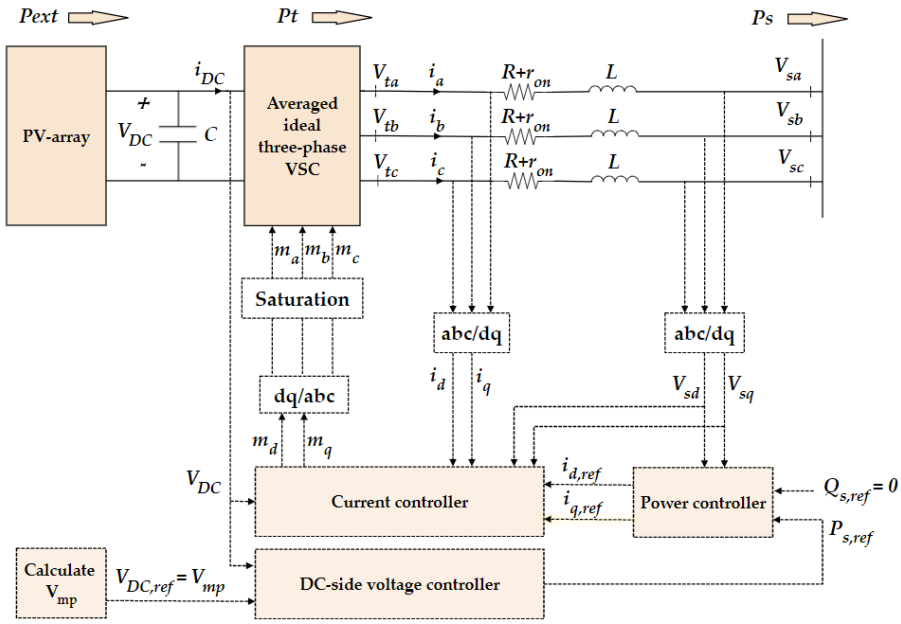

Figure 4.1: *Schematic diagram of the controlled PV-array. Solid lines indicate power lines, while dotted lines indicate measurements/control signals.*

In addition to the reference inputs, each controller also inputs measurement signals from various places in the system. Both measurement signals and control signals are indicated by dotted lines in Figure 4.1. It is illustrated how the AC measurement signals are transformed from the stationary to the rotating frame by means of a *abc/dq*-transformation. The inverse transformation is performed on m_{dq} before it is sent to the VSC. To protect the VSC from over-current and over-voltage conditions, $i_{dq,ref}$ and m_{abc} are limited by saturation blocks. The power flow at various places in the system is shown. P_{ext} is the power extracted from the PV-array. This is the power that is maximized when $V_{DC} = V_{mp}$. Further, P_s is the power sent to the PCC. This is the power that is regulated by the control system. P_t is the power flowing from the DC- to the AC-side of the converter. In the development of the DC-side voltage controller, the assumption that $P_t = P_s$ is used.

4.2 Control system development

The development of each of the four parts in the control system will be described individually. The focus is not on the derivation of equations (*e.g.* transformation to the *dq*-frame, per-unitizing, *etc*). Rather, the focus is on identifying important system properties that can be read from the final equations, and how these properties are decisive to the control design. The time domain equations will be analyzed in parallel with their Laplace domain equivalents. When beneficial, the Laplace domain equations are presented in the form of block diagrams.

4.2.1 The current controller

Based on reference current inputs, $i_{dq,ref}$, the current controller performs changes to the converter gating/switching signals, m_{dq}, as a means to achieve the desired line current. In other words, the current controller performs current reference tracking, ensuring that $i_d \approx i_{d,ref}$ and $i_q \approx i_{q,ref}$. A *dq*-frame description of the PV-array line current dynamics is given by Equation 4.1, and the equivalent block diagram is shown in Figure 4.2. Nominal AC system frequency is assumed. All parameters and variables (except time) are in per units. A non per-unitized version of Equation 4.1 is derived in Reference [23] (pages 208-219), and the transformation to the per-unit system of choice is provided in the Appendix B. i_{dq} are given by

$$\frac{L}{\omega_b}\frac{di_d}{dt} = L\omega_0 i_q - (R + r_{on})i_d + V_{DC}(t)m_d(t) - V_{sd}, \tag{4.1a}$$

$$\frac{L}{\omega_b}\frac{di_q}{dt} = -L\omega_0 i_d - (R + r_{on})i_q + V_{DC}(t)m_q(t) - V_{sq}, \tag{4.1b}$$

where ω_b is the angular velocity base value, ω_0 is the nominal electrical angular velocity, L is the line inductance, R is the line resistance, r_{on} is the on-state resistance of the VSC switches, V_{DC} is the DC-side voltage, V_s is the PCC voltage, and m_{dq} are the VSC switching signals. Subscript d and q refers to the d- and q-axis components of the variables, respectively. Equation 4.1 (and the block diagram) provide a description of how the line current changes with time, and notably, which components contribute to this change. Important realizations are that:

1. The converter switching signals, m_d and m_q, contribute to i_d and i_q dynamics. This implies that the current can be regulated by the signals m_d and m_q.

2. Current dynamics also depend on V_{DC}, V_{sd} and V_{sq}. This implies that i_d and i_q may drop or rise even without the control signals initializing the change. V_{DC}, V_{sd} and V_{sq} are disturbance variables, *i.e.* not controllable, and should be counteracted.

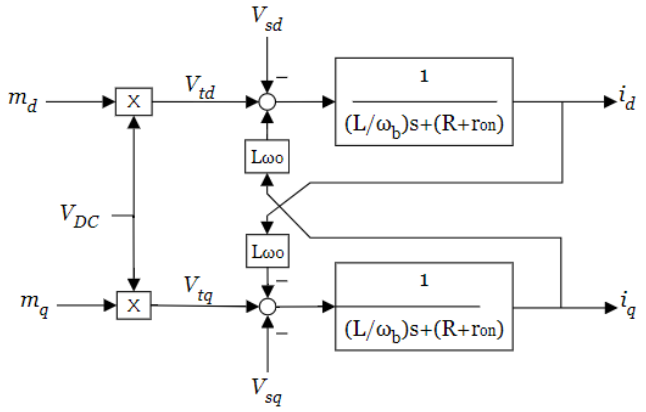

Figure 4.2: *Block diagram of PV-array line current dynamics.*

3. The dynamics of i_d and i_q are cross-coupled. This implies that a change in i_d impose a change in i_q. As long as the current are coupled, it will be impossible to change i_d without also alter i_q, and vice versa. The current should therefore be decoupled.

The disturbance variables and the cross-coupling interfere with the current control, and should be counteracted. Preferably, the current should only depend on a control signal. It should be remembered that, as m_d and m_q are control signals, they can be defined in any way seen fit. A useful way to define, m_d and m_q is

$$m_d = \frac{1}{V_{DC}}(u_d - L\omega_0 i_q + V_{sd}), \tag{4.2a}$$

$$m_q = \frac{1}{V_{DC}}(u_q + L\omega_0 i_d + V_{sq}), \tag{4.2b}$$

where u_d and u_q are two new control signals, and the variables V_{DC}, i_d, i_q, V_{sd} and V_{sq} are all measurements of the physical values. With this, the disturbance variables and the current cross-coupling are counteracted by automatic adjustments in m_d and m_d. If V_{sd} drops (by *e.g.* the connection of a load), m_d immediately drops as well, balancing the right hand side of Equation 4.1, and i_d stays fixed. Inserting Equation 4.2 into Equation 4.1 gives

$$\frac{L}{\omega_b}\frac{di_d}{dt} = -(R + r_{on})i_d + u_d, \tag{4.3a}$$

$$\frac{L}{\omega_b}\frac{di_q}{dt} = -(R + r_{on})i_q + u_q, \tag{4.3b}$$

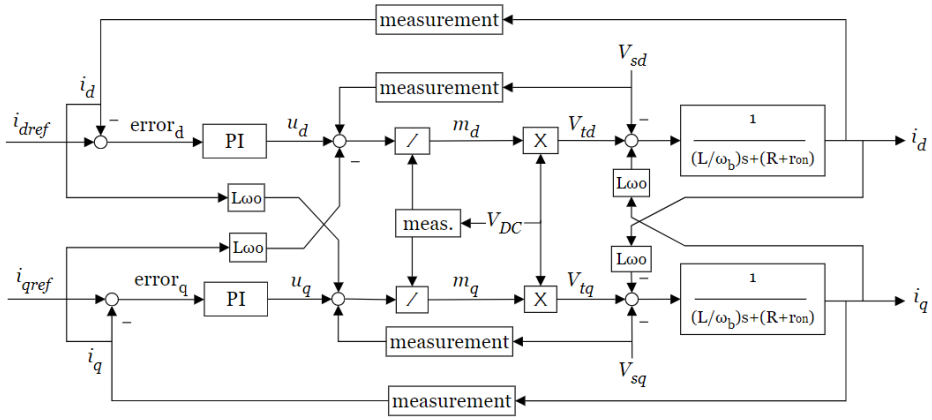

Figure 4.3: *Block diagram of the controlled line current dynamics.*

which represent two decoupled equations, where the only variables affecting the current dynamics are the control signals u_d and u_q. Since i_d and i_q are DC quantities in steady state, two PI-regulators can produce u_d and u_q and achieve reference tracking with zero steady-state error. One PI regulator process the error signal $(i_{d,ref} - i_d)$, and provide u_d for reference tracking of the d-axis current. The other PI-regulator process the error signal $(i_{q,ref} - i_q)$, and provide u_q for reference tracking of the q-axis current. As the systems in the d- and q-axis control loops are identical, the two PI-regulators can also be identical. The complete current controller is shown in the block diagram of Figure 4.3. It can be seen that the current controller incorporates Equation 4.2, and that u_d and u_q are the outputs of two parallel PI-regulators. It should be noted that the signals u_d and u_q serve the purpose of adapting to changes in the reference signals, $i_{d,ref}$ and $i_{q,ref}$. The other feedback measurement signals serve the purpose of counteracting all other disturbances that affect the current dynamics. The block diagram of Figure 4.3 is somewhat complicated, but (as the control signals cancel most of the physical signals) can be re-written to a simplified form shown in Figure 4.4. This block is seen to be consistent with Equation 4.3.

The block diagram is a description of how the currents i_d and i_q behave when the current controller is added to the system. It can be seen that i_d and i_q have decoupled dynamics. It can also be seen that the inputs $i_{d,ref}$ and $i_{q,ref}$ (which are control signals) affect the actual (physical) current. Further, it can be seen that the disturbance variables no longer have a part in the equation. Expectations that can be drawn from this are that:

1. i_d and i_q can be regulated separately, respectively, by $i_{d,ref}$ and $i_{q,ref}$.
2. i_d and i_q will not disturb each other when regulated.
3. Even if the DC-side voltage or the PCC voltage change, they will not affect the line current.

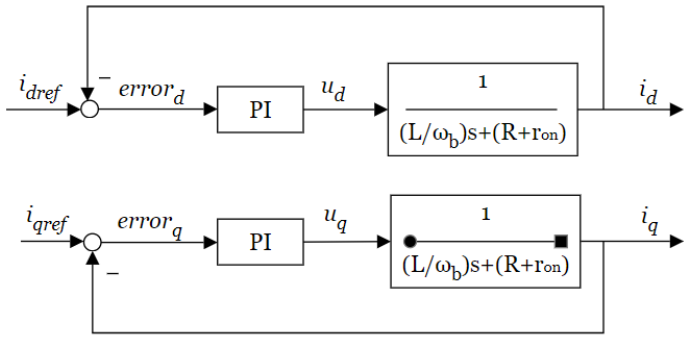

Figure 4.4: *Simplified version of the block diagram of Figure 4.3.*

To what degree these expectations prove correct dependent on the validity of the adopted model. This will become evident when testing the control system.

Regulator gains

The two PI-regulators in the current controller, k_d and k_q, are identical. They are given by

$$k_d(s) = k_q(s) = \frac{k_p s + k_i}{s}, \tag{4.4}$$

where k_p and k_i are, respectively, the regulators proportional and integral gains. The gains are tuned with the method of modulus optimum. The method is elaborated in Appendix F. In brief words, the nominator of the PI-regulator is sat to eliminate the plant pole. With this, the closed-loop transfer function of the current controller, $G_i(s)$, becomes a first-order transfer function given by

$$G_i(s) = \frac{i_d}{i_{d,ref}}(s) = \frac{i_q}{i_{q,ref}}(s) = \frac{1}{\tau_i s + 1}, \tag{4.5}$$

where τ_i is the time constant of the closed-loop system, and is a design choice. τ_i should be made small for fast current control. However, it should be made adequately large such that the switching harmonics from the VSC do not interfere with the current control. τ_i is typically selected in the range of $0.5 - 5$ ms [23] (a high switching frequency permits a smaller τ_i). In this case, τ_i and the regulator gains are selected to

$$\begin{aligned} \tau_i &= 0.5e^{-3} \quad [\text{s}], \\ k_p &= 0.1250 \quad [\text{rad}], \\ k_i &= 4.0750 \quad [\text{rad/s}]. \end{aligned} \tag{4.6}$$

The current controller step response is shown in Figure 4.5. It can be verified to be the response of a first-order transfer function with time constant approximately 0.5

ms. An illustration of how the current controller is implemented in the Simulink environment is depicted in Appendix.

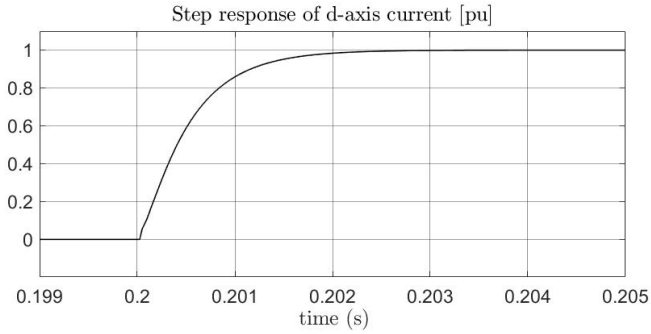

Figure 4.5: *Step response of current controller, d-axis current. The unit step is applied at time t = 0.2 seconds.*

4.2.2 The power controller

Based on the input reference power signals, $P_{s,ref}$ and $Q_{s,ref}$, the power controller determines $i_{d,ref}$ and $i_{q,ref}$. The PV-array is operating at a unity power factor. Therefore, $Q_{s,ref} = 0$. It should be mentioned that the same power controller will be applied to the storage battery. In that case, $Q_{s,ref}$ will be tested for other values than zero. The design of the power controller is simpler than that of the current controller. It is also designed without the use of PI-regulators. The real and reactive power to the PCC, P_s and Q_s, can be described by

$$P_s(t) = V_{sd}(t)i_d(t) + V_{sq}(t)i_q(t), \tag{4.7a}$$

and

$$Q_s(t) = -V_{sd}(t)i_q(t) + V_{sq}(t)i_d(t), \tag{4.7b}$$

where V_{sd} and V_{sq} are the d- and q-axis components of $V_{s,abc}$. i_d and i_q are the d- and q-axis components of i_{abc} (see Figure 4.1). A non per-unitized version of this equation is provided in Reference [23] (page 218), and the transformation to the per-unit system of choice is provided in Appendix B. If the dq-frame is synchronized with the AC-system, $V_{sq} = 0$. Thus, assuming steady-state of the PLL, P_s and Q_s, can be described by

$$P_s(t) = V_{sd}(t)i_d(t), \tag{4.8a}$$

and

$$Q_s(t) = -V_{sd}(t)i_q(t). \tag{4.8b}$$

It can be seen that V_{sd} is the only disturbance signal present. The disturbance from V_{sq} is regarded as negligible, and only the disturbance from V_{sd} is accounted for in the power controller design. This is done by defining

$$i_{d,ref} = \frac{1}{V_{sd}} P_{s,ref}, \tag{4.9a}$$

and

$$i_{q,ref} = -\frac{1}{V_{sd}} Q_{s,ref}, \tag{4.9b}$$

where V_{sd} in the equation is the measurement of the physical voltage. It can be seen that when the current equal its reference, the powers will also equal their references. The block diagram of the power controller is shown in Figure 4.6. It

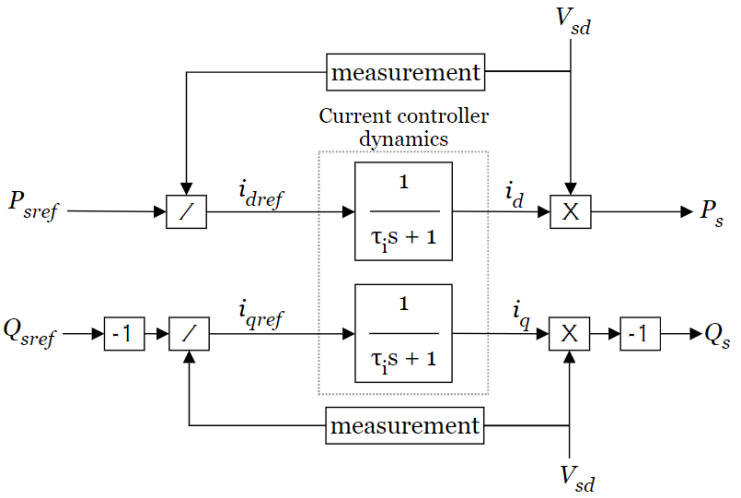

Figure 4.6: *Block diagram of the power controller, assuming that the dq-frame is perfectly synchronized with the AC system.*

is seen that the measurement signal of V_{sd} cancel the disturbance from V_{sd} in the physical system. The -1 multiplication of $Q_{s,ref}$ cancel the negative sign in Equation B.2b. With the assumption that the control signals perfectly cancel the disturbances, the power controller transfer function, $G_P(s)$, is reduced to equal the current controller transfer function. That is,

$$G_P(s) = \frac{P_s(s)}{P_{s,ref}} = \frac{1}{\tau_i s + 1} = G_i(s), \tag{4.10a}$$

and

$$G_P(s) = \frac{Q_s(s)}{Q_{s,ref}} = \frac{1}{\tau_i s + 1} = G_i(s). \tag{4.10b}$$

However, as seen from the block diagram, the control signals are applied to the left hand side of the current controller. The physical disturbances affect the right hand side of the current controller. If τ_i is small enough, $G_i(s) \approx 1$. In that case, there will be no difference in the physical disturbances and the counteractive measurement signals. This results in $G_P(s) = G_i(s)$. If τ_i is large, the current controller introduce a time lag to the measurement signals, making them differ from the disturbance terms. Thus, the validity of the power controller model decreases as τ_i increases. In the model utilized, $\tau_i = 0.5$ ms, which represent fast current control. The effect of a slow current control is explored under applications. For now, it is expected that the first order model of the power controller is quite accurate. Expectations to the power controller are therefore that:

1. P_s and Q_s can be regulated separately, respectively by $P_{s,ref}$ and $Q_{s,ref}$. Further, they will not disturb each other significantly when changed.
2. P_s will follow the same transient pathway as i_d. Q_s will follow the same transient pathway as i_q. *i.e.* they will stabilize in the same per-unit values, and have the same dynamics towards the new steady-state value (the dynamic of a first order transfer function).
3. Even if the PCC voltage change, it will not significantly disturb P_s and Q_s.
4. Neither are any other variables expected to disturb P_s and Q_s.

As before, the degree to which these expectations prove correct dependent on the validity of the adopted model. This will become evident when testing the control system. In this chapter, the power controller is only tested in combination with the entire MPPT control system. The power controller is also utilized on the storage battery, where its operation is tested more specifically. An illustration of how the power controller is implemented in the Simulink environment is depicted in Appendix E.

4.2.3 The DC-side voltage controller

Based on the input reference voltage, $V_{DC,ref}$, the DC-side voltage controller determines $P_{s,ref}$. The DC-side voltage controller is somewhat more complicated than the power controller. It also incorporates a PI-regulator, which enables reference tracking with zero steady-state error. With reference to Figure 4.1, the DC-side voltage is determined by the dynamics of the large DC-side capacitor, C. The voltage across the capacitor change as a result of differences in P_{ext} and P_t. Any

power extracted from the PV-array not released to the AC-system accumulates in the capacitor in the form of an electric field. As this electric field strengthen or weaken, the voltage increase or decrease. The DC-side voltage is described in per unit by

$$\frac{C}{2\omega_b}\frac{dV_{DC}^2}{dt} = P_{ext} - P_t, \tag{4.11}$$

where ω_b is the angular velocity base value. C is the capacitance, P_{ext} is the power sent into, and P_t is the power released from the DC-side capacitor. The non per-unitized version of this equation is found in Reference [23] (page 201), and the transformation to the per-unit system of choice is provided in the Appendix B. The size of the capacitor decides how much energy is needed to alter the magnitude of V_{DC}. It should be noted that the power controller regulate P_s, and $P_s \neq P_t$, due to dynamics and losses of the feeder line. However, a common simplification is that $P_s = P_t$. With this, the transfer function from P_s to V_{DC}^2 takes the form

$$G_V(s) = \frac{V_{DC}^2(s)}{P_s(s)} = -\Big(\frac{2\omega_b}{C}\Big)\frac{1}{s}. \tag{4.12}$$

Due to the voltage squared in Equation 4.11, V_{DC}^2 will be regulated instead of V_{DC}. Figure 4.7 is a block diagram of the DC-side voltage control loop. As seen from the diagram, the disturbance from P_{ext} is counteracted by a measurement signal in the controller. The figure illustrates how both the reference and the feedback voltage is squared before being processed by the PI-regulator. The -1 multiplication is to compensate the negative sign of $G_V(s)$.

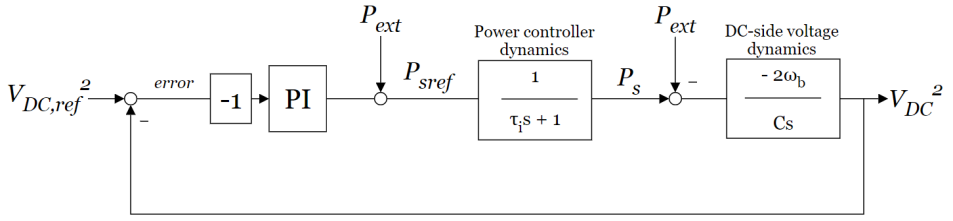

Figure 4.7: *Control block diagram of the DC-side voltage regulation loop based on the simplified model.*

Expectations from the DC-side voltage controller are that:

1. V_{DC} can be controlled to $V_{DC,ref}$ with zero steady-state error.
2. The dynamics of the controller is of higher order than first order.
3. The disturbance from P_{ext} is counteracted.

Regulator gains

As the voltage is a DC-signal, a simple PI-regulator achieves reference tracking with zero steady state error. The regulator, $K_V(s)$, is given by

$$K_V(s) = k_{simp}\frac{s + z_{simp}}{s}, \tag{4.13}$$

where k_{simp} and z_{simp} are the proportional and integral gains, respectively. The regulator gains are tuned according to the *symmetrical optimum* principle, which determines the gains based on a desired phase margin, δ_m. A general recommendation is to have a phase margin above 45° [36]. By choosing a phase margin of 53°, the gains were set to

$$\begin{aligned} k_{simp} &= 7.138 \quad [rad], \\ z_{simp} &= 223.9 \quad [rad/s]. \end{aligned} \tag{4.14}$$

An illustration of how the DC-side voltage controller is implemented in the Simulink environment is depicted in Appendix E.

Limitations of the simplified model

It is worth looking in to the implications of equating $P_s = P_t$. A more complicated model of the voltage dynamics is derived in Reference [23] (pages 191-194). The model describes P_t in terms of P_s more accurately. This provides a non-linear model that must be linearized around a given operating point, P_{s0}. Assuming $Q_s = 0$, the transfer function from $\tilde{P}_s$ to $\tilde{V}_{DC}^2$ in the more accurate model becomes

$$G_V(s) = \frac{\tilde{V}_{DC}^2(s)}{\tilde{P}_s(s)} = -\Big(\frac{2\omega_b}{C}\Big)\frac{\tau s + 1}{s}, \tag{4.15}$$

and

$$\tau = \frac{LP_{s0}}{\omega_b V_{sd}^2}, \tag{4.16}$$

where the additional parameters, τ and L, are the system time constant, and the feeder line inductance. Superscripts $\sim$ and subscripts 0 indicate, respectively small-signal perturbations and steady-state values of the variables. It can be seen that τ is a function of the operating point. Further it can be seen that the simplified model corresponds to the more accurate model linearized around the operating point $P_{s0} = 0$. However, the simplified model fails to notice that an operating condition $P_{s0} \neq 0$ causes a shift in the phase of $G_V(s)$. If P_{s0} is positive, τ is positive, and adds to the phase of $G_V(s)$. On the other hand, if P_{s0} is negative, τ becomes negative, and result in a reduction in the phase of $G_V(s)$. A phase

reduction is unwanted, as this moves the system towards instability. Luckily, the PV-array is normally not operated with negative powers, as the PV array is the generating unit.

4.2.4 Calculating optimal DC-side voltage

The optima DC-side Voltage, V_{mp}, is found by utilizing a perturb-and-observe algorithm. The algorithm is integrated into the Simulink model through a MATLAB-function block. The inputs to the MATLAB function are an initial reference voltage, $V_{DC,ref}$, and the measured voltage and current outputs from the PV-array, I_{DC} and V_{DC}. The output is an updated $V_{DC,ref}$ that is adjusted by a small increment, $\Delta V_{DC,ref} = 0.015$ pu. If the power output from the array increases, further adjustments in that direction are made. If the power decreases, adjustment in the opposite direction are made. The algorithm is simple, and the MATLAB script utilized is included in Appendix E. The method has been referred to as a hill climbing method. With reference to Figure 3.4, it can be seen as a nice analogy, because it is based on the rise of the curve of P_{ext} for voltages below the maximum power point, and the fall above that point. The algorithm constantly searches for V_{mp}, and finds it (eventually) without having to measure the solar irradiance. The increment size and the time between each update decide how fast $V_{DC,ref}$ track V_{mp}. The increment size also give rise to ripples in the steady state value of $V_{DC,ref}$. Thus, it should not be made too large.

4.3 Performance of the controlled PV-array

In this section, the behaviour of the controlled PV-array is analyzed. The objective of the control system is to trace the maximum power output of the given operating condition (irradiance), optimizing the efficiency of the PV-array. As known, the maximum power point is when $V_{DC} = V_{mp}$. The performance of the PV-array is analyzed both connected to the distribution grid, and in stand-alone operation. The storage battery is not included at this point. The distribution grid is modelled as a strong grid, thus $Z_{th} = 0$.

4.3.1 The PV-array in grid-connected operation

In this scenario, the switch connecting the microgrid with the utility is in closed position. The voltage at the PCC is supported by the grid, and is expected to stay fixed regardless of the amount of power delivered from the PV-array. The PV-array's ability to autonomously make V_{DC} track V_{mp} is tested by making step-changes in the irradiance. The system is operating at full-load condition. Initial irradiance is sat to $10W/m^2$, which charges the DC-link capacitor to $V_{DC} \approx 1.07$ pu. Then, the system is subjected to a sequence of step-changes at the times:

$t = 0.5$ sec: Solar irradiation is step-changed up to $1000W/m^2$.

$t = 1.1$ sec: Solar irradiation is step-changed down to $100W/m^2$.

$t = 1.7$ sec: Solar irradiation is step-changed up to $600W/m^2$.

The time responses of the system is shown in Figure 4.8. Plotted values are the DC-side voltage, V_{DC}, the power extracted from the array, P_{ext}, the power delivered to the AC-system, P_t, the feeder line current, i_{dq}, and the voltage at the PCC, $V_{s,dq}$. It can be observed that:

1. V_{DC} autonomously track V_{mp}. Every time irradiation is step-changed, V_{DC} begins to move in the direction of the new V_{mp}, and settles when it equals this value.

2. As solar irradiation is stepped up from $10W/m^2$ to $1000W/m^2$, it takes approximately 0.4 seconds for V_{DC} to reach the new optimal value.

3. It can be seen that the power output from the array, P_{ext}, steps up at the same time as the irradiance is stepped up. Moreover, it can be seen that as V_{DC} is approaching V_{mp}, the power increases even further. This is most apparent during the time interval from 0.5 to 0.9 seconds. The first (larger) step up is due to higher irradiance, while the second (smaller) increase is the contribution from MPPT. (see also Figure 3.4.)

4. As expected, the voltage at the PCC stays fixated. Instead, the changes in P_{ext} (and P_t) materializes in the form of a change in the line current.

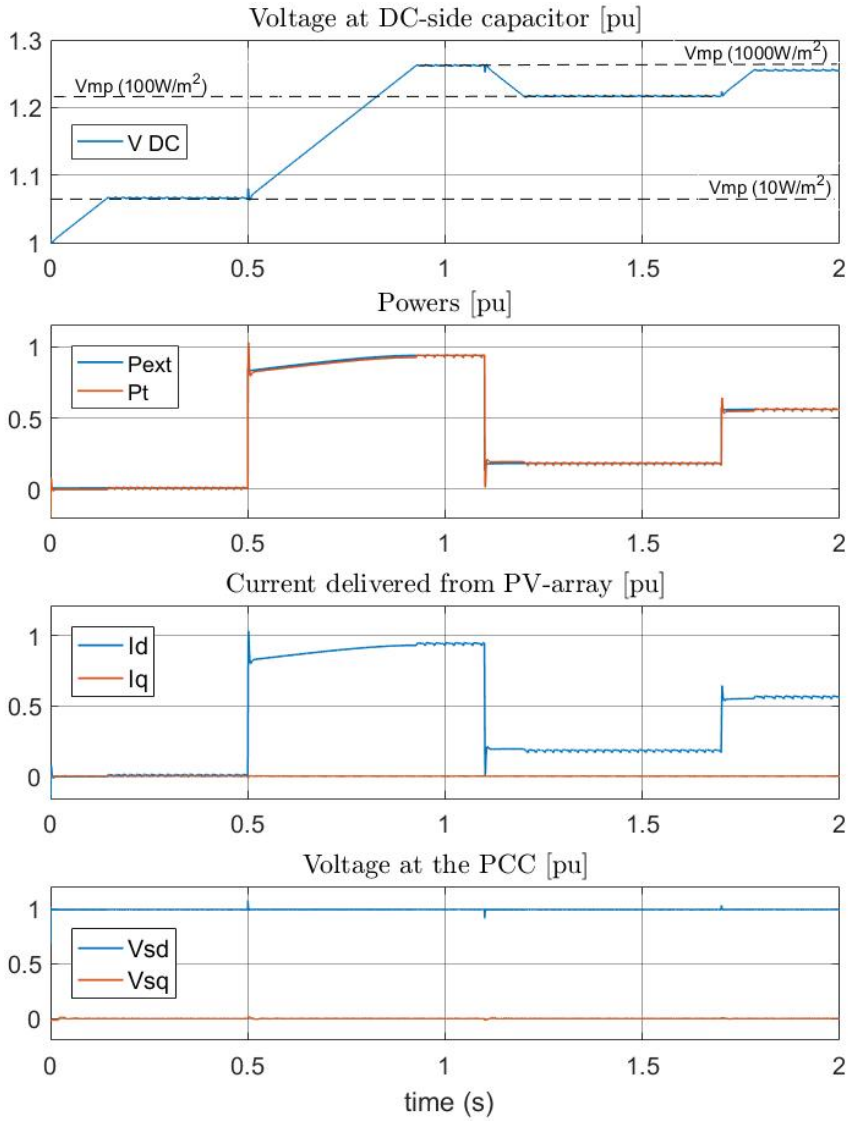

Figure 4.8: *The controlled PV-array feeder; response to step-changes in irradiation during full load and grid-connected operation.*

5. Peaks occur in the DC-side voltage at the instants when the solar irradiance was step-changed. This is due to the increase in P_t lagging the P_{ext}. This lag is associated with the time constant of the DC-side voltage controller. The magnitude of these voltage peaks are not large. Additional system tests confirm that the severity of these peaks increase if the size of the DC-side

capacitor is decreased.

6. There are small ripples in the steady-state DC-link voltage. This is expected, due to the perturb-and-observe technique utilized to search for V_{mp}.

7. i_q is regulated to zero. This is expected, as the array is working at a unity power factor ($Q_{s,ref} = 0$).

A close-up on the powers, P_{ext} and P_t, are shown in Figure 4.9. The figure show more clearly how the increase in V_{DC} is achieved by regulating P_t slightly smaller that P_{ext} (left frame). Similarly, it show how a decrease in V_{DC} is achieved by regulating P_t slightly higher than P_{ext} (right frame). The close-up show more clearly how the response in P_t slightly lag P_{ext}. These lags are what causes the small peaks in the DC-side voltage. It can be concluded that the developed control system enables maximum power point tracing, optimizing the efficiency of the PV-array. The system adapts autonomously and quickly to changes in irradiation, without the need to actually measure the irradiance.

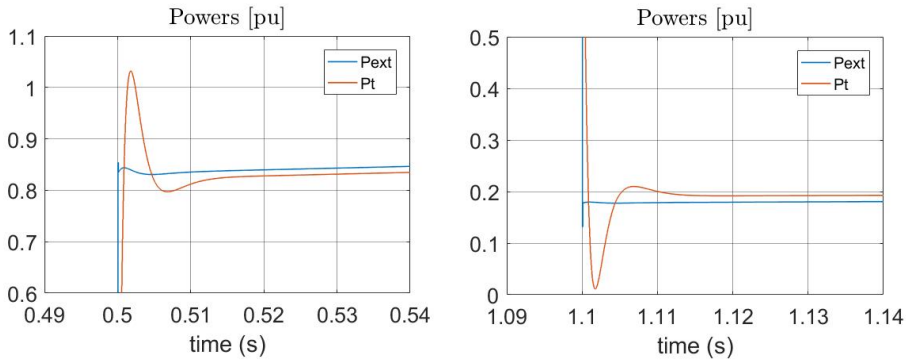

Figure 4.9: *Close-up of P_{ext} and P_t of the controlled PV-array during a) a step-up in solar irradiation, b) a step-down in solar insolation.*

4.3.2 Islanding the PV-array

In this scenario, the switch connecting the microgrid with the utility will be opened. It illustrates the inadequacy of operating the PV-array in stand-alone without any unit (*e.g.* a battery) being in charge of the power balance (*i.e.* conducting voltage control) present. Without any unit performing voltage control, there is no guarantee that the loads will be provided with their requested amount of power. Abundance or insufficiency of power to loads become evident in the form of a voltage at the PCC above or below the nominal voltage. The scenario unfolds as follows: Initially, the system is connected to the distribution grid, operating at full-load condition and with a solar irradiation of $50W/m^2$. This amount of solar

irradiation is not sufficient to cover the loads, and there is an import of power from the distribution grid. The system is subjected to a sequence of changes at the times:

$t = 0.60$ sec: The switch at the PCC is opened, islanding the PV-array.

$t = 0.80$ sec: Solar irradiation is step-changed up to $1000W/m^2$.

$t = 1.10$ sec: Solar irradiation is step-changed down to $200W/m^2$.

$t = 1.40$ sec: Solar irradiation is step-changed up to $600W/m^2$.

The time response of the system is depicted in Figure 4.10. Plotted values are the DC-side voltage, V_{DC}, the power extracted from the array, P_{ext}, the power delivered to the AC-system, P_t, the feeder line current, i_{dq}, and the voltage at the PCC, V_s. The voltage at the PCC is plotted both in terms of the d- and q-axis components, as well as the amplitude, $\hat{V}_s$. It can be observed that:

1. When the distribution grid disconnects, the PV-array undergo a transient condition, and stabilizes in a new operating point.
2. In the new steady-state, $\hat{V}_s$ is below nominal. This is due to the power delivered from the PV-array being insufficient to cover the loads at only $50W/m^2$ irradiation.
3. The current has increased in the new stady-state compared with the old steady-state. This is not due to an increase in P_t (which remains constant), but due to the power being delivered at a lower voltage level.
4. The PV-array control system continues to perform MPPT, also in the stand-alone operation. Thus, the power extracted from the array is still optimized.
5. At $1000W/m^2$ irradiation, there is an abundance of power extracted from the PV-array. $\hat{V}_s$ increases above nominal, so that power is being dissipated in loads at a higher rate than rated/desired.
6. The PCC voltage now has a q-component, $V_{sq} > 0$, meaning that the micro-grid no longer is phase-synchronized with the distribution grid.

It can be concluded that, for stand-alone operation of the PV-array, MPPT cannot be performed without compromising the power quality of the microgrid. When there is limited sun, and an associated power deficit, the voltage drop below nominal. When there is lots of sun, and following power surplus, the voltage rises above nominal. A power surplus might not be that serious. The surplus could be shed, or the loads (if not very sensitive loads) could consume somewhat more than rated. A power deficit represent a larger problem, as failing to deliver power to critical loads is unwanted. More generally, the fact that the voltage is not regulated, but fluctuate as a bi-product of load conditions and solar irradiance is not acceptable. The next chapter is dedicated to the development of the storage battery control system. It is shown that by including a storage battery, the voltage can be regulated while the PV-array performs MPPT, also during isolated operation.

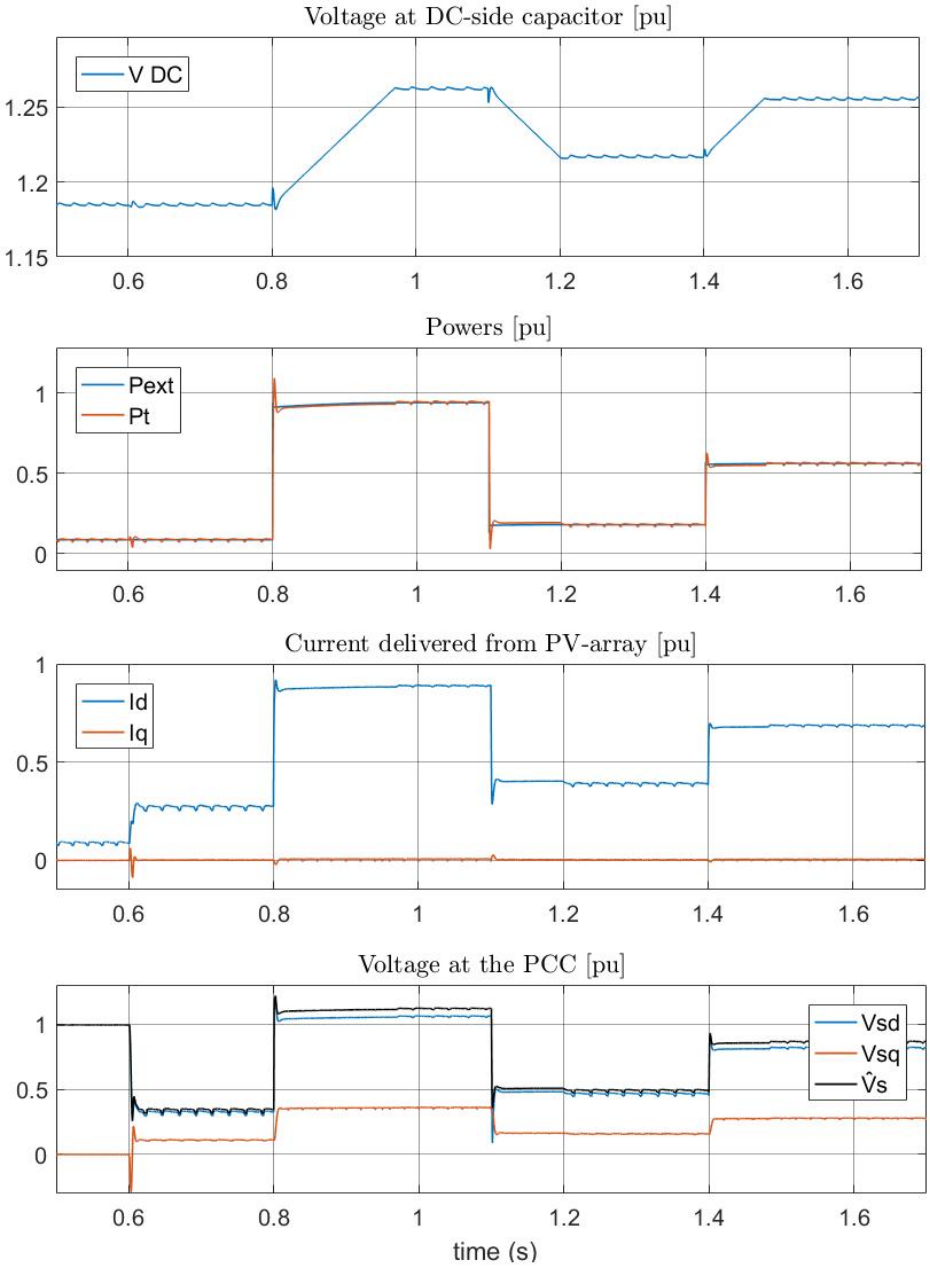

Figure 4.10: *The controlled PV-array feeder responses to step-changes in solar insolation during full load and stand-alone operation.*

Chapter 5

Battery control

This chapter outlines the development and implementation of the storage battery control system. As the storage battery is the master unit of the microgrid, it needs two distinct controllers. The first is the P/Q controller, which is the active controller as long as the microgrid is connected to the distribution grid. The control objective during this operation is to deliver the amount of power 8positive or negative) that is requested from the battery. The second controller is the V/f controller, which is the active controller when the microgrid is islanded. The control objective during this operation is to regulate the amplitude and frequency of the load voltage (PCC voltage), $V_{s,abc}$, in the presence of disturbances in the load current, $i_{L,abc}$. Switching between the controllers is done by the mode command signal. Experiments with storage battery operation without the PV-array have been conducted. This involves both grid-connected operation and stand-alone operation. Finally, the storage battery and the PV-array are combined, and the operation of the complete microgrid is reviewed.

5.1 Outline of control steps

The P/Q control system is based on an inner current control loop and an outer power control loop. The P/Q controller is identical to the one developed for the PV-array in Chapter 4 (as a part of the MPPT), and will not be covered in this chapter. The V/f controller consist of an inner current control loop and an outer voltage control loop. Also the current control loop is identical to the one already developed. Therefore, the only extension is the voltage control loop. Figure 4.1 illustrate the schematics of the storage battery control system. The following list summarize the control for both operating modes:

Grid-connected operation: The multiplexer switches are in upward position, so that $i_{d,ref}$ and $i_{q,ref}$ are fed from the power controller (opposite to what is illustrated in Figure 5.1).

1. The power controller calculates $i_{d,ref}$ and $i_{q,ref}$ based on the input reference powers, $P_{s,ref}$ and $Q_{s,ref}$.
2. The current controller adjust the converter gating/switching signals, m_{dq}, based on $i_{d,ref}$ and $i_{q,ref}$.

Isolated operation: The multiplexer switches are in downward position, so that $i_{d,ref}$ and $i_{q,ref}$ are fed from the voltage controller (as illustrated in Figure 5.1).

1. The voltage controller calculates $i_{d,ref}$ and $i_{q,ref}$ based on input voltages, $V_{sd,ref}$ and $V_{sq,ref}$.
2. The current controller adjust the converter gating/switching signals, m_{dq}, based on $i_{d,ref}$ and $i_{q,ref}$.

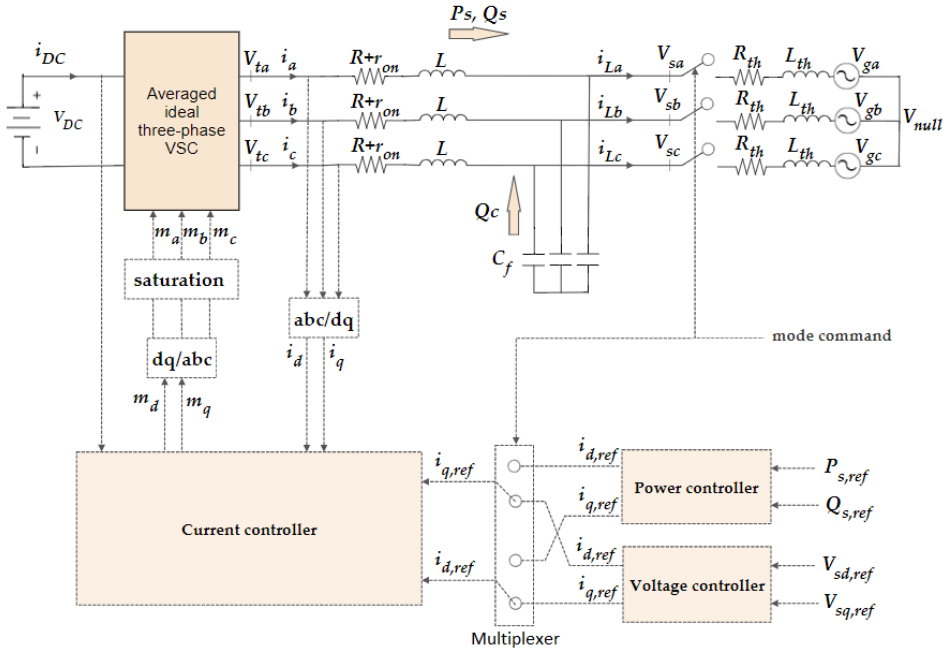

Figure 5.1: *Schematic diagram of storage battery control system. Solid lines indicate power lines, while dotted lines indicate measurements/-control signals.*

In addition to the reference inputs, each controller also inputs measurement signals from various places in the system. Both measurement signals and control signals

are indicated by dotted lines in Figure 5.1. Note that the voltage at the PCC, $V_{s,abc}$ and the load current, $i_{L,abc}$, are also measured, but not depicted in the figure. Note also that other elements connected at the PCC (*e.g.* loads) are not shown in the figure either. P_s and Q_s are the power sent to the PCC from the storage battery. This are the powers regulated by the control system. Q_c is the reactive power flowing from the three-phase shunt capacitor. The total power input to the PCC is therefore $(P, Q) = (P_s, Q_s + Q_c)$.

5.2 Control system development

5.3 The power controller

The power controller is the same controller as developed in the previous chapter. It will not be described again. The expectations to this controller is for clarity repeated:

1. P_s and Q_s can be regulated separately, respectively by $P_{s,ref}$ and $Q_{s,ref}$, and will not disturb each other significantly when regulated.
2. P_s will follow the same transient pathway as i_d. Q_s will follow the same transient pathway as i_q. *i.e.* they will stabilize in the same per-unit values, and have the same dynamics towards the new steady state value (the dynamic of a first order transfer function).
3. Even if the PCC voltage change, it will not significantly disturb P_s and Q_s.
4. Neither are any other variables (*e.g.* the load condition) expected to affect the dynamic response of P_s and Q_s.

The controller performance is tested at the end of this chapter, during the grid-connected operation of the storage battery.

5.3.1 The voltage controller

Based on the input references, $V_{sd,ref}$ and $V_{sq,ref}$, the voltage controller determines $i_{d,ref}$ and $i_{q,ref}$. As the relation between the amplitude of the PCC voltage in the *abc*-frame and the *dq*-frame is given by

$$\hat{V}_{s,abc} = \sqrt{V_{sd}^2 + V_{sq}^2}, \tag{5.1}$$

nominal voltage at the PCC is achieved by regulating

$$(V_{sd}, V_{sq}) = (1\text{pu}, 0). \tag{5.2}$$

With reference to Figure 4.1 the voltage at the PCC equal the voltage across the three-phase shunt capacitor, C_f. A *dq*-frame description of the voltage dynamics is

given by Equation 5.3, and the equivalent block diagram is shown in Figure 5.2. All parameters and variables (except time) are in per units. A non per-unitized version of the equation is derived in Reference [23] (pages 248-249) and the transformation to the per-unit system of choice is provided in the Appendix B. The dynamics of V_{sd} and V_{sq} are given by

$$\frac{C_f}{\omega_b}\frac{dV_{sd}}{dt} = C_f(\omega V_{sq}) + i_d - i_{Ld}, \tag{5.3a}$$

$$\frac{C_f}{\omega_b}\frac{dV_{sq}}{dt} = -C_f(\omega V_{sd}) + i_q - i_{Lq}, \tag{5.3b}$$

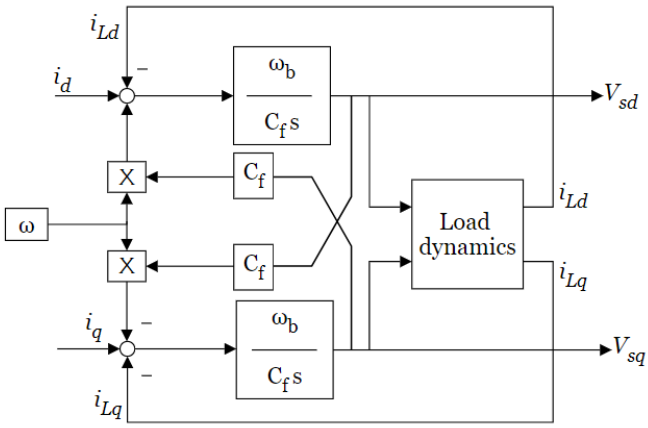

Figure 5.2: *Laplace domain block diagram of PCC voltage dynamics.*

where C_f is the capacitance of the shunt capacitor, ω_b is the angular velocity base value, ω is the electrical angular velocity of the AC system, V_s is the PCC voltage, i_{dq} is the battery current, and $i_{L,dq}$ is the current flowing to the PCC. $i_{L,dq}$ will be referred to as the load current, as this is the part of the battery current that is delivered to loads. Subscript d and q refers to the d- and q-axis components of the variable. Equation 5.3 (and the block diagram) provide a description of how the PCC voltage changes with time, and notably, which components contribute to this change. Important realizations are that:

1. i_d and i_q contribute to V_{sd} and V_{sq} dynamics. This suggest that the voltage can be controlled by $i_{d,ref}$ and $i_{q,ref}$.
2. The voltage dynamics also depend on the load current i_{Ld} and i_{Lq}. This is a disturbance signal, and should be counteracted.
3. The dynamics of V_{sd} and V_{sq} are cross-coupled. As long as the voltages are cross-coupled, it is impossible to change V_{sd} without also alter V_{sq}, and vice versa. This voltages should therefore be decoupled.

To account for the disturbance from the load current and the voltage cross-coupling, the control signals $i_{d,ref}$ and $i_{q,ref}$ are defined as

$$i_{d,ref} = u_d - C_f(\omega_0 V_{sq}) + i_{Ld}, \tag{5.4a}$$

$$i_{q,ref} = u_q + C_f(\omega_0 V_{sd}) + i_{Lq}, \tag{5.4b}$$

where u_d and u_q are two new control inputs. V_{sd}, V_{sq}, i_{Ld} and i_{Lq} are all measurement signals, referred to as the voltage decoupling terms and the load-compensating terms, respectively. Similar as before, the purpose of these signals are to cancel out the effect of the disturbances and the natural cross-coupling. Since V_{sd} and V_{sq} are DC quantities in steady state, two PI-regulators can produce u_d and u_q and achieve reference tracking with zero steady-state error. One PI regulator process the error $(V_{sd,ref} - V_{sd})$ and provide u_d for reference tracking of the d-axis voltage. The other PI-regulator process the error $(V_{sq,ref} - V_{sq})$ and provide u_q for reference tracking of the q-axis voltage. As the systems in the d- and q-axis control loops are identical, the two PI-regulators can also be identical. The complete voltage controller is shown in the block diagram of Figure 5.3. It can be seen that the voltage controller incorporates Equation 5.4, and that u_d and u_q are the outputs of two parallel PI-regulators. The current dynamics are described by the transfer functions of the closed-loop current controller.

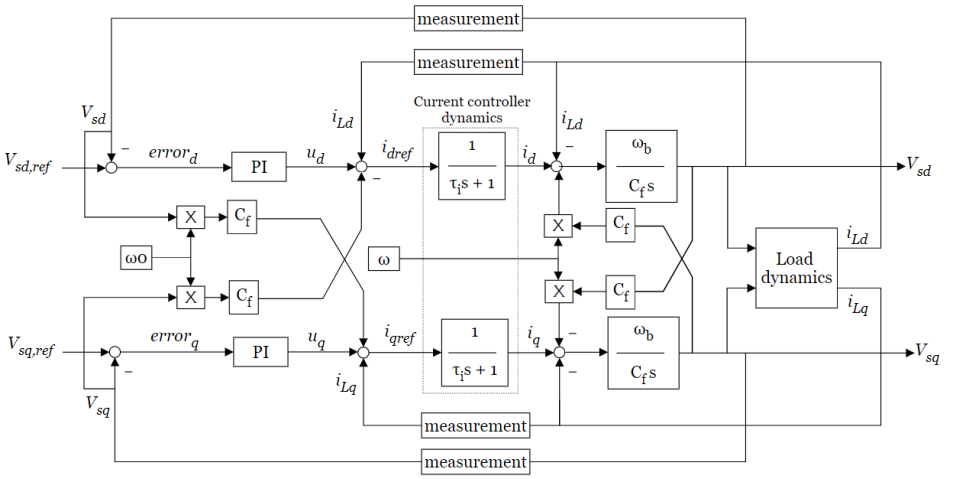

Figure 5.3: *Block diagram of the controlled voltage dynamics.*

With the assumption of nominal system frequency, and that the feed forward terms of the control system perfectly cancel the feed back of the physical system, the block diagram of the controlled voltage system can be approximated by the simplified block diagram of Figure 5.4. However, as seen from the block diagram, the control signals are applied to the left hand side of the current controller. The physical

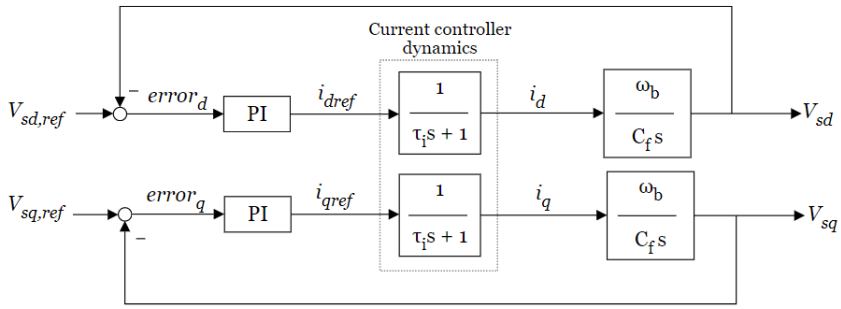

Figure 5.4: *Simplified block diagram of the controlled voltage dynamics. The validity of the model depend on the time constant τ_i.*

disturbances affect the right hand side of the current controller. This was also the case for the power controller, and the same conclusions can be drawn. If τ_i is small enough, the current controller transfer function is ≈ 1. In that case, there will be no difference in the measurement signal and the disturbance, and the voltage control loop can be described by the simplified block diagram of Figure 5.4. If τ_i is large, the current controller introduce a time lag to the measurement signals, making them differ from the disturbance terms. Thus, the validity of the simplified block diagram decreases as τ_i increases. Expectations to the voltage controller are therefore:

1. V_{sd} and V_{sq} can be controlled separately, respectively, by $V_{sd,ref}$ and $V_{sq,ref}$.
2. V_{sd} and V_{sq} will not disturb each other significantly. However, it is expected that this disturbance increase for large τ_i.
3. Even if the load current changes, it will not significantly disturb V_{sd} and V_{sq}. However, it is expected that this disturbance increase for large τ_i.

To what degree these expectations prove correct will dependent on the validity of the adopted model. This will become evident when testing the control system.

Tuning regulator gains

The two PI-regulators of the voltage controller are identical, and given by

$$k(s) = k\frac{s+z}{s}, \tag{5.5}$$

where k and z are the proportional and integral gains, respectively. The gains are

tuned to

$$\begin{aligned} z &= 0.7 \quad [\text{rad/s}], \\ k &= 1.0 \quad [\text{rad}]. \end{aligned} \tag{5.6}$$

The parameters are first tuned in accordance with the method of *symmetrical optimum*, and then somewhat adjusted based on system tests. An illustration of how the implementation of the voltage controller looks in the Simulink environment is provided in Appendix E.

5.4 Performance of the controlled battery

The behaviour of the controlled storage battery is analyzed, both connected to the distribution grid, and in stand-alone operation. When the battery is grid-connected, the P/Q controller is the active part. During stand-alone, it is the V/f controller that is the active part. The PV-array is not connected at this point. The Thévenin impedance of the distribution grid is sat to zero, that is, the distribution grid is modelled as a stiff grid.

5.4.1 The storage battery in grid-connected operation

In this scenario, the switch connecting the microgrid with the utility is in closed position. That is, the voltage at the PCC is supported by the (stiff) grid, and the behaviour of the storage battery is dictated by the power controller. The control objective is to deliver the requested amount of power. The storage battery's ability to do this is tested by making steps-changes to $P_{s,ref}$ and $Q_{s,ref}$. The reference powers are initially zero, and subjected to the following changes at the time instants

$t = 0.20$ sec: $P_{s,ref}$ is step-changed from 0 p.u. to 1 p.u.

$t = 0.30$ sec: $P_{s,ref}$ is step-changed from 1 p.u. to -0.2 p.u.

$t = 0.35$ sec: $P_{s,ref}$ is step-changed from -0.2 p.u. to 0.5 p.u.

$t = 0.40$ sec: $Q_{s,ref}$ is step-changed from 0 p.u. to 1 p.u.

The system time response during no-load condition is depicted in Figure 5.5. The measured values are the battery powers, P_s and Q_s, the line currents, i_d and i_q, and the PCC voltages V_{sd} and V_{sq}. It should be remembered that as long as $V_{sq} = 0$, the amplitude of the PCC voltage is given by the d-axis component of the voltage. That is, $\hat{V}_s = V_{sd}$. It can be observed that:

1. P_s and Q_s can be controlled separately, respectively by $P_{s,ref}$ and $Q_{s,ref}$. This imply that the current cross-coupling is successfully decoupled.

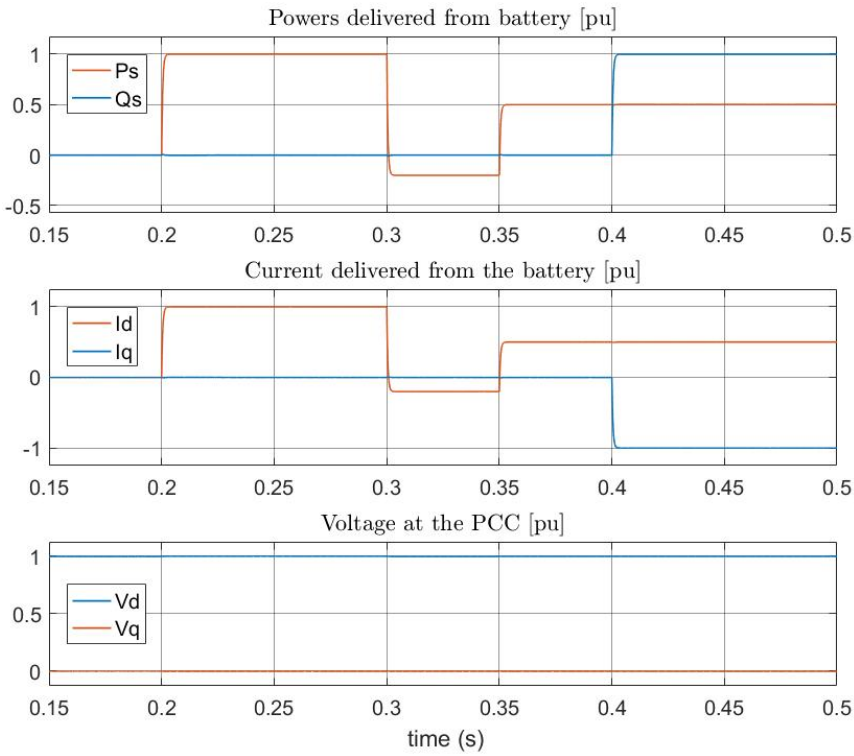

Figure 5.5: *Storage battery time response to step-changes in $P_{s,ref}$ and $Q_{s,ref}$. No-load condition and connected to a stiff grid.*

2. As expected, P_s follow the same transient pathway as i_d. Q_s follow the same pathway as i_q. They stabilize in the same per-unit value, and have the dynamic response of a first order transfer function. Close examination verify that τ_i still equals 0.5 ms (see also Figure 4.5).

3. $V_{s,abc}$ is not disturbed by the changes in P_s or Q_s. This is expected, as the voltage here is imposed by the stiff distribution grid.

Similar time responses during the partially and the fully loaded conditions are shown in Figure 5.6 and Figure 5.7. As seen from the figures, the time response of the system is equal in all three situations. Thus, the power controller reference tracking ability is unaffected by the load condition.

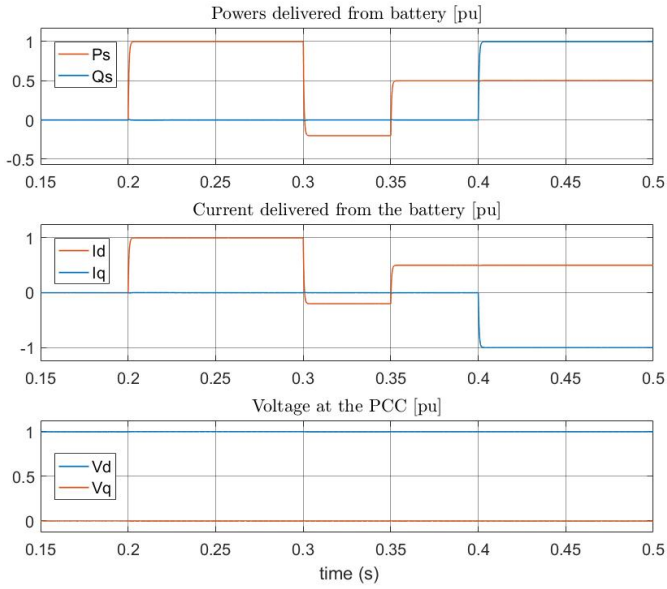

Figure 5.6: *Storage battery time response to step-changes in $P_{s,ref}$ and $Q_{s,ref}$. Partially loaded condition and connected to a stiff grid.*

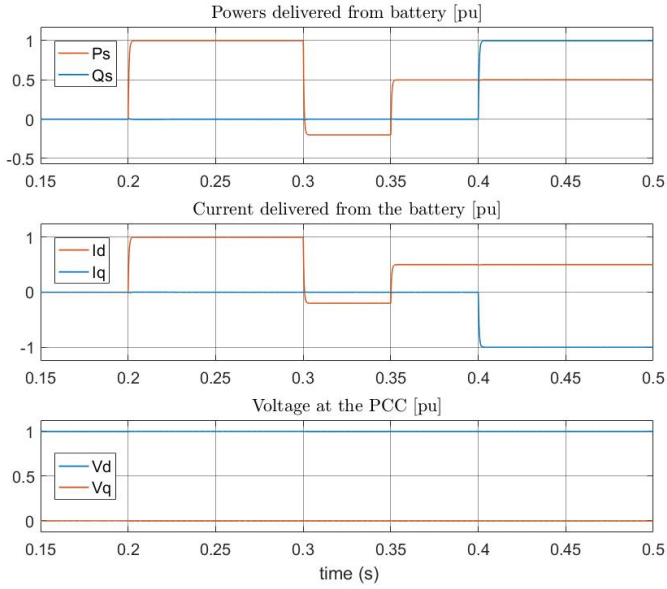

Figure 5.7: *Storage battery time response to step-changes in $P_{s,ref}$ and $Q_{s,ref}$. Full-load condition and connected to a stiff grid.*

5.4.2 Islanding the storage battery

In this scenario, the switch connecting the storage battery to the distribution grid will be opened. The scenario illustrates the storage battery's ability to work in stand-alone operation. The control objective during this operation is to regulate the amplitude and frequency of the load voltage (PCC voltage), $\hat{V}_s$, in the presence of disturbances in the load current, $i_{L,dq}$ (*i.e.* changes in load condition). In order to keep the PCC voltage to its nominal value, the battery must adapt to the load condition, so it at all times delivers the requested amount of power. The battery's ability to do this is tested by step-vise connect and disconnect load 1 and 2 from the microgrid. As the storage battery is equipped with a voltage controller, it is expected to be able to do this (at least until the depletion of the battery). The scenario unfolds as follows: Initially, the storage battery is connected to the grid. Both loads are disconnected, and the battery is being charged by a current $i_d = 1$ pu (that is $P_{ref} = -1$, and $Q_{ref} = 0$). Thus, there is an import of active power from the distribution grid. There is also an export of reactive power, due to the shunt capacitor, C_f, producing reactive power. At the time instants:

$t = 0.20$ sec: The switch at the PCC is opened, islanding the storage battery. At the same instant, the battery is switched from power control to voltage control.

$t = 0.30$ sec: Load 1 is connected to the PCC.

$t = 0.40$ sec: Load 2 is connected to the PCC.

$t = 0.50$ sec: Load 2 is disconnected from the PCC.

$t = 0.60$ sec: Load 1 is disconnected from the PCC.

The system time response is depicted in Figure 5.8. The plotted values are the PCC voltages, V_{sd} and V_{sq}, the current delivered from the battery, i_d and i_q, and the load currents, i_{Ld} and i_{Lq}. The PCC voltage amplitude, $\hat{V}_s$ is not plotted. As $V_{sq} \approx 0$ the entire time, $\hat{V}_s$ is almost not distinguishable from V_{sd}. One can observe that:

1. As expected, the voltages are regulated to their reference values, $(V_{sd,ref}, V_{sq,ref}) = (1, 0)$, with zero steady-state error. There are only small transient fluctuations away from the reference values at the times when the system is disturbed.

2. The current delivery from the battery, i_d and i_q, are adapted to the new operating conditions in order to keep the voltage across loads to nominal value.

3. When the microgrid is disconnected, i_d is regulated to ≈ 0, and i_q is regulated positive. This is expected, as there is no real power consumption in the microgrid at that time (except some losses in the feeder line), but the shunt capacitor requests a negative reactive power.

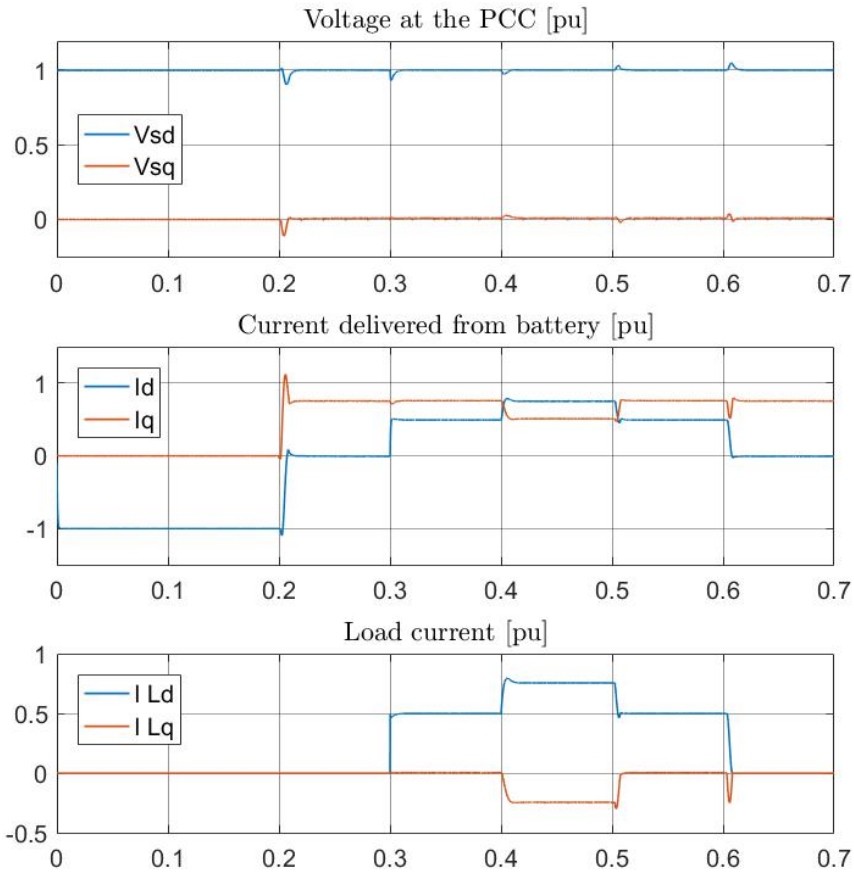

Figure 5.8: *The voltage controller is regulating V_{sd} to 1 p.u., and V_{sq} to zero while being disturbed by step-changes in the load condition.*

4. The connection of load 1 only affect the d-axis component of the currents, i_d and i_{Ld}. This is due to the d-axis current component being associated with real power, and load 1 being purely ohmic.

5. The connection of load 2 affect both the d- and the q-axis component of the currents. This is due to q-axis current component being associated with reactive power, and load 2 is both ohmic and inductive.

It can be concluded that the storage battery in stand-alone operation has the ability to regulate the PCC voltage to nominal value with zero steady-state error. Further, it is able to support this voltage under a dynamic load condition.

5.5 Performance of the complete microgrid

Operation of the complete microgrid is analyzed. That is, both the PV-array and the storage battery are connected to the PCC. The Thevenin impedance of the distribution grid is zero, that is, the distribution grid is still modelled as a stiff grid. In this scenario, the microgrid is initially grid-connected, but is islanded at the time $t = 0.45$ seconds. The control objective of the microgrid is to continue to perform MPPT, optimizing the efficiency of the PV-array, while at the same time regulate the voltage over loads (PCC voltage) to nominal value. The microgrid's ability to preform these tasks are tested by changing the solar irradiance after the microgrid has been islanded. Initial conditions are: Solar irradiation equal $100W/m^2$. $(P_{s,ref}, Q_{s,ref)} = (0.5, 0)$. Both loads are connected, representing the full-load condition. There is a small import of real power from the distribution grid, and a larger export of reactive power to the distribution grid. At the time instants:

$t = 0.45$ sec: The switch at the PCC is opened, islanding the microgrid.

$t = 0.80$ sec: Solar irradiation is step-changed up to $1000W/m^2$.

$t = 1.10$ sec: Solar irradiation is step-changed down to $200W/m^2$.

$t = 1.40$ sec: Solar irradiation is step-changed up to $600W/m^2$.

The time response of the system is depicted in Figure 5.9. The plotted values are the power extracted from the PV-array, P_{ext}, the power sent to the AC-system from the PV-array, P_t, the power deliveries from the storage battery, P_s and Q_s, and the PCC voltage, V_s. The voltage at the PCC is shown both in terms of the d- and q-axis components, as well as the amplitude, $\hat{V}_s$. However, as V_{sq} hardly deviates from zero, V_{sd} and $\hat{V}_s$ overlaps. It is observed that:

1. As expected, the power delivery from the PV-array is unchanged by the event of islanding. This is because the array is continuing to perform MPPT and the solar irradiation has not been changed.

2. As expected, the storage battery adapts its power delivery to the new operating condition. This happens immediately after islanding, to account for the loss of the distribution grid. Thus, there is a small increase in P_s, and a larger decrease in Q_s. As a result, the PCC voltage is kept to nominal during the event.

3. When the real power delivery from the PV-array increases, the PCC voltage starts to increase. The storage battery reacts by reducing P_s. As a result, the PCC voltage is regulated back nominal.

4. Similarly, when real power delivery from the PV-array drop, the PCC voltage starts to drop. The storage battery reacts by increasing P_s. As a result, the PCC voltage is regulated back to nominal.

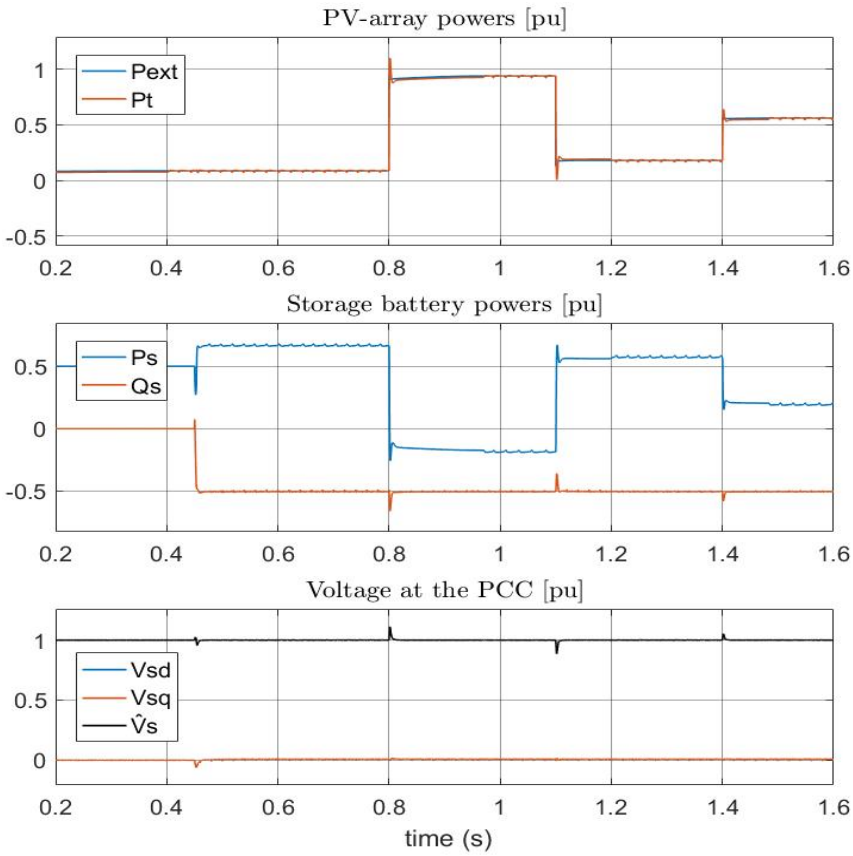

Figure 5.9: *Time response of the complete microgrid. The microgrid is isolated at the time $t = 0.45$ seconds. The isolated microgrid is operating at full load condition and a variable supply from the PV-array.*

5. As expected, the PCC voltages are regulated to their reference values with zero steady-state error. This implies that the requested power is being delivered to loads during the entire event, both during the islanding of the microgrid, and during the variable solar conditions.

When including a storage battery to the microgrid, the PV-array conduct MPPT while power quality at the same time is maintained. This is achieved by having the battery perform voltage control. This means that the battery adapts to the power delivery coming from the PV-array, charging during power surplus and discharging during power deficit. Having this buffer, the voltage at the PCC is regulated to nominal value, and requested power is being delivered to loads, also during variable solar conditions. It can be concluded that, with the control system developed, the respective control objectives are achieved. The PV-array efficiency is optimized, and power is delivered to loads at a nominal voltage level, both dur-

ing grid-connected and isolated operation. The next chapter is a documentation of further analyzes of the complete microgrid system behaviour.

Chapter 6

Applications

A simulation model that accurately represent a physical system will have a large application potential. Some possible simulations tests will be shown in this chapter. Simulations concern important events such as islanding of the microgrid. They also concern islanding with delays in the mode command signal. It is further explored how the size of the current controller time constant, τ_i, affect the battery's voltage reference tracking ability.

6.1 Transient response to islanding

This section is dedicated to illustrate how voltage transients propagate in the microgrid when it is islanded from the utility, and an analysis of which circumstances will impose the larger transients. The voltage transients are plotted in terms of the amplitude of the PCC voltage, $\hat{V}_s$. Generally, all changes to an electrical system *e.g.* customers that change loads, changes in solar intensity, a generator outage, short circuits, lightning strikes, *etc*, will introduce transients, by pushing the system away from its current operating point. The change imposed from islanding can be compared to the loss of a source, or the disconnection of a load, depending on whether the microgrid is importing or exporting energy. In the following analysis, a scenario where the microgrid has a significant production surplus is simulated. As a representation of an extreme situation, solar irradiance is sat equal to $1000W/m^2$, and no load is connected to the microgrid. Thus, the microgrid will export a large amount of power, unless the storage battery is charged. Three different cases are, respectively,

case 1: $(P_{s,ref}, Q_{s,ref})$ = (-0.9, -0.8), strong distribution grid,

case 2: $(P_{s,ref}, Q_{s,ref})$ = (+0.9, +0.8), strong distribution grid,

case 3: $(P_{s,ref}, Q_{s,ref})$ = (+0.9, +0.8), less strong distribution grid.

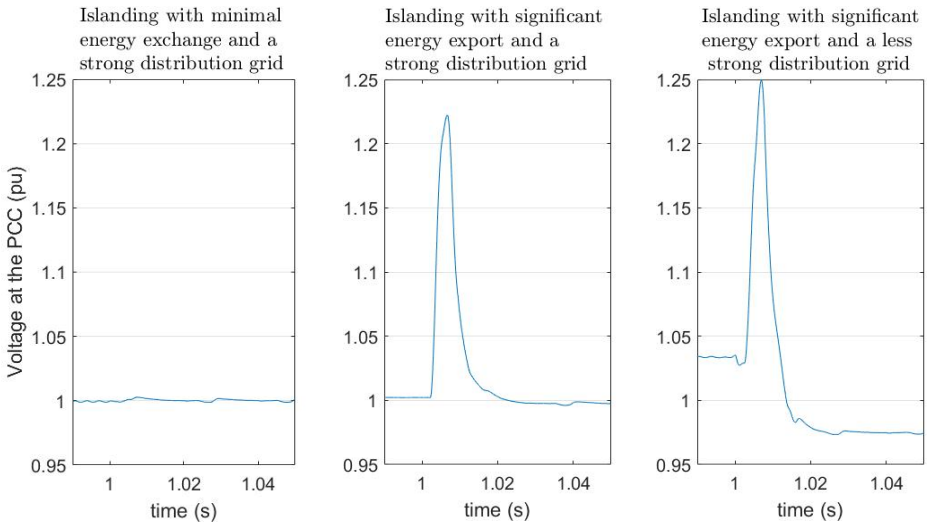

Figure 6.1: *Microgrid islanding under the three different scenarios.*

Whit these initial power references, the microgrid is islanded at time $t = 1$ seconds. In all three cases, the transient response in the PCC nodal voltage, $\hat{V}_s$, is shown in Figure 6.1. Keep in mind that the power reference signals dictate how much energy is exchanged with the distribution at the instant islanding occur. At the instant of islanding, the storage battery is switched to voltage control, in which case ($V_{sd,ref}$,$V_{sq,ref}$) = (1, 0). In Case 1, pre-islanding power exchange with the utility is minimized by charging the storage battery. In Case 2, the energy flow to the battery is reversed, thus the power export to the utility is significant. Case 3 has similar power export as Case 2, additionally, the impedance of the distribution grid, $Z_{th} \neq 0$. It can be observed that:

1. In the case of minimal power exchange, there is hardly any disturbance to $\hat{V}_s$.
2. In the case of significant energy export, a transient disturbance is imposed on $\hat{V}_s$. The disturbance is short in duration, but high in magnitude.
3. In the case of significant energy export and a less strong grid, the peak value of $\hat{V}_s$ reaches an even greater magnitude. This is due to $\hat{V}_s$ before islanding being slightly higher than nominal ($\approx 0.3pu$), and this offset adds to the voltage rise caused by the islanding. The voltage offset originates from the voltage across the distribution grid impedance, imposed by the energy export from the microgrid. In addition to the increased voltage peak, the voltage also dips below nominal after islanding. It takes the control system approximately 3 seconds to correct the voltage back to nominal (not shown in the figure).

It can be concluded that the transient response to islanding is affected both by the energy exchange with the distribution grid, and the distribution grid impedance. Voltage transients are avoided if there is no energy exchange at the instant islanding occur. If the energy exchange is significant, a voltage transient of high magnitude might be imposed at the PCC. The transient peak may be magnified if the microgrid is connected to a weak distribution grid.

Further investigation of the islanding transient response is conducted by assigning a range of different power references to the storage battery. In this test, $Q_{s,ref}$ is equal to zero for all cases, and only $P_{s,ref}$ is varied. $\hat{V}_s$ in the milliseconds around islanding is depicted in Figure 6.2.

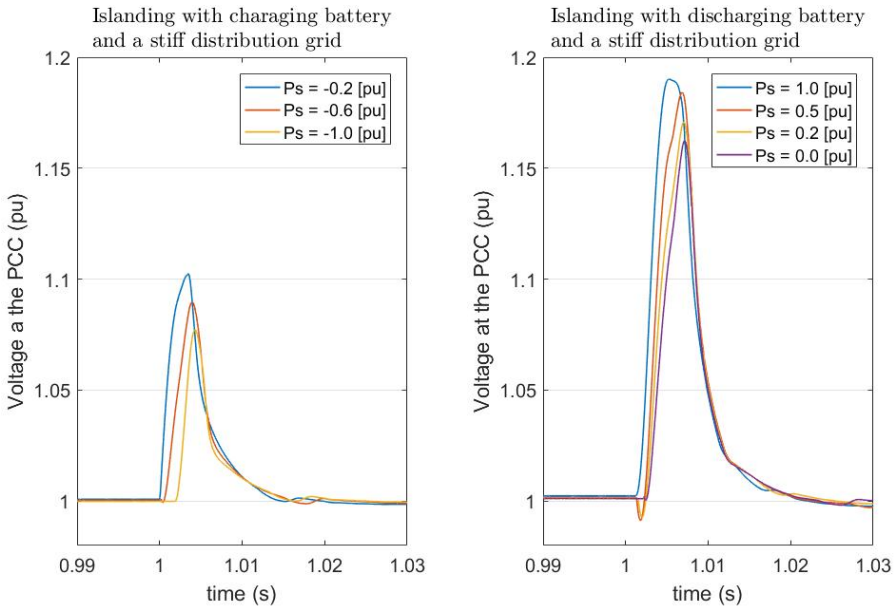

Figure 6.2: *Microgrid islanding at $t = 1$. $Q_s = 0$ and different values for P_s. Peak in $\hat{V}_s$ is highly dependent on the direction of the power flow.*

In the figure, the left frame depicts the results from a charging storage battery (negative P_s), while the results from a discharging storage battery (positive P_s) are shown in the right frame. Observations from this simulations are:

1. Generally, charging the storage battery result in a lower voltage peak than discharging the storage battery. This is expected, as a charging storage battery means less power exchange with the utility.
2. A greater charging current introduce a small delay in the rise of $\hat{V}_s$. It also limits the peak voltage, and shortens the correction time.
3. Conversely, a smaller discharging current introduce a small time delay to the voltage rise. It also limits the peak voltage, and shortens the correction time.

4. The voltage peak seems to be more dependent upon the direction of the storage battery power flow than the magnitude of this power flow. *e.g.* it can be seen that the response in $\hat{V}_s$ do not differ much from $P_s = 1.0$ and $P_s = 0.0$. However, the response differ significantly from $P_s = 0.0$ and $P_s = -0.2$.

Again, it is seen that a higher power exchange with the utility when islanding introduce a greater voltage transient. However, it seems that the most severe voltage fluctuations are avoided as long as the power flow in the storage battery feeder do not have to change direction.

6.2 Microgrid islanding with delay or failure in the mode command signal

This section is dedicated to illustrate what may be the consequences of delays or failures in the mode command signal. The mode command is the signal which coordinates the islanding of the microgrid with proper switching between power control and voltage control of the storage battery unit. Two situations are analyzed. These are, respectively, when the switch to voltage control lags the islanding of the microgrid, and when the switch to voltage control precedes the islanding of the microgrid.

6.2.1 Islanding with delayed activation of voltage controller

Here, the storage battery is switched to voltage control 50 milliseconds after the microgrid has been islanded. This situation might occur if *e.g.* the microgrid is unintentionally islanded, as the islanded situation must be detected before proper control action can take place. Depending on the detection scheme, islanding detection introduce a short or a long time delay. Fast island detection might be as quick as 4 ms, while slower methods might take 100 ms or longer [32]. In this scenario, solar irradiation is sat equal to $300W/m^2$, and both loads are connected to the microgrid. With this irradiance, the power output from the PV-array is insufficient to cover the loads. The storage battery power references prior to islanding are $(P_{s,ref}, Q_{s,ref}) = (0,\ 0)$. The power delivery from the battery feeder and the PV-array feeder, and the resulting transient response in PCC voltage are shown in Figure 6.3. The PCC voltage is shown both in terms of voltage amplitude, $\hat{V}_s$, and in terms of the three-phase signals, $V_{s,abc}$. It is seen that

1. islanding occur at time $t = 1.00$ second, but the battery do not increase its power output before it is switched to voltage control, at time 1.05 seconds.
2. the power deficit during the time interval between 1.0 and 1.05 causes $\hat{V}_s$ to drop.
3. the system quickly recover $\hat{V}_s$ to nominal value once the voltage controller is activated.

As can be seen, the event does not have any sustained detrimental impact on the power quality apart from the 50 ms period until the battery switches to voltage control. However, if islanding were never detected, the battery would not shift to voltage control at all. Then, one would have the same situation as if the PV-array was operating in stand alone. The power quality in that situation is not satisfactory, as the PV unit do not regulate its power output according to the load, but according to MPPT.

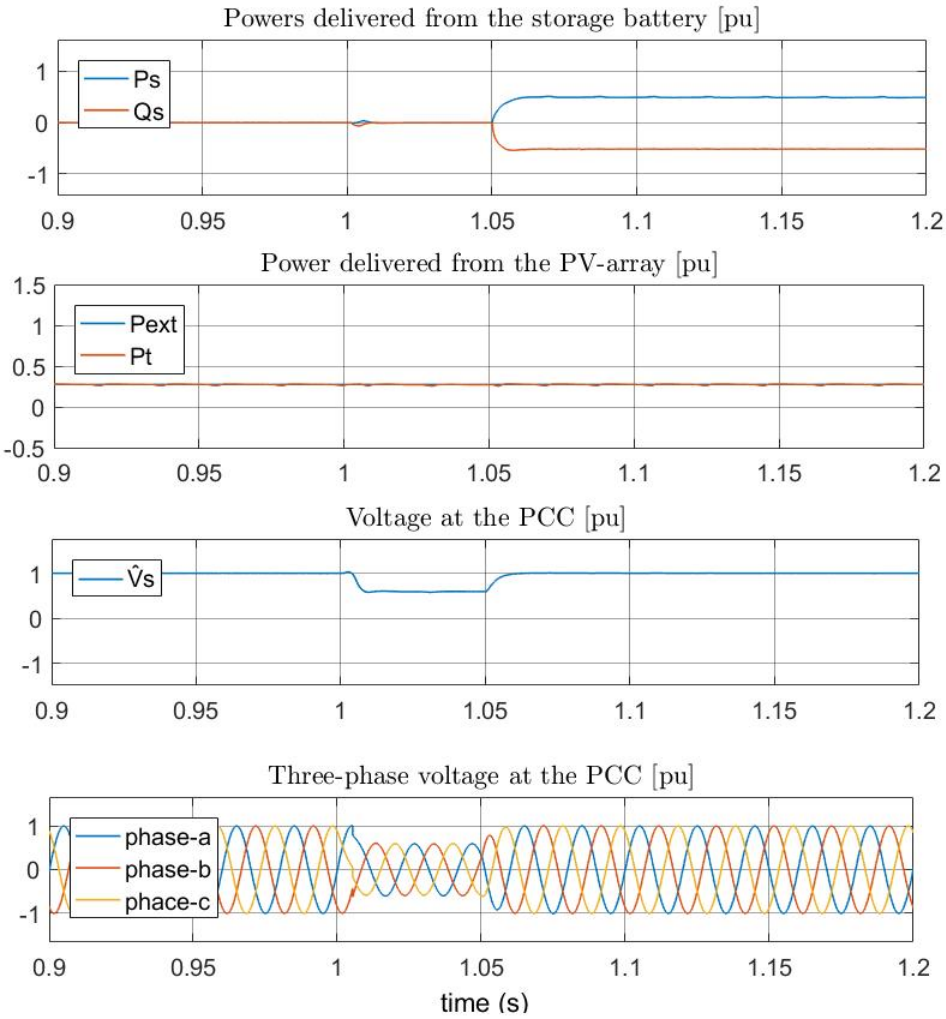

Figure 6.3: *The microgrid is islanded 50 ms before the battery switch to voltage control. Full load, solar irradiance*= $300W/m^2$, $(P_{s,ref}, Q_{s,ref})$ = (0,0).

A more severe situation occur in the situation of a power surplus after islanding. Solar irradiance is still $300W/m^2$, but the storage battery supplies power with the references $(P_{s,ref}, Q_{s,ref}) = (0.8,\ 0.8)$. Again, the microgrid is islanded at the time $t = 1$ second. The voltage controller is activated 50 ms later, at the time $t = 1.05$ seconds. The power delivery from the battery and the PV-array feeder, and the resulting transient response in PCC voltage are shown in Figure 6.4. The PCC voltage is shown both in terms of voltage amplitude, $\hat{V}_s$, and in terms of the three-phase signals, $V_{s,abc}$. It can be seen that

1. Due to excess of energy, $\hat{V}_s$ increases when the microgrid islands.
2. The storage battery continue to try to regulate P_s and Q_s to their reference values, but is unable to do so. They deviate in separate directions, creating a standing (and even increasing) oscillation.
3. the oscillations spread to the rest of the system, causing both the PCC voltage and the power flow in the PV-array feeder to oscillate.
4. the high magnitudes of $\hat{V}_s$ cause reverse power flows in the PV-array feeder. This is unwanted behaviour, and may cause damage to the PV-array. Protection systems should be in place to prevent negative power flows.
5. At time $t = 1.05$ seconds, the battery voltage controller is activated. The system recover to steady-state with nominal $\hat{V}_s$. However, in the 50 ms time period before the voltage controller was activated, the system was unstable.

This situation had a much more severe impact on the microgrid power quality. The voltage quality is low during the transient period, and may cause damage to equipment.The system is also unstable until the voltage controller is activated. This illustrate how the mode command signal may be a single point to failure. If the battery voltage controller fails to activate, the system may become unstable, and other protective actions (perhaps a shutdown) must take place. Improvements may be done on the control system to increase stability margins, and make the system more robust to such events. Thus, there might be necessary to develop more sophisticated controllers.

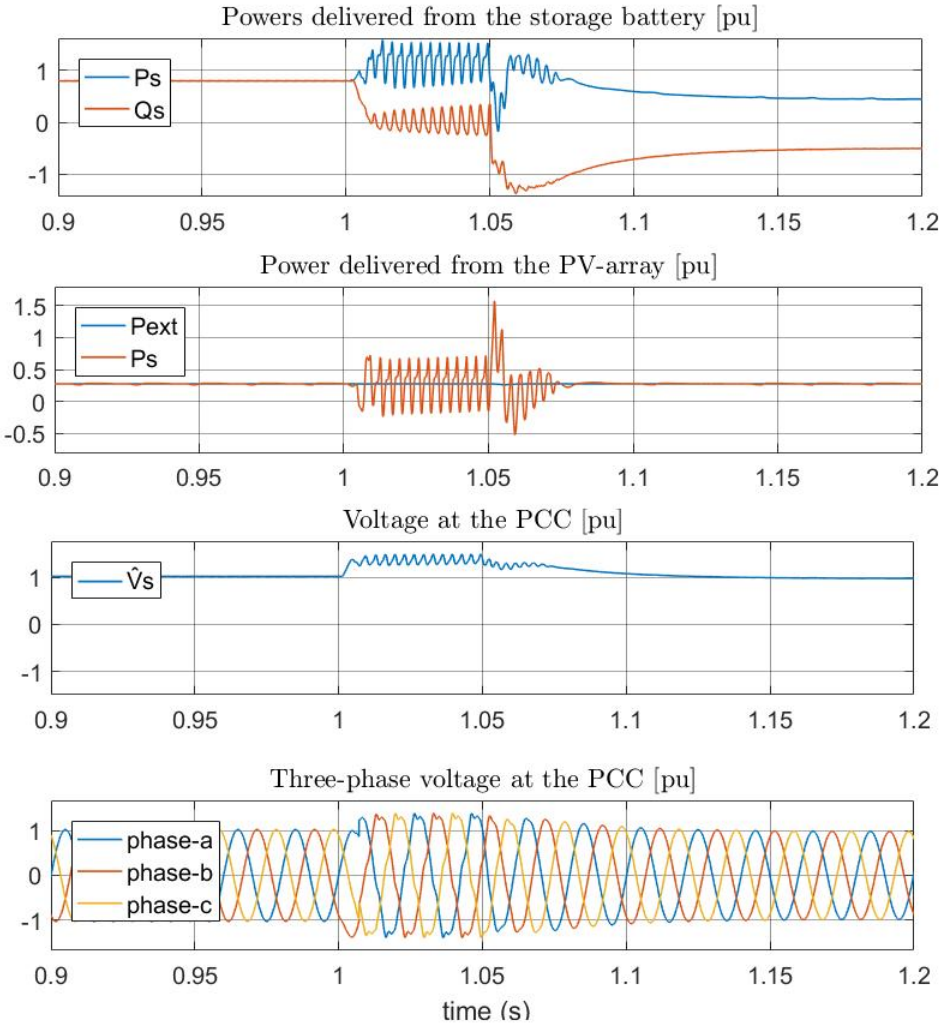

Figure 6.4: *The microgrid is islanded before the battery controller switch to V/f control. (Full load, solar irradiance= $300W/m^2$).*

6.2.2 Activation of voltage controller with delayed islanding

Here, the storage battery is switched to voltage control approximately one second before the microgrid is islanded. The simulation represent an unintentional switch to voltage control. In this scenario, solar irradiation is sat equal to $300W/m^2$, and both loads are connected to the microgrid. The storage battery power references prior to islanding equal $(P_{s,ref}, Q_{s,ref}) = (0,0)$. Thus, there is an import of real power, and an export of reactive power prior to islanding. The impedance of the distribution grid, $Z_{th} \neq 0$, and there is a small discrepancy from nominal voltage at the PCC prior to islanding. At the time $t = 0.95$ seconds, the battery is switched to voltage control, but the switch at the PCC remains closed until the time $t = 2.0$ seconds. The resulting power delivery from the battery feeder and the PV-array feeder, and the resulting nodal voltage amplitude at the PCC are shown in Figure 6.5. It can be observed that

1. Even the small discrepancy from nominal voltage produce large response in P_s and Q_s. This is because while grid-connected, the Thevenin impedance seen from the battery is small (due to the parallel branch of the distribution grid). As soon as the microgrid islands, the Thevenin impedance is higher, thus, P_s and Q_s drops in magnitude.
2. P_s and Q_s are limited at approximately $\pm$1p.u. This is due to reference current saturation block inside the battery controller.
3. The power flowing in the PV-array feeder is not disturbed. This is because the voltage at the PCC do not differ significantly from nominal value.
4. The system remains stable, also during the time period between $1 < t < 2$ seconds. In the case where the PCC switch do not open at all, P_s and Q_s stabilizes with the values $P_s \approx 0.88$ p.u. and $Q_s \approx -0.62$ p.u.

It seems that a switch to voltage control without islanding does not cause large problems concerning the stability of the microgrid. However, the powers are no longer regulated, and may deviate largely from their desired values if the battery is unintentionally switched to voltage control.

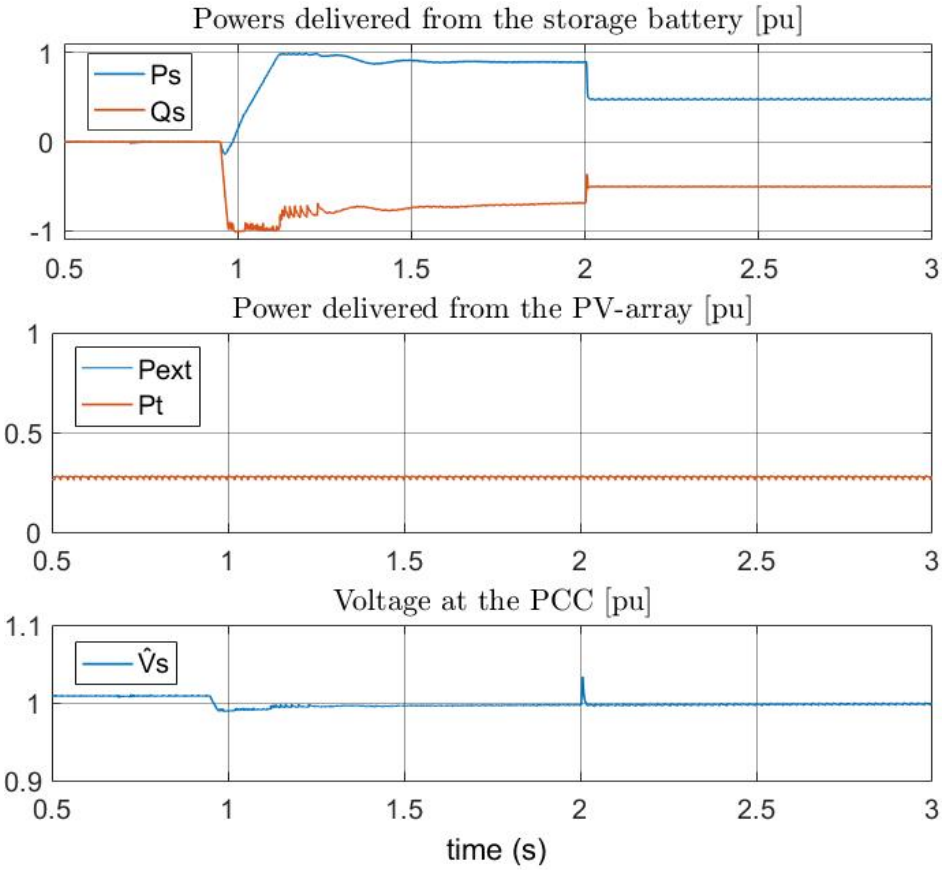

Figure 6.5: *The battery controller switch to V/f while the microgrid is still connected to the distribution system. Full load, solar irradiance=* $300W/m^2$*).*

6.3 Sensitivity to load condition

This section is dedicated to an analysis of the battery voltage controller sensitivity to the load condition. The battery voltage controller regulate the nodal voltage at the PCC. The dynamics of this voltage, in terms of V_{sd} and V_{sq}, is described by Equation 5.3. As previously stated, the load currents, i_{Ld} and i_{Ld}, are included in Equation 5.3 as disturbance terms. To counteract this disturbance, load-compensating feed-forward terms are included in the voltage control system. These can be seen from the block diagram of Figure 5.3, for simplicity repeated here as Figure 6.6.

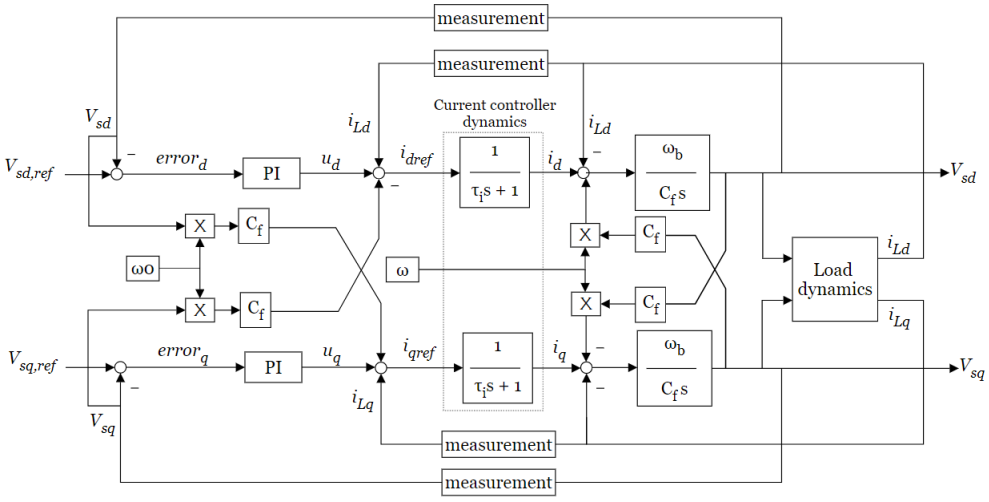

Figure 6.6: *Block diagram of voltage controller repeated.* $i_{d,ref}$ *and* $i_{q,ref}$ *as defined in Equation 5.4.*

As stated in the development of the voltage controller in the previous chapter (also seen from Figure 6.6), the effectiveness of the load-compensating feed-forward terms will depend on the time constant of the current controller. If τ_i is zero, the dynamics of the current controller will equal to 1, and the load-compensating feed-forward terms will perfectly cancel the load disturbance. However, the current controller inevitably introduce some time lag, and so, τ_i will never be zero. It is therefore expected that voltage controller performance is not fully invariant to the load condition. Further, it is expected that the load condition dependency increase as the time constant of the current controller increases. In the microgrid model of this thesis, (as switching harmonics from the VSC are not modelled), there are no apparent consequences from choosing a current controller time constant τ_i close to zero. In reality however, τ_i must be adequately large such that the harmonics from the VSC do not interfere with the current control. Normally, τ_i is selected in the range of $0.5 - 5$. The step-response of the voltage controller have

been compared for the lower and upper limit, *i.e.* $\tau_i = 0.5$ ms, and $\tau_i = 5.0$ ms, respectively, representing a fast and a slow current controller. In the simulation, $V_{sq,ref}$ was kept to zero, and $V_{sd,ref}$ was subjected to the following step-changes at times:

$t = 0.15$ sec: $V_{sd,ref}$ is step-changed from 0 p.u. to 1 p.u.

$t = 0.30$ sec: $V_{sd,ref}$ is step-changed from 1 p.u. to 1.2 p.u.

$t = 0.40$ sec: $V_{sd,ref}$ is step-changed from 1.2 p.u. to 0.5 p.u.

The resulting response in V_{sd} and V_{sq} are shown in Figure 6.7 and Figure 6.8. The results verify that, when current control is fast, the reference tracking ability of the voltage controller is almost invariant of load condition. When current controller is slow, the reference tracking ability of the voltage controller is different during no-load and full-load conditions. As expected, it can be concluded that as τ_i increases, the reference tracking ability of the voltage controller becomes more sensitive to the load condition.

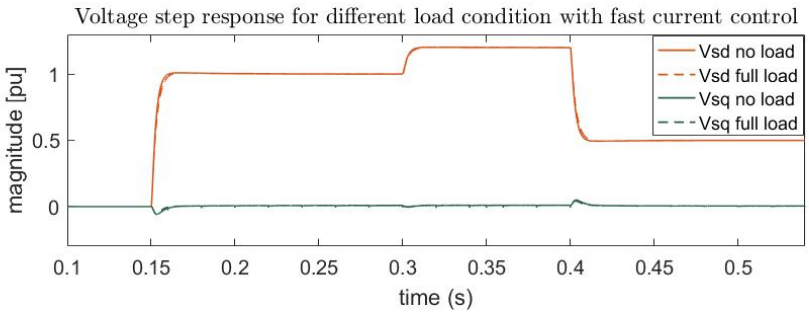

Figure 6.7: *Voltage controller step-response with fast current control.*

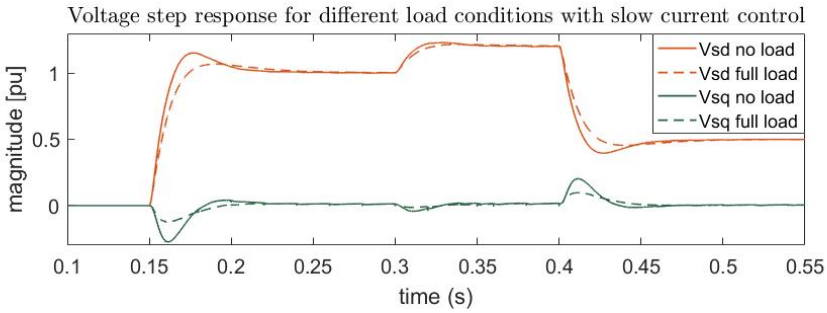

Figure 6.8: *Voltage controller step-response with slow current control.*

Chapter 7

Discussion

A main goal of this work was to develop an initial framework for the study of microgrid control. The framework consists of a microgrid model implemented in the MATLAB/Simulink simulation tool. The model incorporates a suggested control structure, supplied with a treatment of the underlying concepts. The model was restricted to contain as few elements as possible, only the absolute necessary components were included. These were a generating unit (PV-array), a storage unit (battery), a distribution system and loads, as well as the power electronic interfaces between the AC- and the DC-components. The model needs further expansion in order to represent more complicated microgrids, who might include generation from multiple sources, and perhaps structured with multiple busbars. However, even with the modest amount of components, the small microgrid model incorporates a range of fundamental control functions. These functions can be considered building blocks on which a more complicated microgrid model can be developed. As has been shown, the current controller constitutes the innermost control loop, present in all controlled elements. Upon the current controller, either power control or voltage control can be build. Maximum power point tracing of the PV-array was further achieved by making additions to the power controller. An expansion of the microgrid model can to a large degree be achieved by use of the same fundamental building blocks. Optimization of other generating units, *e.g.* maximum power point tracing of a wind turbine, can be achieved by use of much the same systems (*i.e.* a current controller, a power controller and a DC-side voltage controller [37]).

Simplifications were made when modeling the microgrid power system dynamics. The element of the power system were in-built models from the Simulink library, most of them fairly complicated. The largest simplifications may have been the ones concerning the VSC model. The converter was modelled by a technique that averages the voltage profile over one switching cycle. By utilizing this method, information of switching harmonics were lost. The choice was justified by the benefits from fast simulations. Most simulations concerned events that lasted less

than 3 seconds, and it took approximately 5-10 seconds to perform the simulations. This simulation run-time was acceptable.

In the design of the control system, simplifications were also made regarding the microgrid power system dynamics. It is worth noting, however, that these simplifications did not influence the models of the power system elements. Important simplifications in the control system design concerned the time constants of the control loops. Whenever new (outer) control loops were added to the control system, the inner control loops were assumed to have time constants of zero. In the design of the DC-side voltage controller of the PV-array, the feeder line impedance was disregarded. The importance of these simplifications were explored. It was hypothesized, based on relevant equations and block diagrams, that larger time constants in the inner control loops would lead to the outer control loops being more influenced by disturbance signals. Simulations were therefore conducted with both a fast and a slow inner current control loop. It was confirmed that, as the current controller time constant increased, the outer voltage control loop became more sensitive to load conditions. This highlights the value of having fast inner controllers, especially in cascaded systems of multiple control loops. The impact of disregarding the feeder line impedance in the DC-side voltage controller was also examined. By studying a more accurate model of the DC-side voltage dynamics, it was noted that stability boarders were not threatened by positive power flows. Negative power flows, on the other hand, lead to excessive phase lag in the loop gain, and may therefore threaten stability. Negative power flows are when the converter operate as a rectifier. This was forced upon the PV-array when the microgrid was islanded without the proper coordination of the microgrid master controller, due to failure in the mode command signal. However, preventing negative power flows may be fairly manageable, perhaps by means of diodes on the DC-side of the converter. Applied to another system, a DC-side voltage controller may be intended to operate for power flows in both directions. This can be enabled by adding a lead filter to the controller loop gain that compensates the excessive phase lag, as proposed in Reference [23].

The control system developed could probably be made more complex. However, the feasibility of a control system is not necessarily measured by its complexity. The more complex, the higher becomes the computational burden (and the price), which may be a demerit of the system. The feasibility of a control system should be measured by its ability to perform reference tracking under the range of operating conditions and possible disturbances. Also, for its robustness, its ability to maintain stability in the event of component failure or other unforeseen and critical situations. Thus, simplifications may be justified as long as they do not compromise these abilities. The value of good simulation tools become evident. This allows to start with a fairly simple control design, as the one developed, and make improvements where necessary based on results from simulation tests. In the control system developed, a disadvantage might be having a single unit (the battery) responsible for voltage control during isolated operation. This issue is worsened by the need for two distinct controllers on this unit, with following de-

pendence on proper coordination of controller modes. This means that the system has critical components that may be a single point of failure. Advantages with the method was that it enabled zero steady-state error.

In further development of the model, it would be interesting to integrate other sources into the microgrid. The units included so far were all no-inertia units. High inertia systems has slower dynamics than low inertia systems. It is therefore reason to believe that including inertia into the system would be beneficial from a stability perspective. However, it would be interesting to study the combined dynamics of inertia elements (perhaps connected directly to the microgrid) and no-inertia elements (connected via converters). Even if inertia in general may be a positive attribute, combining multiple units who largely differ in their dynamic behaviour may prove to be a source of other challenges. Another interesting development of the microgrid model is to include a strategy to recombine the microgrid with the distribution grid after islanding. This was originally intended, but was excluded due to time limitations. Recombination requires a supervisory control system that coordinate the time instant of the closure of the PCC switch. When the microgrid is in island mode, a phase lag is likely to exist between the microgrid and the distribution grid. This means that even if the voltages in both systems are at nominal levels (in terms of rms values), they may have large (instantaneous) voltage differences. Thus, a synchronization mechanism must be in place for the recombination of the microgrid. A synchronization mechanism is proposed in Reference [23], but its details have not yet been studied. Further, it may be interesting to see how the adaption of a more accurate model of the VSC affect the system, both in terms of simulation run-time, and severity of disturbances from switching harmonics. These switching harmonics sets limitations on the current controller, and it may be of interest to explore how fast current control could be allowed before the VSC switching harmonics disturb the control significantly. Finally, if a well developed microgrid control system has been achieved, the next step would be to implement the system into a laboratory environment for physical testing. The Smart Grid Laboratory at NTNU may be one facility where the microgrid model can be tested.

Chapter 8

Conclusions

A control system for a microgrid model has been developed. The model consisted of a generating unit (PV-array), a storage unit (battery), a distribution system and loads, as well as the power electronic interfaces between the AC- and the DC-components. The control was performed through inverter control of the microgrid units in a master-slave structure. The control functions implemented were current control, power control, voltage control, and maximum power point tracing of the PV-array. The control system was shown to enable optimized efficiency of the PV-array, while at the same time regulate the amplitude and frequency of the load voltage in the presence of a variable load condition and a variable supply. The control system was feasible during both grid-connected and islanded operation, and was able to adapt to islanding events with the microgrid stability preserved.

An advantage of the master-slave structure utilized is that it enabled reference tracking with zero steady-state error. A disadvantage with the strategy is the need for two distinct controllers on the master unit (the battery), with following dependence on proper coordination of battery controller modes. Delays of failure in the mode command signal could lead to system instability. The most severe disturbances occurred when the microgrid was islanded before the battery made the proper switch from power control to voltage control.

The application potential of the developed simulation model was demonstrated. Simulations concerned transient dynamics during important events. These were islanding of the microgrid during power exchange with the utility, and islanding that did not coordinate with the microgrid master controller. It was also demonstrated how the current controller time constant affected the battery's voltage reference tracking ability. As the time constant increased, the reference tracking ability became more sensitive to the load conditions.

Appendices

Appendix A

Per-Unit values

The base values for the microgrid AC-side quantities are given in Table A.1. The base power is chosen as 200 kVA, as this is the rating of the power supply interface of the Smart Grid laboratory at NTNU. The base voltage is chosen as the peak value of the line-to-neutral voltage. The base current is chosen as the amplitude of nominal line current. The base values for the microgrid DC-side are determined based on those of the AC side. The base power is the same for both DC and AC sides. However, the DC-side base voltage is defined to be two times the AC-side base voltage. This is to obtain the AC-side voltage of 1.0 pu from the DC-side voltage of 1.0 pu at unity modulation index. The base values are summarized in Table A.2.

Table A.1: *Base values for the microgrid AC-side.*

Quantity	Symbol and Expression	Value
Power	$S_b = \frac{3}{2} V_b I_b$	200 kVA
Voltage	$V_b = \hat{V}_s = \sqrt{\frac{2}{3}} V_n$	326.6 V
Current	$I_b = 2P_b/3V_b$	408.2 A
Frequency	$\omega_b = \omega_0 = 2\pi f_0$	100π rad/s
Impedance	$Z_b = V_b/I_b$	0.8 Ω
Capacitance	$C_b = 1/Z_b\omega_b$	4000 μF
Inductance	$L_b = Z_b/\omega_b$	2500 μH
Modulation	m_b	1 [-]

Table A.2: *Base values for the microgrid DC-side.*

Quantity	Symbol and Expression	Unit
Power	$S_{b,DC} = S_b$	200 kVA
Voltage	$V_{b,DC} = 2V_b$	653.2 V
Current	$I_{b,DC} = (3/4)I_b$	306.2 A
Impedance	$Z_{b,DC} = (8/3)Z_b$	2.13 Ω
Capacitance	$C_{b,DC} = (3/8)C_b$	1500 μF
Inductance	$L_{b,DC} = (8/3)L_b$	6800μH

Appendix B

Equation per-unitizing

The equations presented in Chapter 4 and Chapter 5 are utilized in a per unitized form. They can be found in the reference in a non-per unitized form, and the per unitizing is presented here. Here, underline is used to represent the per unit value of the variable. When the equations are utilized in previous chapters, all equations are in per unit, and the underline is neglected.

The non per-unitized version of Equation 4.1 is is presented in Equation B.1. This is the form that can be found in Reference [23] (pages 219).

$$L\frac{di_d}{dt} = L\omega_0 i_q - (R + r_{on})i_d + \frac{V_{DC}}{2}m_d - V_{sd}, \tag{B.1a}$$

$$L\frac{di_q}{dt} = -L\omega_0 i_d - (R + r_{on})i_q + \frac{V_{DC}}{2}m_q - V_{sq}, \tag{B.1b}$$

As Equation B.1a and B.1b are conceptually the same, only per unitizing of Equation B.1a will be shown.

$$L\frac{di_d}{dt} = \underline{L}\omega_0 i_q - (R + r_{on})i_d + \frac{V_{DC}}{2}\underline{m_d} - V_{sd},$$

$$L_b I_b \underline{L}\frac{d\underline{i_d}}{dt} = L_b\omega_b I_b L\underline{\omega_0 i_q} - Z_b I_b(\underline{R} + \underline{r_{on}})\underline{i_d} + V_{b,DC}\frac{\underline{V_{DC}}}{2}\underline{m_d} - V_b\underline{V_{sd}},$$

$$\frac{Z_b I_b}{\omega_b}\underline{L}\frac{d\underline{i_d}}{dt} = Z_b I_b L\underline{\omega_0 i_q} - Z_b I_b(\underline{R} + \underline{r_{on}})\underline{i_d} + V_b\underline{V_{DC}m_d} - V_b\underline{V_{sd}},$$

$$\frac{1}{\omega_b}\underline{L}\frac{d\underline{i_d}}{dt} = \underline{L\omega_0 i_q} - (\underline{R} + \underline{r_{on}})\underline{i_d} + \underline{V_{DC}m_d} - \underline{V_{sd}}.$$

The modulating signals m_d and m_q are already numbers between zero and unity. Thus, the base value $m_b = 1$, and there is really no difference between the non per-unit value and the per-unit value of this signal. The non per-unitized version of Equation 4.7 is is presented in Equation B.2. This is the form that can be found in Reference [23] (pages 218).

$$P_s(t) = \frac{3}{2}\big[V_{sd}(t)i_d(t) + V_{sq}(t)i_q(t)\big], \tag{B.2a}$$

and

$$Q_s(t) = \frac{3}{2}\big[- V_{sd}(t)i_q(t) + V_{sq}(t)i_d(t)\big]. \tag{B.2b}$$

Per-unitizing Equation B.2a gives

$$P_s = \frac{3}{2}\big[V_{sd}i_d + V_{sq}i_q\big],$$

$$P_b\underline{P_s} = V_bI_b\frac{3}{2}\big[\underline{V_{sd}i_d} + \underline{V_{sq}i_q}\big],$$

$$V_bI_b\frac{3}{2}\underline{P_s} = V_bI_b\frac{3}{2}\big[\underline{V_{sd}i_d} + \underline{V_{sq}i_q}\big],$$

$$\underline{P_s} = \big[\underline{V_{sd}i_d} + \underline{V_{sq}i_q}\big].$$

The non per-unitized version of Equation 4.11 is is presented in Equation B.3. This is the form that can be found in Reference [23] (pages 201).

$$\frac{C}{2}\frac{dV_{DC}^2}{dt} = P_{ext} - P_{loss} - P_t, \tag{B.3}$$

where P_{loss} are losses in the capacitor. Assuming $P_{loss} = 0$ and per-unitizing gives

$$C_{b,DC}V_{b,DC}^2\frac{\underline{C}}{2}\frac{d\underline{V_{DC}^2}}{dt} = P_b\underline{P_{ext}} - P_b\underline{P_t},$$

$$\frac{3}{8}C_b 4V_b^2\frac{\underline{C}}{2}\frac{d\underline{V_{DC}^2}}{dt} = P_b\underline{P_{ext}} - P_b\underline{P_t},$$

$$\frac{3}{2}\frac{1}{Z_b\omega_b}V_b^2\frac{\underline{C}}{2}\frac{d\underline{V_{DC}^2}}{dt} = P_b\underline{P_{ext}} - P_b\underline{P_t},$$

$$\frac{3}{2}\frac{1}{\omega_b}I_bV_b\frac{\underline{C}}{2}\frac{d\underline{V_{DC}^2}}{dt} = P_b\underline{P_{ext}} - P_b\underline{P_t},$$

$$\frac{1}{\omega_b}P_b\frac{\underline{C}}{2}\frac{d\underline{V_{DC}^2}}{dt} = P_b\underline{P_{ext}} - P_b\underline{P_t},$$

$$\frac{\underline{C}}{2\omega_b}\frac{d\underline{V_{DC}^2}}{dt} = \underline{P_{ext}} - \underline{P_t}.$$

The non per-unitized version of Equation 5.3 is is presented in Equation B.4. This is the form that can be found in Reference [23] (page 249).

$$C_f\frac{dV_{sd}}{dt} = C_f(\omega V_{sq}) + i_d - i_{Ld}, \tag{B.4a}$$

$$C_f\frac{dV_{sq}}{dt} = -C_f(\omega V_{sd}) + i_q - i_{Lq}, \tag{B.4b}$$

Per-unitizing Equation B.4a gives

$$C_bV_b\underline{C_f}\frac{d\underline{V_{sd}}}{dt} = C_b\omega_bV_b\underline{C_f}(\underline{\omega}\underline{V_{sq}}) + I_b\underline{i_d} - I_b\underline{i_{Ld}},$$

$$\frac{1}{\omega_bZ_b}V_b\underline{C_f}\frac{d\underline{V_{sd}}}{dt} = \frac{1}{Z_b}V_b\underline{C_f}(\underline{\omega}\underline{V_{sq}}) + I_b\underline{i_d} - I_b\underline{i_{Ld}},$$

$$\frac{1}{\omega_b}\underline{C_f}\frac{d\underline{V_{sd}}}{dt} = \underline{C_f}(\underline{\omega}\underline{V_{sq}}) + \underline{i_d} - \underline{i_{Ld}}.$$

Appendix C

Model specifications

Specifications for the the storage battery lithium-ion model utilized in the simulations are listed in Table C.1. Figure C.1 show the nominal current discharge characteristic of the battery. It can be seen that, if nominal current is drawn from the battery, the terminal voltage is fairly constant throughout a large part of the battery's operating time, considered as the nominal operating range. The voltage drops drastically when the battery is close to depletion, and it increases rapidly when the battery is close to fully charged. As the battery state of charge is initially is set to 60%, it is operated in the nominal range throughout all simulations.

Table C.1: *Specifications for the storage battery lithium-ion model.*

Variable	Value
Nominal voltage	783.8 V
Rated capacity	200 Ah
Initial state of charge	60 %
Response time	0.1 s

Specifications for the the PV-array model utilized in the simulations are listed in Table C.2. Figure C.2 show the PV-array I-V and P-V characteristics at different solar irradiances.

Other specifications are those of the microgrid loads and line impedances, the averaged model of the two-level voltage source converter, and the programmable voltage source. These are listed in Table C.3, Table C.4, and Table C.5, respectively. In the cases where the utility is modelled as a stiff grid, the utility impedance is zero. Otherwise, the impedance has the value specified in the table.

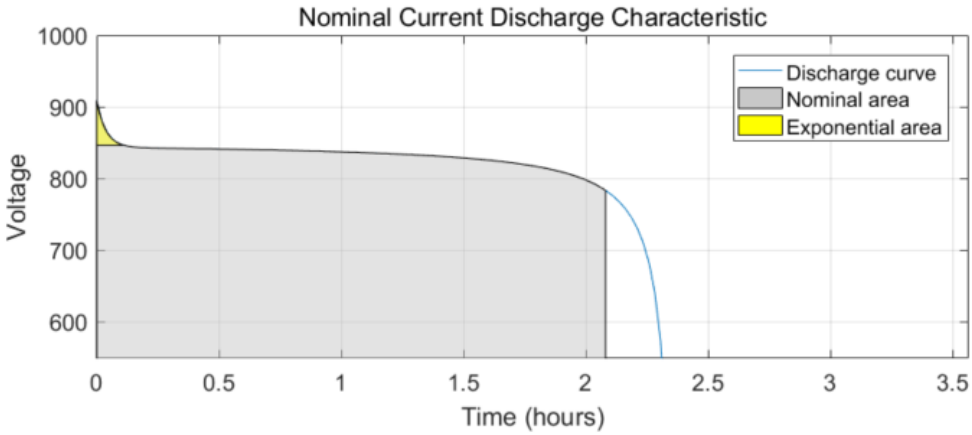

Figure C.1: *Nominal current discharge characteristics of the Lithium-Ion battery utilized in the microgrid Simulink model.*

Table C.2: *Array data for the PV-array model, module SunPower SPR-415E-WHT-D.*

Parameter	Value
Parallel strings	40
Series connected modules per string	12

Table C.3: *Specifications for microgrid loads and line impedances.*

Parameter	Symbol	Value	Value in per unit
Load 1 resistance	R_1	1.60 Ω	2.0
Load 2 resistance	R_2	1.60 Ω	2.0
Load 2 impedance	L_2	5 mH	1.9635
Line impedance	L	50 μH	19.6 e^{-3}
Line resistance	R	0.75 mΩ	0.93 e^{-3}
Capacitance at PCC	C_f	3000 μF	0.754
Utility impedance	L_{th}	50 μH (or zero)	19.6 e^{-3}
Utility resistance	R_{th}	0.75 $m\Omega$ (or zero)	0.93 e^{-3}

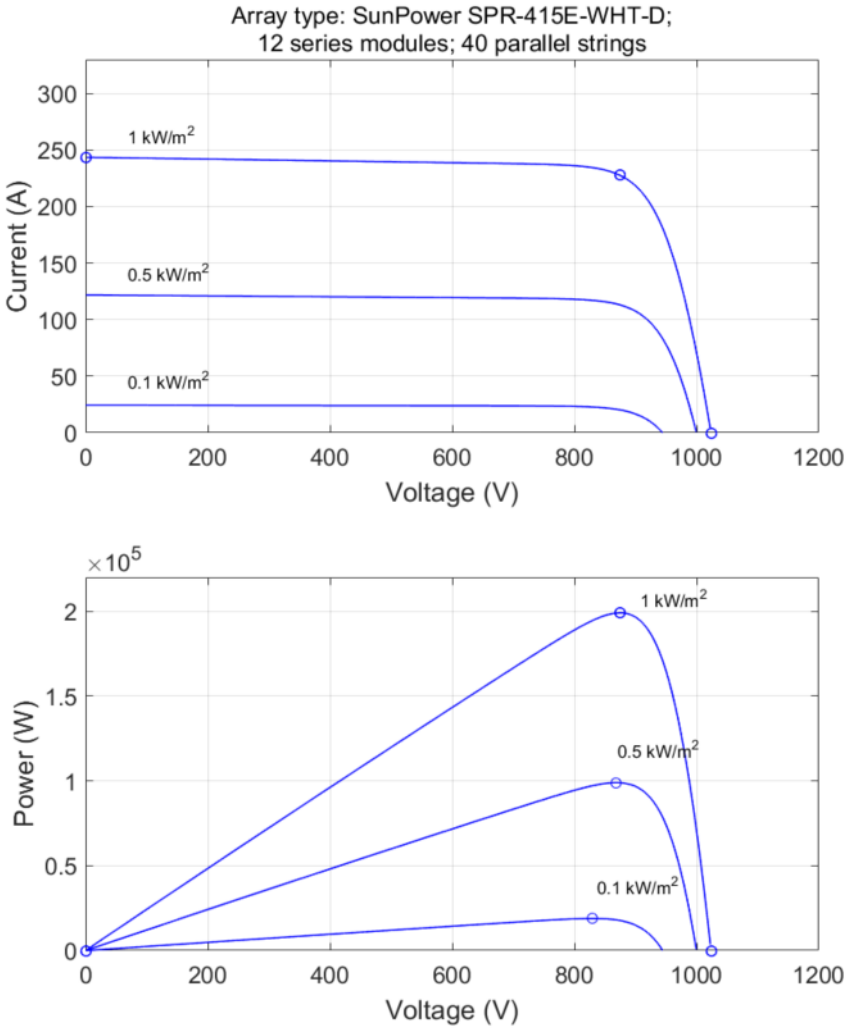

Figure C.2: *PV-array I-V and P-V characteristics at different solar irradiance.*

Table C.4: *Specifications for the averaged model of the two-level voltage source converter from the Simulink Simscape library.*

Parameter	Value	Value in per unit
Diode on-state resistance	88 mΩ	0.11
Diode snubber resistance	1.0 $\mu\Omega$	$1.25e^{-6}$
Diode snubber capacitance	inf	inf
Diode forward voltage	1.0 mV	$3.1e^{-6}$
Current source snubber resistance	inf	inf

Table C.5: *Specifications for the programmable voltage source.*

Parameter	Value	Value in per unit
Voltage amplitude ($V_{rms,ph-ph}$)	400 V	1
Initial phase angle (phase a)	0 deg.	-
Frequency	50 Hz	1

Appendix D

Calculating the angle for the dq-frame

D.1 Grid-connected operation

Transformation to the *dq*-frame can relieve the control system of a significant amount of calculations if the *dq*-frame rotational speed is properly selected. If the rotating frame matches the angular speed of the AC-system, the AC system steady-state signals are DC-signals in the *dq*-frame. Synchronization of the *dq*-frame is achieved by a mechanism called the *phase-locked loop*. Assuming that the voltage at the PCC is balanced, sinusoidal, and of constant frequency, it can be expressed as

$$V_{sa}(t) = \hat{V}_s cos(\omega_0 t + \theta_0), \tag{D.1a}$$

$$V_{sb}(t) = \hat{V}_s cos(\omega_0 t + \theta_0 - \frac{2\pi}{3}), \tag{D.1b}$$

$$V_{sc}(t) = \hat{V}_s cos(\omega_0 t + \theta_0 - \frac{4\pi}{3}), \tag{D.1c}$$

where $\hat{V}_s$ is the peak value of the line-to-neutral voltage, ω_0 is the distribution system (source) frequency, and θ_0 is the source initial phase angle. The space-phasor equivalent of $V_{s,abc}$ is

$$\overrightarrow{V}_s = \hat{V}_s e^{j(\omega_0 t + \theta_0)}. \tag{D.2}$$

Expressed in the *dq*-frame, the space-phasor becomes

$$V_{sd}(t) = \hat{V}_s cos(\omega_0 t + \theta_0 - \rho), \tag{D.3a}$$

$$V_{sq}(t) = \hat{V}_s sin(\omega_0 t + \theta_0 - \rho), \tag{D.3b}$$

where $\rho(t)$ is the rotating angle of the dq-frame. Based on Equation D.3, $\rho(t) = \omega_0 t + \theta_0$ corresponds to $V_{sd} = \hat{V}_s$ and $V_{sq} = 0$. Therefore, synchronization can be achieved by regulating V_{sq} to zero through the PLL. Figure D.1a illustrates a schematic diagram of the PLL. As seen in the figure, feedback from V_{sq} are processed by a compensator, which then adjusts the rotational speed of the dq-frame, ω, such that V_{sq} is forced to zero in the steady state. The end result is that $\rho(t) = \omega_0 t + \theta_0$ and $V_{sd} = \hat{V}_s$. The voltage-controlled oscillator (VCO) in the figure can be regarded as a resettable integrator whose output, ρ, is reset to zero whenever it reaches 2π. Figure D.1b depicts a PLL-block from the Simulink library, where H(p) is a pre-tuned PID-regulator. This PLL block was implemented to our system, and its performance tested. Figure D.2 shows the generated ρ for the dq-transformation, and the resulting PCC voltage in the dq-frame. As seen from the figure, both V_{sd} and V_{sq} are DC-signals, and V_{sq} is equal zero, which is satisfactory behaviour of the PLL.

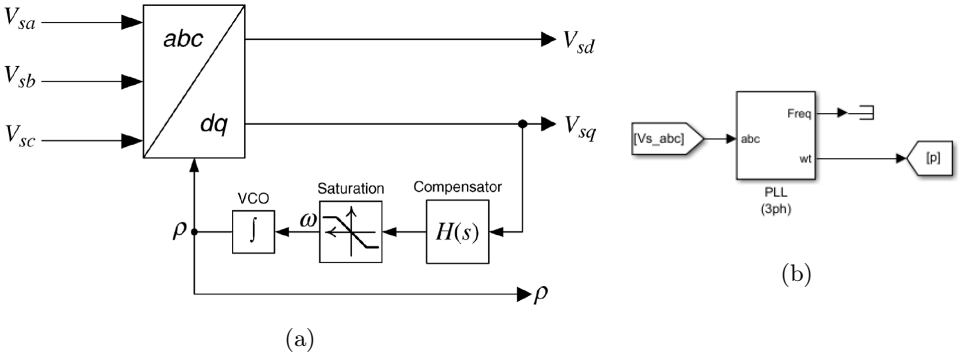

Figure D.1: *The Phase-locked loop adjusts the rotational speed of the dq-frame such that V_{sq} is forced to zero in the steady state. a) Schematic diagram of the phase-locked-loop. b) The pre-tuned phase-locked-loop block from the Simulink library, which takes $V_{s,abc}$ as input, and outputs $\rho(t)$.*

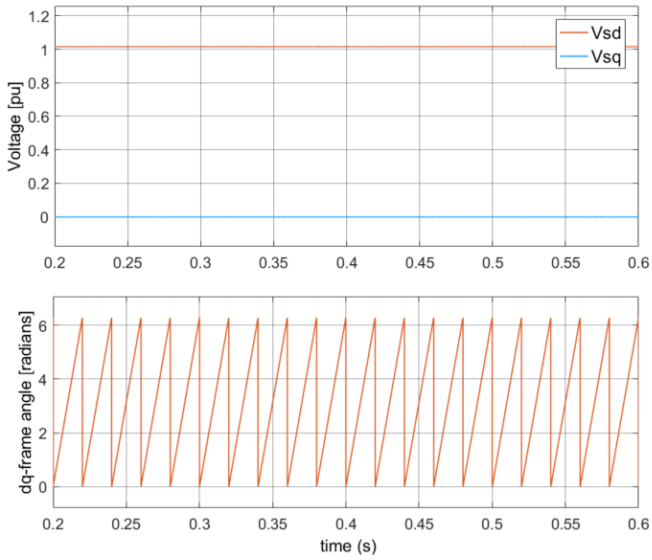

Figure D.2: PLL performance

D.2 Island operation

During grid-connected operation, the microgrid frequency is imposed by the utility. The angle for the *abc*/*dq*-transformation was therefore found by the PLL, who ensured that the rotating frame tracked the frequency of the distribution grid. Further, by utilizing the same angle for the inverse transformation, it assured that the VSC produced AC-voltages of equal frequency as the utility. In isolated operation, the VSC can be set to produce AC-voltages of nominal frequency. Thus, the angle for the *abc*/*dq*-transformation can simply be obtained from a sawtooth generator, as illustrated in Figure D.3. As illustrated in the figure, the sawtooth generator is combined with the PLL from section **??** through a multiplex switch. A mode-signal coming from the sensor at the PCC, detecting whether the microgrid is in grid-connected or island operation, determines whether the angle is created from the PLL or the sawtooth generator.

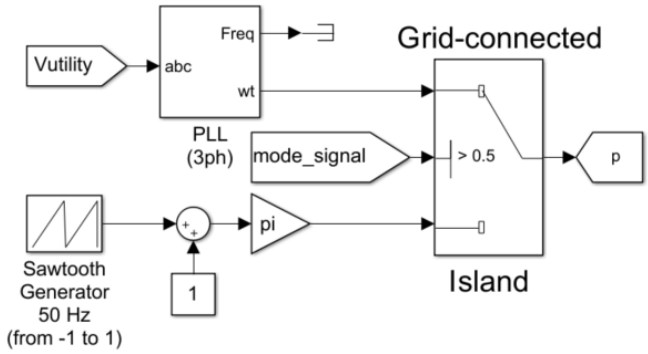

Figure D.3: *Simulink implementation of rotating dq-frame angle creator. The mode-signal distributed from the switch at the PCC determine whether the angle is created from the PLL or the sawtooth generator.*

Appendix E

Simulink implementations

E.1 The complete microgrid

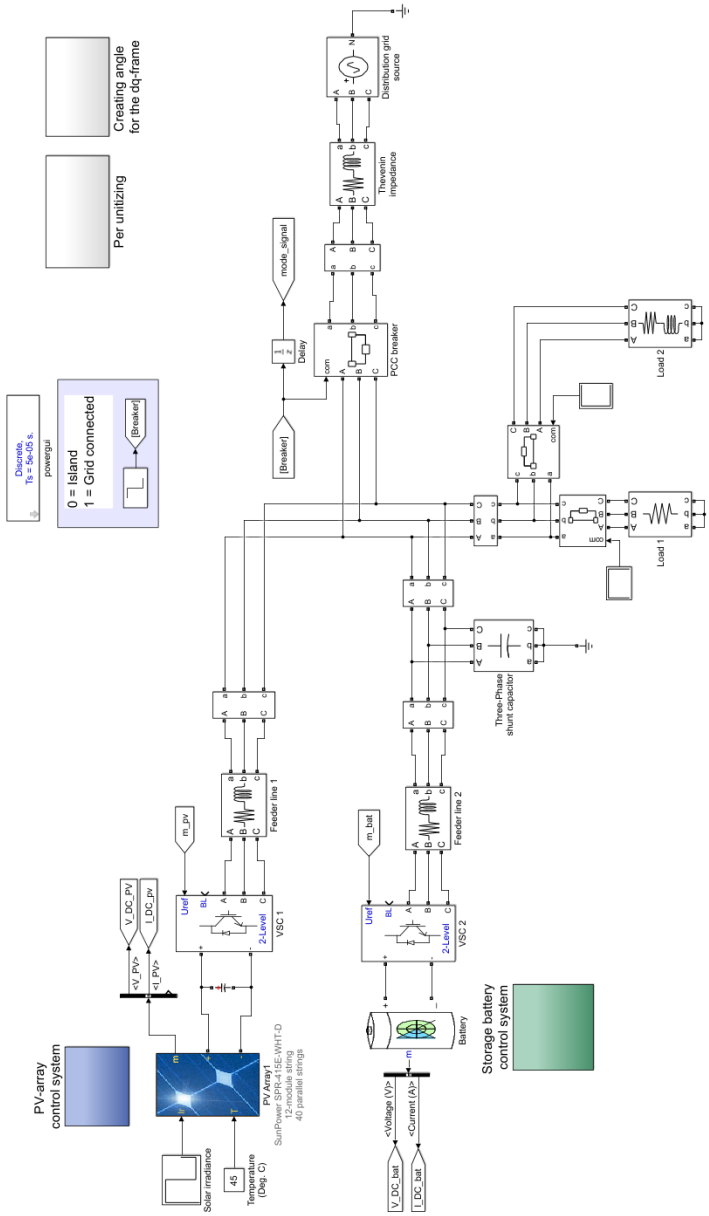

Figure E.1: *The microgrid power system implementation in the Simulink environment.*

E.2 Storage battery control system

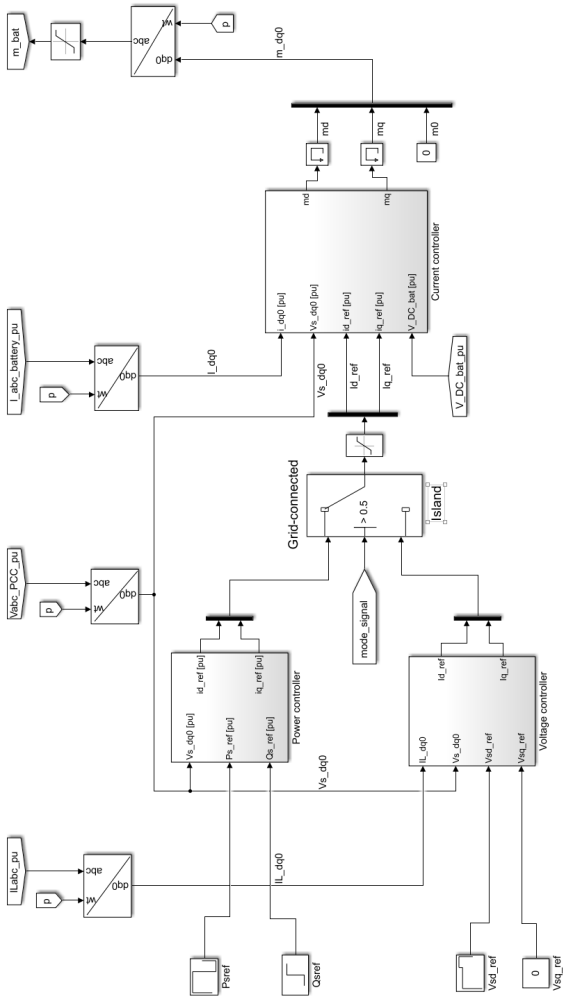

Figure E.2: *The complete storage battery control system implementation in the Simulink environment.*

The current controller

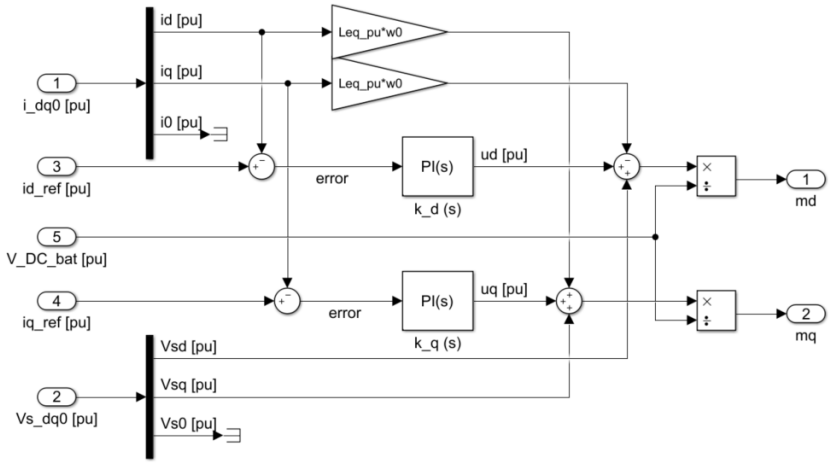

Figure E.3: *The current controller. The inputs are reference currents control signals, and measurements of current, DC-side voltage and PCC voltage. The outputs are m_d and m_q, which are fed to the VSC.*

The power controller

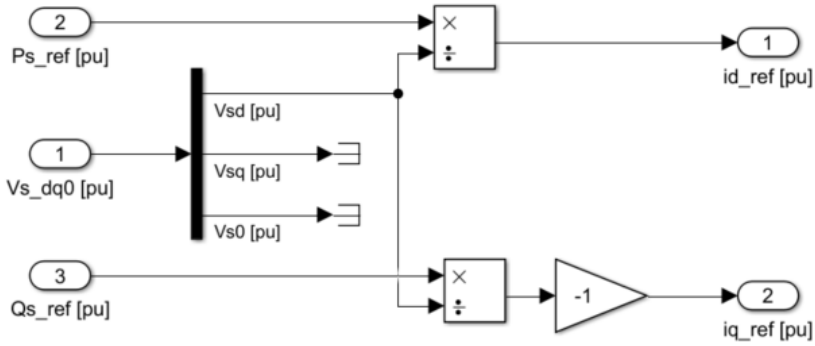

Figure E.4: *Power controller. The inputs are reference powers and measurements of the PCC voltage. The outputs are the reference currents.*

The voltage controller

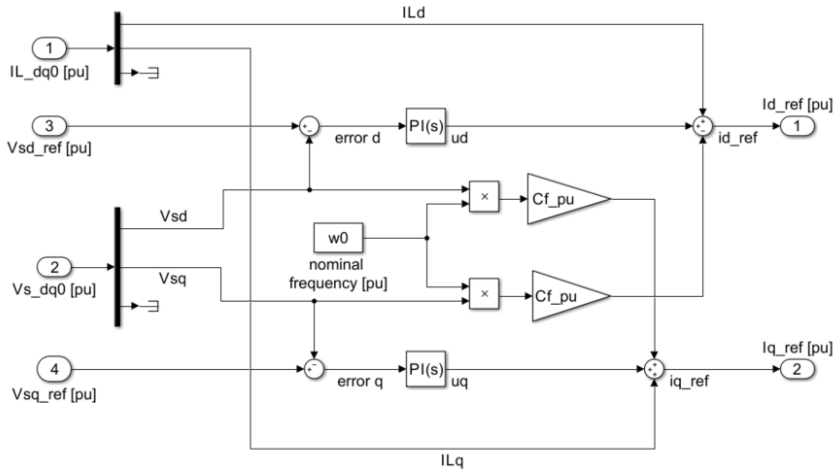

Figure E.5: *The voltage controller. The inputs are reference voltages, and measurements of the PCC voltage and load current. The outputs are the reference currents.*

E.3 PV-array control system

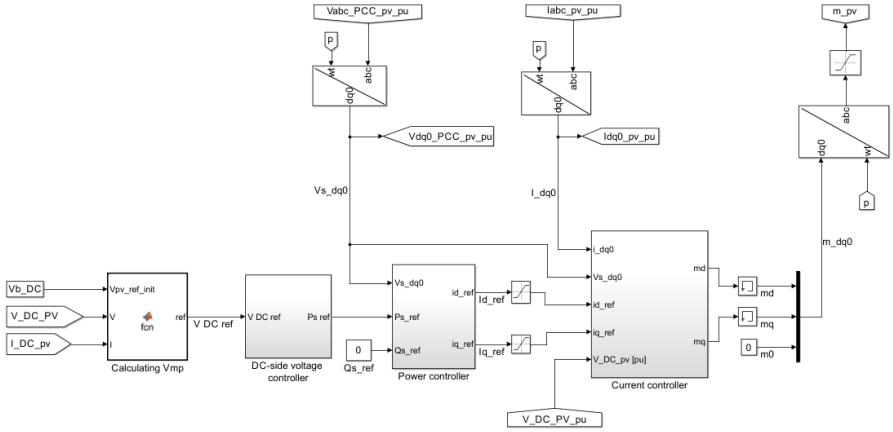

Figure E.6: *The complete PV-array control system implementation in the Simulink environment.*

The DC-side voltage controller

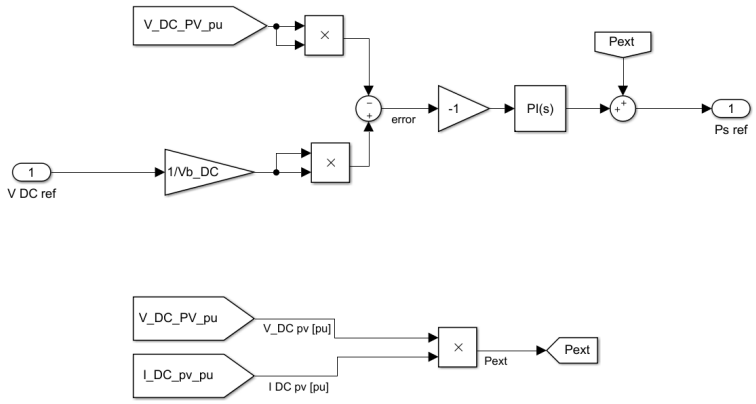

Figure E.7: *The DC-side voltage controller*

MATLAB algorithm for calculating Vmp

```
function ref = fcn(Vpv_ref_init, V, I)

% Perturb & Observe algorithm.
% ref output = Reference for DC link voltage (Vdc_ref)
% V input = PV array terminal voltage (V)
% I input = PV array current (A)

ref_init = Vpv_ref_init;  %Initial reference
delta_ref = 0.015;        %Increment value

persistent Vold Pold ref_old;
dataType = 'double';
if isempty(Vold)
    Vold=0;
    Pold=0;
    ref_old=ref_init;
end
P= V*I;
dV= V - Vold;
dP= P - Pold;

if dP ~= 0
    if dP < 0
        if dV < 0
            ref = ref_old + delta_ref;
        else
            ref = ref_old - delta_ref;
        end
    else
        if dV < 0
            ref = ref_old - delta_ref;
        else
            ref = ref_old + delta_ref;
        end
    end
else
    ref=ref_old;
end
ref_old=ref;
Vold=V;
Pold=P;
```

Appendix F

Regulator tuning methods

F.1 The modulus optimum

The PI-regulators of the current controller are tuned by the method of modulus optimum. The two identical PI-regulators, $k_d(s)$ and $k_q(s)$, are given by

$$k_d(s) = k_q(s) = \frac{k_p s + k_i}{s}, \tag{F.1}$$

where k_p and k_i are the regulator proportional and integral gains. With reference to Figure 4.4, the loop gain, $l(s)$, of the d- and q-axis current control loops become

$$l(s) = (\frac{k_p}{Ls})\frac{s + k_i/k_p}{s + (R + r_{on})/L}. \tag{F.2}$$

The loop gain is seen to include a zero in $s = -k_i/k_p$, and a pole in $s = (R + r_{on})/L$. The goal is to reduce the closed loop transfer function to a first order transfer function. The closed loop transfer function is reduced to a first order transfer function if k_p and k_i are tuned so that the zero cancels the pole. Thus, choosing

$$\begin{aligned} k_p &= L/\tau_i, \\ k_i &= (R + r_{on})/\tau_i, \end{aligned} \tag{F.3}$$

gives a closed loop transfer function, $G_i(s)$, of

$$G_i(s) = \frac{l(s)}{1 + l(s)} = \frac{k_p/(Ls)}{1 + k_p/(Ls)} = \frac{1}{\tau_i s + 1}, \tag{F.4}$$

where τ_i is the time constant of the closed-loop system, and is a design choice.

F.2 The symmetrical optimum

The PI-regulators of the voltage controller and of the the DC-side voltage controller are tuned by this method. The method is suitable for a loop gain that has two poles at s = 0, including the PI-regulator pole and one real pole. To explain the method, the voltage controller will be used as the example. Let the PI-regulators be

$$PI(s) = k\frac{s+z}{s}, \tag{F.5}$$

where k and z are proportional and integral gains, respectively. With reference to Figure 5.4, the loop gain of the d- and q-axis voltage control loops become

$$l(s) = \frac{k\omega_b}{\tau_i C_f}\Big(\frac{s+z}{s+\tau_i^{-1}}\Big)\frac{1}{s^2}. \tag{F.6}$$

Lets analyze the phase response, $\angle l(j\omega)$, of this open loop system. At low frequencies, the phase will approximate $-180°$, due to the double pole at $s = 0$. At higher frequencies, the $s + \tau_i^{-1}$ term contributes to a phase lead, while the $s + z$ term contributes to a phase lag. As the frequency increase, if $z < \tau_i^{-1}$, the phase first increases until it reaches a maximum, δ_m, at a certain frequency, ω_m. Then, for even higher frequencies, the phase angle drops asymptotically until is approaches $-180°$. As stated in Reference [23], δ_m and ω_m are given by

$$\delta_m = sin^{-1}\Big(\frac{1-\tau_i z}{1+\tau_i z}\Big) \tag{F.7}$$

$$\omega_m = \sqrt{z\tau_i^{-1}}. \tag{F.8}$$

If the gain crossover frequency, ω_c, is chosen as ω_w, then δ_m becomes the phase margin. In order for this to hold, the regulator proportional gain, k, must satisfy the condition

$$|l(j\omega_c)| = |l(j\omega_w)| = 1, \tag{F.9}$$

which yields

$$k = \frac{C_f\omega_m}{\omega_b}. \tag{F.10}$$

By selecting a phase margin, δ_m, the integral gain, z, follows from Equation F.7. Then, the proportional gain, k, follows from Equation F.8 and F.10.

Bibliography

[1] International Energy Agency. "Ch. 12: Integration of variable renewables in power systems". In: *World Energy Outlook 2016* (2016), pp. 495–546.

[2] International Energy Agency. "Ch. 10: Renewable energy outlook". In: *World Energy Outlook 2016* (2016), pp. 397–442.

[3] International Energy Agency. "Ch. 3: Energy, emissions and universal access". In: *World Energy Outlook 2017* 1.1 (2017), pp. 107–152.

[4] Mission Innovation Smart Grids. *Smart Grids Innovation Challenge Country Report 2017*. 2017. URL: http://smartgrids.no/mission-innovation-country-report-on-smart-grids/.

[5] E. G. B. Lindeberg. Personal communication. CO_2 Technology, Trondheim Norway. May 2017.

[6] J. Machowski, J. W. Bialek, and J. R. Bumby. *Power System Dynamics: Stability and Control*. 2nd. Chichester, United kingdom: John Wiley & Sons, Ltd., 2012.

[7] S. Souihi et al. "SMILAY: An information flow management framework for microgrid applications". In: *IEEE Communications Magazine* 51.1 (Jan. 2013), pp. 120–126.

[8] H. Bevrani, B. Francois, and T. Ise. *Microgrid dynamics and control*. United States of America: John Wiley & Sons, 2017.

[9] S. Papathanassiou, N. Hatziargyriou, K. Strunz, et al. "A benchmark low voltage microgrid network". In: *CIGRE symposium*. 2005, pp. 1–8.

[10] A. Bernardo et al. "DG behaviour and protection schemes in case of disturbances within the concept of Distribution Grid Area". In: *CIRED 2012 Workshop: Integration of Renewables into the Distribution Grid*. May 2012, pp. 1–4. DOI: 10.1049/cp.2012.0888.

[11] K. A. Potty, P. Keny, and C. Nagarajan. "An intelligent microgrid with distributed generation". In: *IEEE Innovative Smart Grid Technologies-Asia*. Nov. 2013, pp. 1–5.

[12] S. Parhizi et al. "State of the Art in Research on Microgrids: A Review". In: *IEEE Access* 3 (2015), pp. 890–925.

[13] CivicSolar, Inc. *Civicsolar*. 2017. URL: https://www.civicsolar.com/support/installer/articles/microgrid-regulatory-policy-us.

[14] G. Joos et al. "The Need for Standardization: The Benefits to the Core Functions of the Microgrid Control System". In: *IEEE Power and Energy Magazine* 15.4 (July 2017), pp. 32–40. ISSN: 1540-7977. DOI: 10.1109/MPE.2017.2690518.

[15] International Electrotechnical Commission. *IEC/TS 62898-1 Ed.1: Microgrids – Guidelines for microgrid projects planning and specification.* unpublished. 2016.

[16] E. Planas et al. "AC and DC technology in microgrids: A review". In: *Renewable and Sustainable Energy Reviews* 43 (2015), pp. 726–749.

[17] M. P. Thekaekara. "Solar radiation measurement: techniques and instrumentation". In: *Solar Energy* 18.4 (1976), pp. 309–325.

[18] International Energy Agency. *World Energy Outlook 2016.* OECD Publishing.

[19] International Energy Agency. "Ch. 10: The environmental case for natural gas". In: *World Energy Outlook 2017* 1.1 (2017), pp. 107–152.

[20] NVE Plusskunder. Webpage downloaded november 2017. URL: www.nve.no/reguleringsmyndigheten-for-energi-rme-marked-og-monopol/nettjenester/nettleie/tariffer-for-produksjon/plusskunder/.

[21] International Energy Agency. *World Energy Outlook 2017.* OECD Publishing.

[22] D. E. Olivares et al. "Trends in Microgrid Control". In: *IEEE Transactions on Smart Grid* 5.4 (July 2014), pp. 1905–1919.

[23] A. Yazdani and R. Iravani. *Voltage-Sourced Converters in Power Systems : Modeling, Control, and Applications.* Wiley-IEEE Press, 2010.

[24] M. S. Mahmoud. *Microgrid: Advanced Control Methods and Renewable Energy System Integration.* 1st ed. Amsterdam, Netherlands: Elsevier Ltd, 2017.

[25] NVE. *Smart metering (AMS).* Webpage downloaded october 2017. URL: https://www.nve.no/energy-market-and-regulation/retail-market/smart-metering-ams/.

[26] M.A. Abido M.S. Mahmoud S. A. Hussain. "Modeling and control of microgrid: An overview". In: *Journal of the Franklin Institute* 351.5 (2014), pp. 2822–2859.

[27] I. Mitra, T. Degner, and M. Braun. "Distributed generation and microgrids for small island electrification in developing countries: a review". In: *Solar Energy Society of India* 18.1 (2008), pp. 6–20.

[28] R. Bayindir et al. "A comprehensive study on microgrid technology". In: *International Journal of Renewable Energy Research* 4.4 (2014), pp. 1094–1107.

[29] O. Dag and B. Mirafzal. "On stability of islanded low-inertia microgrids". In: *2016 Clemson University Power Systems Conference (PSC).* Mar. 2016, pp. 1–7.

[30] T. E. Huayllas, D. S. Ramos, and R. L. Vasquez-Arnez. "Microgrid systems: Current status and challenges". In: *2010 IEEE/PES Transmission and Distribution Conference and Exposition: Latin America (T D-LA).* Nov. 2010, pp. 7–12.

[31] F. Li, R. Li, and F. Zhou. *Microgrid technology and engineering application.* Elsevier Ltd, 2016. ISBN: 0-12-803598-6.

[32] C. Li et al. “A review of islanding detection methods for microgrid”. In: *Renewable and Sustainable Energy Reviews* 35 (2014), pp. 211–220.

[33] A. Luque and S. Hegedus. *Handbook of Photovoltaic Science and Engineering*. Chichester, UK: John Wiley & Sons, 2011. Chap. The Physics of the Solar Cell.

[34] D. P. Hohm and M. E. Ropp. “Comparative study of maximum power point tracking algorithms using an experimental, programmable, maximum power point tracking test bed”. In: *Conference Record of the Twenty-Eighth IEEE Photovoltaic Specialists Conference - 2000*. 2000, pp. 1699–1702.

[35] Kjell Sand. “Leveringskvalitet - en oversikt”. In: *SINTEF* (2008).

[36] J. G. Balchen, T. Andresen, and B. A Foss. *Reguleringsteknikk*. 5th ed. Institutt for teknisk kybernetikk, Norges teknisk-naturvitenskapelige universitet, 2004.

[37] M. Holt. “Feasibility Studies on a Stand-Alone Hybrid Wind-Diesel System for Fish Farming Applications”. MA thesis. Norwegian University of Science and Technology, 2017.